Laser Photonics Rev. **5**, No. 4, 571–606 (2011) / **DOI** 10.1002/lpor.201000009

LASER & PHOTONICS REVIEWS

Abstract Surface plasmon resonance (SPR) sensors have been a mature technology for more than two decades now, however, recent investigations show continuous enhancement of their sensitivity and their lower detection limit. Together with the recent investigations in localized SPR phenomena, extraordinary optical transmission through nanoapertures in metals, and surface-enhanced spectroscopies, drastic developments are expected to revolutionize the field of optical biosensing. Sensitivity-enhancement (SE) techniques are reviewed focusing both on the physical transduction mechanisms and the system performance. In the majority of cases the SE is associated with the enhancement of the electromagnetic field overlap integral describing the interaction energy within the analyte. Other important mechanisms are the interaction between plasmons and excitons and between the analyte molecules and the metal surface. The lower detection limit can be reduced significantly if systems with high signal-to-noise ratio are used such as common-path interferometry, ellipsometry or polarimetry systems.

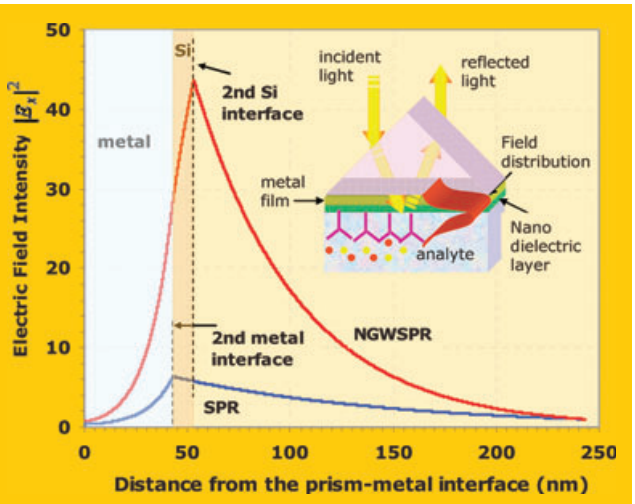

Sensitivity-enhancement methods for surface plasmon sensors

Atef Shalabney and Ibrahim Abdulhalim*

1. Introduction

Surface plasmon resonance (SPR) sensing devices have seen a tremendous growth during the last decade [1, 2] both from a fundamental point of view and as highly sensitive devices for optical sensing of small biological or chemical entities in gases and liquids [3]. There are two main types of surface plasmons (SPs): extended and localized. The extended SP is considered as more classical [4] since it has been known for a longer time. It can be described as a longitudinal electromagnetic wave (EM) in a two-dimensional electron gas that exists on the interface between metals and dielectrics. Localized SPs on the other hand became more familiar only during the last two decades and they are excited in metallic structures with dimensions less than half the wavelength of the exciting electromagnetic (EM) wave. In both cases the incident EM field has to be polarized in the plane of incidence (transverse magnetic (TM) polarization). In the case of extended or propagating surface plasmon resonance (PSPR), the plasmon propagates along the interface between metal and dielectric, for distances on the order of tens to hundreds of micrometers and decay evanescently in the z direction with a 1/e decay length on the order of 200 nm. The interaction between the metal surface-confined EM waves and the molecular layer of interest leads to shifts in the plasmon resonance, which can be observed in three modes: (a) angle resolved (b) wavelength shift, and (c) imaging. In the first two modes, one measures the reflectivity of light from the metal surface as a function of either wavelength (at constant incidence angle) or as a function of incidence angle (at constant wavelength). The third mode uses light of both constant wavelength and incidence angle to interrogate a two-dimensional region of the sample, mapping the reflectivity of the sample as a function of position.

For the case of localized surface plasmon resonance LSPR, light interacts with particles much smaller than the incident wavelength [1]. This leads to a plasmon that oscillates locally around the nanoparticle with a frequency known as the LSPR frequency. Similar to PSPR, the LSPR is sensitive to changes in the local dielectric environment. Typically, researchers measured changes in the local dielectric environment through LSPR wavelength-shift measurements, although a variant of angle-resolved sensing for the LSPR is also possible. Both PSPR and LSPR can provide thermodynamic and real-time kinetic data for binding processes. Moreover, although PSPR spectroscopy provides much higher sensitivity to changes in the bulk refractive index than LSPR spectroscopy, the response of the two techniques becomes comparable when measuring short-range (in the nm vicinity of the metal surface) changes in the refractive index owing to a molecular adsorption layer. This is a result of the much smaller sensing volume offered by the LSPR sensors, as the EM-decay length is 40–50 times shorter than that of the PSPR sensors. Moreover, advances

Department of Electro Optic Engineering and The Ilse Katz Institute for Nanoscale Science and Technology, Ben Gurion University of the Negev, Beer Sheva 84105, Israel
* Corresponding author: e-mail: abdulhlm@bgu.ac.il

in synthetic and lithographic fabrication techniques allow tuning of the localized resonance wavelength through the visible, near-infrared, and into the infrared regions of the EM spectrum, by varying shape, size, and material of the nanoparticles that support the LSPR. This offers additional flexibility when designing LSPR sensing experiments.

The PSPR biosensors have been widely applied in a diverse range of fields, including molecular recognition, and disease immunoassays [5–10] etc. Even though conventional SPR biosensors are more sensitive than other label-free devices, they are still unable to achieve the direct detection of small molecular (a few hundred of Daltons) interactions or low molecular concentrations (physiological concentration) on the surface of the biosensor. Consequently, various proposals have been developed to enhance the sensitivity or resolution of biosensors by using different SPR modes or detection methods [11–16]. It is the purpose of this article to provide a review of the sensitivity-enhancement techniques of SPR sensors. Also, various LSPR biosensors have been proposed that employ the strong UV-Vis absorption band of the metal nanoparticles to yield an area mass detection limit of 100–1000 pg/mm^2. However, this detection capability is poorer than that of conventional PSPR biosensors by at least 100 times [17–19]. On the other hand, the local EM field enhancement near nanostructures causes huge enhancement of other spectroscopic signals such as surface-enhanced Raman scattering (SERS) and surface-enhanced fluorescence (SEF). These spectroscopic techniques provide another important sensing parameter, which is specificity. The enhancement factor depends strongly on the shape of the nanostructure and the type of the metal. In this review article our purpose is to present the sensitivity-enhancing mechanisms and some of the concepts being pursued to achieve enhanced sensitivity.

2. SPR phenomena

2.1. Extended or propagating SPR – theory and sensing mechanism

Although the basics of SPR theory are well known from several books and book chapters [20], for completeness there is a need for a short description and in particular to address certain points that are not well addressed in the existing literature with high relevance to this article such as: sensitivity definitions, mathematical expressions for sensitivity and expanding the discussion on LSPR sensing mechanism.

SP waves are a longitudinal charge-density distribution generated on the metal side interface when light propagates through the metal. Both the metal and the dielectric sample can be with complex refractive indices $n_{\mathrm{m}} = \sqrt{\varepsilon_{\mathrm{m}}}$ and $n_{\mathrm{a}} = \sqrt{\varepsilon_{\mathrm{a}}}$, respectively as shown in Fig. 1. The surface plasmon propagates as an electromagnetic wave parallel to the x direction with magnetic field oriented parallel to the y direction that is, transverse magnetic polarization (TM) state. The condition of (TM) polarization state is needed to generate the charge distribution on the metal interface, which is considered as the first condition for SP excitation. The SP

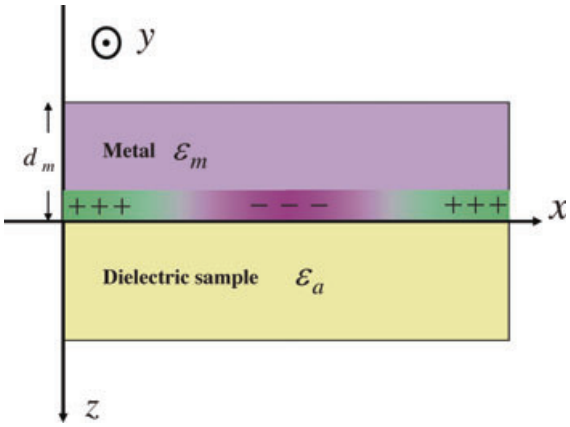

Figure 1 (online color at: www.lpr-journal.org) Metallic and dielectric layers with $n_{\mathrm{m}} = \sqrt{\varepsilon_{\mathrm{m}}}$ and $n_{\mathrm{a}} = \sqrt{\varepsilon_{\mathrm{a}}}$ complex refractive indices respectively, and separated by the *xy*-plane, supporting SPW at the interface in the metal side.

phenomenon can be easily understood, and its main characteristics can be determined by solving Maxwell's equation to the boundary-value problem. By assuming TM plane and harmonic electromagnetic fields in the metal and the sample with the appropriate waves:

$$\begin{aligned} E_i(r,t) &= (E_{ix}, 0, E_{iz}) e^{-k_{zi}|z|} e^{i(k_{xi}x - \omega t)}, \\ H_i(r,t) &= (0, H_{iy}, 0) e^{-k_{zi}|z|} e^{i(k_{xi}x - \omega t)}, \end{aligned} \tag{1}$$

where, $(i = \text{metal, sample})$, k_{zi} is the z component of the wavevector in the layer i, and k_{xi} is the X component of the wavevector. Substituting the fields from Eq. (1) into Maxwell's equations and applying the continuity conditions and the relation

$$k_{zi} = \sqrt{\varepsilon_i \frac{\omega^2}{c^2} - k_{xi}^2}$$

leads to:

$$\begin{aligned} \frac{k_{z1}}{\varepsilon_1} H_{1y} + \frac{k_{z2}}{\varepsilon_2} H_{2y} &= 0, \\ H_{1y} - H_{2y} &= 0. \end{aligned} \tag{2}$$

A solution could be obtained for the last equations set by equating the determinant to zero leading to: $k_{z1}\varepsilon_2 + k_{z2}\varepsilon_1 = 0$, which together with the phase-matching condition $k_{x1} = k_{x2} = k_x$ the following expression is found:

$$k_x = \frac{\omega}{c} \sqrt{\frac{\varepsilon_1 \varepsilon_2}{\varepsilon_1 + \varepsilon_2}}. \tag{3}$$

The value in the left-hand side of Eq. (3) represents the surface plasmon wavevector $k_x = k_{\mathrm{SP}}$, hence Eq. (3) defines the dispersion relation for the propagating SP. Since in the range of optical frequencies, the real part of the metal dielectric constant $\varepsilon_{\mathrm{mr}} < 0$ and assuming that the imaginary parts of both $\varepsilon_1 = \varepsilon_{\mathrm{m}} = \varepsilon_{\mathrm{mr}} + i\varepsilon_{\mathrm{mi}}$ and $\varepsilon_2 = \varepsilon_{\mathrm{a}} = \varepsilon_{\mathrm{ar}} + i\varepsilon_{\mathrm{ai}}$ are small, a purely real SP wavevector can be obtained when $\varepsilon_{\mathrm{mr}} < -\varepsilon_{\mathrm{a}}$

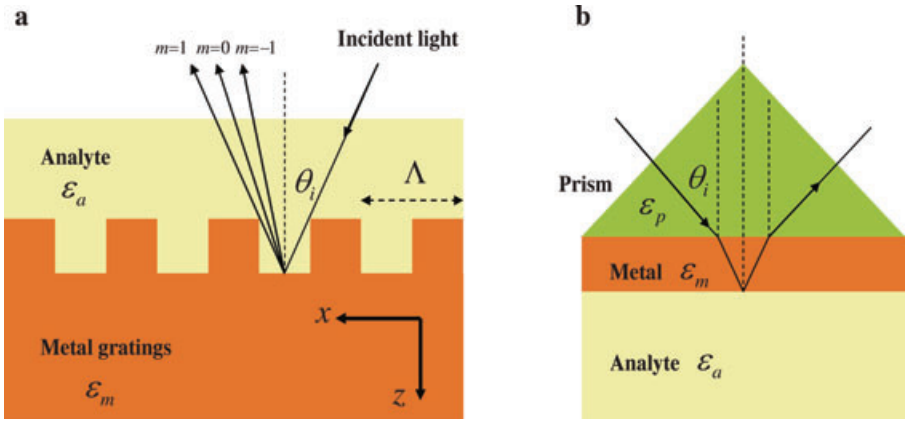

Figure 2 (online color at: www.lpr-journal.org) (a) Enhancing the wavevector of the incident light by the diffraction angle modification. (b) Enhancing the wavevector by prism coupling, the resonance obtained by increasing the momentum of the incident light by the prism high refractive index (Kretschmann configuration)

allowing long-range propagation. This is the second condition for SP existence at the metal/dielectric interface.

Substituting the simplified Drude model for the metal dispersion $\varepsilon_m = 1 - \frac{\omega_p^2}{\omega^2}$ when ω_p is the plasma frequency, in Eq. (3) gives an explicit expression for the dispersion relation of the SP:

$$\omega^2 = \frac{1}{2}\omega_p^2 + \frac{1}{2}k_x^2c^2\left(1+\frac{1}{\varepsilon_a}\right) - \frac{1}{2}\sqrt{\omega_p^4 + 2\omega_p^2k_x^2c^2\left(1-\frac{1}{\varepsilon_a}\right) + k_x^4c^4\left(1+\frac{1}{\varepsilon_a}\right)^2}. \quad (4)$$

On the other hand, the wavevector of light falling on the metallic film satisfies the dispersion line of a photon in free space $(\omega = ck_0)$, which lies on the left of the dispersion line of the plasmon for any frequency, see Fig. 3. Hence, a light beam that hits the metal surface from air will never excite the plasmon at the metal interface unless the photon momentum is enhanced in order to fulfill the matching with the SP momentum, and an intersection between the two lines is obtained. The intersection represents the resonance phenomenon and defines an operating point in which the frequency and the wavevector of both the exciting light and the plasmon are determined. In the case of PSPR, two main techniques are used to enhance the wavevector, (1) prism coupling, in which the wavevector is enhanced by the prism refractive index, (2) diffraction gratings, in which the wavevector is enhanced by the diffraction angle modification as shown in Fig. 2.

Perturbation in the analyte refractive index causes a change in the intersection point and consequently a shift in the resonance wavelength for a fixed incidence angle or a shift in the incidence angle for a fixed wavelength, see Fig. 3. The frequency axis in Fig. 3 is normalized to the plasma frequency, and simultaneously the plasmon wavevector is normalized to the volume plasmon wavevector that is defined as $k_p \equiv \frac{\omega_p}{c}$. Fig. 3 demonstrates clearly the sensing mechanism of the Kretschmann configuration. An increase in the analyte refractive index modifies the plasmon's dispersion curve, and the resonance is obtained at a larger wavelength when the incidence angle is fixed. On the other hand, if one wants to keep the wavelength fixed, the slope of the incident light should be changed by increasing the incidence angle.

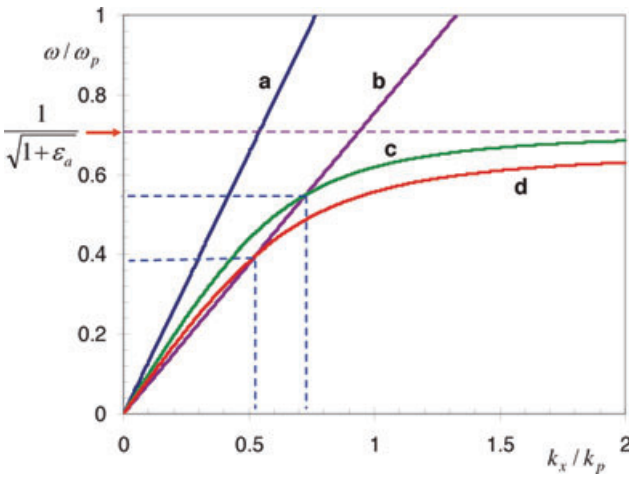

Figure 3 (online color at: www.lpr-journal.org) (a) Dispersion line for free photon incident onto the metal from vacuum. (b) Dispersion line for photon emerging from prism with refractive index 1.732, and with incidence angle equals 50 degrees. (c) Dispersion relation of surface plasmon at the interface between metal and air (as a sample). (d) Dispersion relation of surface plasmon generated at the interface between metal and an analyte with 1.15 refractive index. For a fixed incidence angle, changes in the analyte refractive index demand a corresponding change in the incident light wavelength to maintain resonance, or alternatively a modification in the incidence angle for fixed wavelength. The frequency is normalized to the plasma frequency ω_p, and the x component of the light wavevector is normalized to the plasma wave number, which is defined in the text.

As the plasmon is excited, the wave propagates along the surface in the x direction, which gets absorbed after a certain propagation length. Resonance is then realized as a dip in the reflectivity spectrum (Fig. 4).

Different definitions of the sensitivity were considered in the literature; here we introduce four of them out of the most prominent and widespread. First, when the wavelength is fixed, *angular sensitivity* is defined as the ratio between the resonance angle shift and the analyte refractive-index change (Fig. 4a). Secondly, if the incidence angle is kept fixed, *spectral sensitivity* is the ratio between the resonance wavelength shift and the analyte refractive-index change as illustrated in Fig. 4b. The first two definitions [21] are

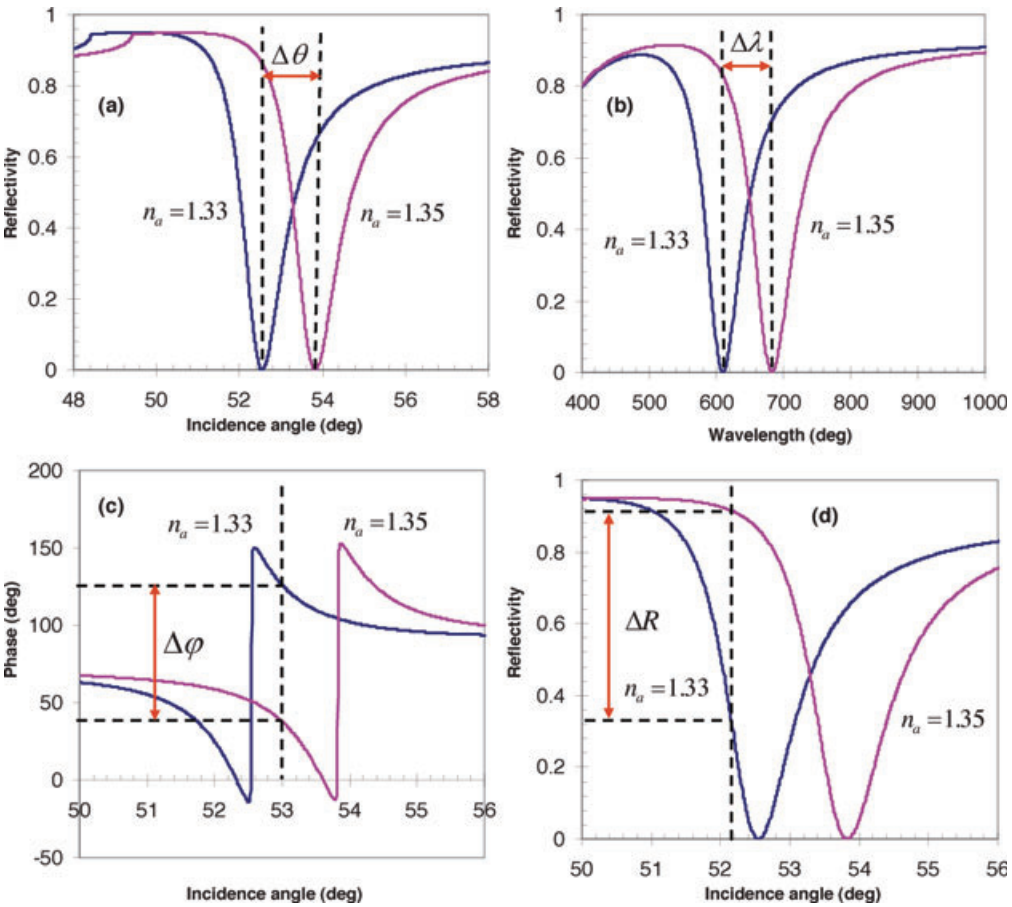

Figure 4 (online color at: www.lpr-journal.org) Illustration of the shift in the resonance due to a change in the analyte refractive index, the blue and the red curves correspond to $n_a = 1.33$ and $n_a = 1.35$, respectively, to clarify the four sensitivity definitions: (a) SPR angle shift (b) SPR wavelength shift (c) SPR phase change and (d) SPR reflectivity change at the steepest slope.

summarized as follows:

$$S_\theta \equiv \frac{d\theta}{dn_a} \quad \text{(for fixed wavelength)};$$
$$S_\lambda \equiv \frac{d\lambda}{dn_a} \quad \text{(for fixed angle)}. \tag{5}$$

Expressions for the angular and spectral sensitivities for both the Kretschmann configuration and the gratings configuration, and are given by:

1. For the Kretschmann configuration:

$$S_\theta \equiv \frac{d\theta}{dn_a} = \frac{\varepsilon_{mr}\cdot\sqrt{-\varepsilon_{mr}}}{(\varepsilon_{mr}+n_a^2)\cdot\sqrt{\varepsilon_{mr}(n_a^2-n_p^2)-n_a^2\cdot n_p^2}},$$
$$S_\lambda \equiv \frac{d\lambda}{dn_a} = \frac{\varepsilon_{mr}^2}{\frac{1}{2}\cdot\left|\frac{d\varepsilon_{mr}}{d\lambda}\right|\cdot n_a^3+\frac{\varepsilon_{mr}\cdot n_a}{n_p}\cdot\frac{dn_p}{d\lambda}\cdot(\varepsilon_{mr}^2+n_a^2)}, \tag{6}$$

n_p is the prism refractive index, $\left|\frac{d\varepsilon_{mr}}{d\lambda}\right|$, $\frac{dn_p}{d\lambda}$ are the metal and the prism dispersions, respectively.

2. For the gratings configuration:

$$S_{G\theta} \equiv \frac{d\theta}{dn_a} = \frac{1}{n_a\cos\theta}\left[\frac{\varepsilon_{mr}^{3/2}}{(\varepsilon_{mr}+n_a^2)^{3/2}}-\sin\theta\right],$$
$$S_{G\lambda} \equiv \frac{d\lambda}{dn_a} = \frac{\left[\frac{m\lambda}{n_a\Lambda}+\sqrt{\frac{\varepsilon_{mr}}{\varepsilon_{mr}+n_a^2}}\cdot\frac{n_a^2}{|\varepsilon_{mr}+n_a^2|}\right]}{\left[\frac{m}{\Lambda}+\frac{n_a^3}{2\sqrt{\varepsilon_{mr}}\cdot|\varepsilon_{mr}+n_a^2|^{3/2}}\cdot\frac{d\varepsilon_{mr}}{d\lambda}\right]}. \tag{7}$$

The third definition corresponds to the change in the reflected intensity (at the steepest slope point) versus the analyte refractive-index change namely *intensity sensitivity* (Fig. 4d). The fourth definition is the *phase sensitivity*, which is defined as the change in the phase of the p-polarized component with the change in the analyte refractive index (Fig. 4c). Intensity and phase shifts are measured when the incidence angle and wavelength are kept fixed.

The sensitivity, as defined above, expresses the rate of change of the information parameter magnitude (measurand) with the analyte refractive index and it should be accurately distinguished from the limit of detection (LOD). The LOD is the smallest quantity of change in the analyte RI (or translated into concentration) that can be detected by the system. Surprisingly the LOD is often mistakenly called sensitivity, which is inadequate and misleading. While the sensitivity is determined solely by the transduction mechanism, the LOD

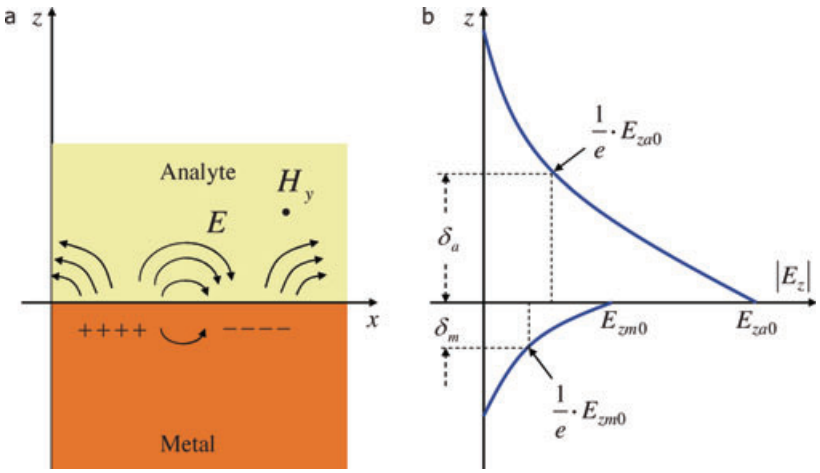

Figure 5 (online color at: www.lpr-journal.org) (a) SP wave at the interface between the metal and dielectric have a combined electromagnetic wave and surface charge. They are transverse magnetic (magnetic field in the y direction), because the generation of surface charge needs an electric-field component perpendicular to the surface. (b) Enhancing the field component perpendicular to the interface due to the surface charge. δ_m, δ_d, are the decay lengths of the field perpendicular to the surface in the metal and the dielectric regions, respectively.

is determined both by the sensitivity and the noise level of the sensor as a system. Indicating $\Delta\chi$ the change in the information parameter related to the SPR signal (χ could be angle, wavelength, intensity, or phase), S_χ is the sensitivity corresponding to the parameter χ, while the LOD in this case will be: $LOD = \Delta\chi_{min}/S_\chi$. The parameter $\Delta\chi_{min}$ is the minimum detectable change in the measurand, which is usually taken as the value of the noise level (signal-to-noise ratio SNR = 1). Hence, by improving the system precision the LOD can be improved. This of course can be achieved by several means such as using less-noisy detectors and sources or using averaging and other signal-processing techniques. Subpixelling resolution can be achieved by using inverse scattering approaches usually used in ellipsometry, for example, by which the optical response curve is fitted to a theoretical model. Lahav et al. [57] used a parabolic fit of the neighborhood of the SPR minimum to achieve subpixelling and improve the LOD.

The SPR phenomenon is accompanied by an evanescent field that decays exponentially into both the metal and the analyte regions. The field enhancement adjacent to the interface explains physically the sensitivity of the device to perturbations in the sample refractive index, as shown in Fig. 5. The evanescent field generated at the interface prevents EM power from propagating away from the surface. The penetration depth δ_d in the dielectric is of the order of half the wavelength of the light involved. Whereas the decay length inside the metal, δ_m, is determined by the skin depth. The confinement dimensions are given by:

$$\delta_m = \frac{\lambda}{2\pi}\cdot\sqrt{\frac{\varepsilon_a+\varepsilon_{mr}}{-\varepsilon_{mr}^2}}; \qquad \delta_d = \frac{\lambda}{2\pi}\cdot\sqrt{\frac{\varepsilon_a+\varepsilon_{mr}}{-\varepsilon_a^2}}. \quad (8)$$

Since the wavevector of the plasmon is not purely real as we assumed before, the plasmon wave also decays in the x direction upon propagation along the interface.

$$k_x' + ik_x'' = \frac{\omega}{c}\sqrt{\frac{(\varepsilon_{mr}+i\varepsilon_{mi})\varepsilon_a}{(\varepsilon_{mr}+\varepsilon_a)+i\varepsilon_{mi}}};$$
$$L_x = \frac{1}{2\left|k_x''\right|} = \frac{\lambda}{2\pi}\cdot\frac{\varepsilon_{mr}^2}{\varepsilon_{mi}}\cdot\left[\frac{\varepsilon_a+\varepsilon_{mr}}{\varepsilon_a\cdot\varepsilon_{mr}}\right]^{3/2}, \quad (9)$$

where k_x', k_x'' are the real and the imaginary parts of the plasmon wavevector, respectively, and L_x is the longitudinal propagation length at the interface, which is of the order of tens micrometers. Note that L_x is defined as the decay length of the energy $|E_x|^2$, while δ_m, δ_d correspond to the decay lengths of the field $|E_z|$.

2.2. Localized SPR – theory and sensing mechanism

LSPR is generated when light interacts with small metal nanofeatures such as nanoparticles, nanoholes or nanoshells. A full theoretical description of localized surface plasmons is quite lengthy and beyond the scope of this review. For our purpose, we first consider a small metallic sphere with radius a and volume V irradiated with light of angular frequency ω and wavelength λ (the radius a is very small relative to the wavelength λ). Since the magnitude of the electric field seems static around the nanoparticle in this limit, we can solve Maxwell's equations in the quasistatic approximation. Under this assumption, the solution of the EM fields outside the sphere will be [22]:

$$E_{out}(x,y,z) = E_0\hat{z} - \left[\frac{\varepsilon_m-\varepsilon_d}{\varepsilon_m+2\varepsilon_d}\right]\cdot a^3E_0 \cdot\left[\frac{\hat{z}}{r^3}-\frac{3z}{r^5}(x\cdot\hat{x}+y\cdot\hat{y}+z\cdot\hat{z})\right], \quad (10)$$

where E_0 is the applied field magnitude that is polarized in the z direction in this case, ε_m is the metallic sphere dielectric constant, and ε_d the dielectric medium refractive index in which the sphere is embedded. The electric field of an electromagnetic radiation displaces the free-electron cloud and produces uncompensated charges near a particle surface and corresponding opposing forces (as in Fig. 6). The optical resonance related to these oscillations called the LSPR. In the general case, the frequency of the collective oscillations does not coincide with the applied wave frequency and is determined by many factors, the electron concentration, electron effective mass, the particle shape

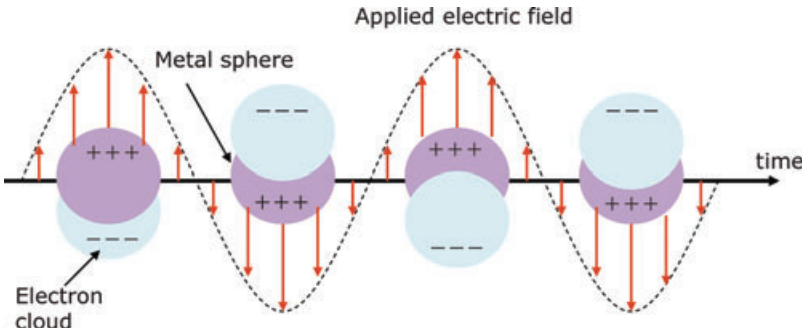

Figure 6 (online color at: www.lpr-journal.org) Oscillations of free electrons at the surface of a nanosphere due to applied electric field with arbitrary polarizations.

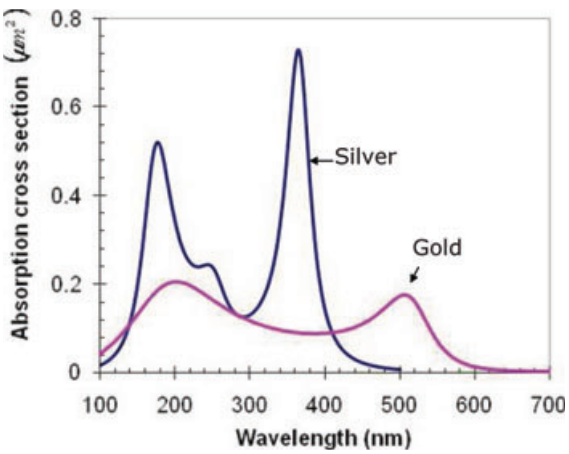

Figure 7 (online color at: www.lpr-journal.org) Absorption cross section for silver and gold spheres. Both silver and gold spheres are with 100 nm diameter and embedded in air, the y-axis is normalized to $10^{-12}\,\mathrm{m}^2$.

and size, interaction between particles, and the influence of the environment. However, for the elementary description of the nanoparticles plasmon resonance it is sufficient to use the usual dipole approximation, and the Drude model.

In this case, the absorption and scattering of light by a small particle are determined by the electrostatic polarizability of the particle α_0, which can be calculated using the optical permittivity $\varepsilon_\mathrm{m}(\omega)$ of the metal (ω is the angular frequency, and λ the wavelength in vacuum), the medium dielectric constant, and the particle geometrical dimensions (see Fig. 7) [23].

$$\alpha_0 = \frac{3}{4}\frac{V}{\pi}\left(\frac{\varepsilon_\mathrm{m}-\varepsilon_\mathrm{d}}{\varepsilon_\mathrm{m}+2\varepsilon_\mathrm{d}}\right) = a^3\left(\frac{\varepsilon_\mathrm{m}-\varepsilon_\mathrm{d}}{\varepsilon_\mathrm{m}+2\varepsilon_\mathrm{d}}\right). \tag{11}$$

Using the renormalized polarizability to be consistent with the energy-conservation law, the integrated absorption and scattering are calculated by:

$$\begin{aligned} C_\mathrm{ext} &= C_\mathrm{abs} + C_\mathrm{sca} \\ &= \frac{12\pi k}{a^3}\frac{\varepsilon_\mathrm{d} Im(\varepsilon_\mathrm{m})}{|\varepsilon_\mathrm{m}-\varepsilon_\mathrm{d}|^2}\cdot|\alpha|^2 + \frac{8\pi}{3}k^4\alpha^2 \\ &\cong 4\pi k Im(\alpha). \end{aligned} \tag{12}$$

Here, $k = 2\pi\sqrt{\varepsilon_\mathrm{d}}/\lambda$ is the wave number in the medium, and both the static polarizability α_0 and the renormalized polarizability α are related by:

$$\alpha = \frac{\alpha_0}{1+\varphi(ka)\cdot a^{-3}\cdot\alpha_0}, \tag{13}$$

where the function $\varphi(ka) \cong -(ka)^2 - i\frac{2}{3}(ka)^3$ takes into account the radiative decay.

One should distinguish between the static polarizability and the renormalized polarizability. In the static case the extinction cross section will be [24]: $C_\mathrm{ext} \cong 4\pi k Im(\alpha = \alpha_0)$. One can see from the latter expression that the extinction spectrum has a strong resonance when:

$$\varepsilon_\mathrm{m}(\omega = \omega_\mathrm{res}) = -2\varepsilon_\mathrm{d}. \tag{14}$$

Although, the well-known Drude model describes the permittivity of bulky metal, we shall use it for estimating the resonance frequency

$$\varepsilon_\mathrm{m}(\omega) = \varepsilon_\mathrm{ib} - \frac{\omega_\mathrm{p}^2}{\omega(\omega+i\gamma_\mathrm{b})}, \tag{15}$$

where ε_ib is the contribution of the interband electronic transitions; ω_p is the frequency of volume plasma oscillations of free electrons; γ_b is the volume decay constant. Unlike the case of extended SPR, here we consider the exact Drude model because the metal permittivity has a main role in determining the LSPR frequency. Substituting Eq. (14) into Eq. (15) with the assumption that the significant contribution to the extinction spectrum caused by absorption, one can express the effective absorption cross section by the resonance frequency and the metal characteristics:

$$\begin{aligned} C_\mathrm{abs} &= \pi a^2 \frac{12ka\varepsilon_\mathrm{d}}{\left(2\varepsilon_\mathrm{d}+\varepsilon_\mathrm{ib}^2\right)} \\ &\cdot \frac{\omega_\mathrm{p}^2(\omega+\gamma_\mathrm{b})^2(\gamma_\mathrm{b}/\omega)}{\left(\omega^2+\gamma_\mathrm{b}^2-\omega_\mathrm{res}^2\right)^2+\omega_\mathrm{res}^4(\gamma_\mathrm{b}/\omega)^2}, \end{aligned} \tag{16}$$

where the resonance frequency ω_res and the corresponding resonance wavelength λ_res are given by:

$$\omega_\mathrm{res} = \frac{\omega_\mathrm{p}}{\sqrt{\varepsilon_\mathrm{ib}+2\varepsilon_\mathrm{d}}}; \qquad \lambda_\mathrm{res} = \lambda_\mathrm{p}\cdot\sqrt{\varepsilon_\mathrm{ib}+2\varepsilon_\mathrm{d}}, \tag{17}$$

here, λ_p is the plasma wavelength. Doyle [25] and Doremus [26] demonstrated that near the resonance, the absorption spectrum was approximately reduced to a Lorenzian

profile for the purpose of comparison between small metallic nanoparticles permittivity and the same metallic bulk permittivity.

The model of Drude is considered as a classical approach to describe the permittivity function of the metal and the dependence on the angular frequency. This model is usually used for bulk samples and it becomes problematic for very small particles. In this context, many studies were done on adjusting the classical model also to small nanoparticles. The modification was done by means of a correction function added to the permittivity function that considers the dependence on the particle size as it was done in several studies [27–29]. A comprehensive study was given in the review article of Khlebtsov [23].

So far, we have considered the case of small metallic spheres. In the general case, the LSPR can be excited in many other structures and shapes [30]. In most cases, metal particles are not isolated and not purely spherical. The fact that metallic particles aggregate and form a large and more complicated structures, does not change their strong absorption and scattering properties that we mentioned above, the difference may be in the number of the absorption peaks within the frequency range. One of the most general descriptions of a smooth and regular shape is an ellipsoid with three axes a, b, and c, $(a \geqslant b \geqslant c)$. If $b = c$, the ellipsoid becomes a prolate spheroid (cigar shape), and if $a = b$ the ellipsoid becomes an oblate spheroid (pancake shape). In a similar manner we can define polarizability for the structure in each direction of the major axes of the ellipsoid. Namely the polarizability that an applied electric field produces depends on the polarization direction of the external applied field, and consequently the resonance wavelength is determined for each axis when the electric field is polarized along that particular axis.

$$\alpha_i = 4\pi abc \left(\frac{\varepsilon_m - \varepsilon_d}{3L_i(\varepsilon_m - \varepsilon_d) + 3\varepsilon_d} \right), \tag{18}$$

where L_i, is a form factor of axis i when the electric field is polarized along this axis, α_i is the polarizability corresponding to the same axis. The geometrical factors L_i obeys the following rules $0 \leqslant L_i \leqslant 1$ and $L_a + L_b + L_c = 1$ when considering the axes a, b, and c. For a sphere $L_a = L_b = L_c = \frac{1}{3}$ due to spherical symmetry and then Eq. (11) is satisfied. The absorption cross section when the applied field is polarized parallel to the i axis will then be:

$$C_{abs} = kIm(\alpha_i) \tag{19}$$

Now, there are peaks in the absorption spectra [31] when $\varepsilon_m = \varepsilon_d(1 - 1/L_i)$. Since $0 \leqslant L_i \leqslant 1$, the term $(1/L_i)$ yields a wide range of frequencies (see Fig. 8). Similar behavior for nanodiscs and nanorods can be obtained because they

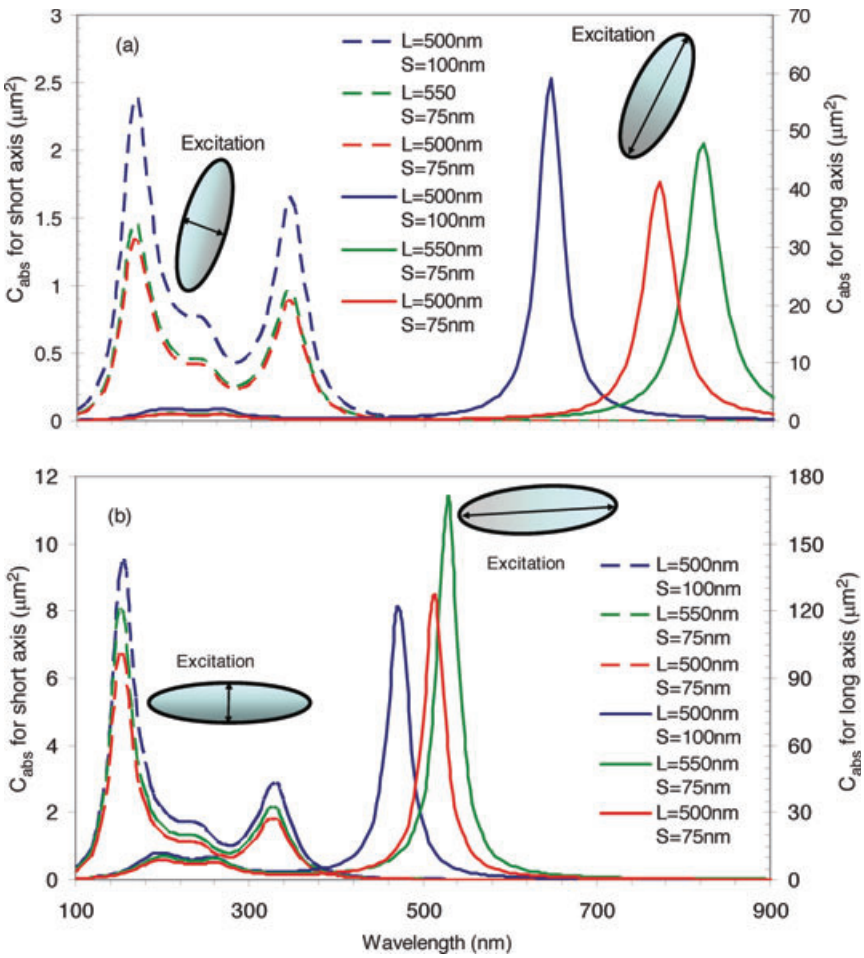

Figure 8 (online color at: www.lpr-journal.org) Absorption cross section for various sizes of spheroids: (a) Absorption cross section for prolate spheroid with different axes lengths. L Indicates the long axis of the spheroid and S indicates the short axis of the spheroid. For each combination of long and short axis, the absorption was calculated for both the polarization parallel to the long axis (solid curves) and parallel to the short axis (dashed curves). (b) Absorption cross section calculated for oblate spheroids. For each spheroid, the absorption was calculated for both the polarization parallel to the long axis (solid curves) and parallel to the short axis (dashed curves). The right vertical scale corresponds to the long-axis polarization, and the left vertical scale corresponds to the short-axis polarization.

are the limits of oblate and prolate spheroids, respectively. Furthermore, one can describe the response of structures in terms of ellipsoids with various shapes. One can design the resonance frequency by tailoring the shape and the size of the nanoparticles. In Fig. 8, the absorption cross section was calculated for silver nanospheroids with various shapes and sizes. The peak can be redshifted or blueshifted compared with the peak of a sphere by controlling the size and the shape of the spheroid. *The geometrical factors* L_i can be analytically calculated for standard smooth particles such as spheres, spheroids, ellipsoids, and cylinders. In the article by Stoner [32], the geometrical factors for ellipsoids were calculated, and the elliptic integrals can be explicitly solved for spheroids. In the case of a prolate spheroid with a being the major long axis and $b = c$ the equatorial short axes, we define $e \equiv \sqrt{1-(b/a)^2}$, and then the appropriate geometrical factors will be:

$$L_a = \frac{1-e^2}{e^2}\left[\frac{1}{2e}\ln\left(\frac{1+e}{1-e}\right)-1\right] \quad \text{and} \qquad L_b = L_c = \tfrac{1}{2}(1-L_a) \tag{20}$$

where L_a the geometrical factor when the excitation polarization is along the major long axis, and $L_b = L_c$ are the geometrical factors when the excitation along the equatorial short axes b or c. In the case of oblate spheroid, $a = b$ are the equatorial long axes, and c is the short polar axis, defining now: $e \equiv \sqrt{1-(c/a)^2}$, the appropriate factors will be:

$$L_c = \frac{1}{e^2}\left[1-\frac{\left(1-e^2\right)^{1/2}}{e}\arcsin(e)\right] \quad \text{and} \qquad L_a = L_b = \tfrac{1}{2}(1-L_c) \tag{21}$$

For other complicated geometries, numerical methods are needed to calculate the form factors such as the discrete dipole approximation (DDA) method, and the finite-difference time-domain (FDTD) method. In these methods, the particle is represented as a large finite number of elements, each of which can interact with the applied electric field. In the case of the DDA, this interaction is modeled in the frequency domain, whereas the FDTD evaluates this interaction in the time domain. In addition to modeling the extinction spectrum of nanoparticles, several equations describe how the LSPR is used for sensing. For example, the LSPR extinction resonance frequency is sensitive to the medium dielectric constant ε_{d} (or refractive index, n_{d}) according to Eqs. (17)–(19). Thus, changes in the environment (by adding adsorbate layer for example) cause an appropriate shift in the resonance wavelength. The relationship between perturbations in the dielectric medium refractive index Δn_{d} and the shift in the resonance wavelength $\Delta\lambda_{\mathrm{res}}$ is given by [33]:

$$\Delta\lambda_{\mathrm{res}} = S_\lambda \cdot \Delta n_{\mathrm{d}}\left[1-\exp\left(\frac{-2d}{l_{\mathrm{d}}}\right)\right], \tag{22}$$

where, S_λ is the bulk refractive index response of the nanoparticles (sensitivity); Δn_{d} is the change in refractive index induced by the adsorbate; d is the effective adsorbate layer thickness; and l_{d} is the characteristic EM field decay. The latter equation matches most of the experiment results, and forms the basis of the LSPR sensing mechanism.

2.3. Evanescent field sensing

At resonance, the reflectivity R reaches its minimum value, the intensity of the electromagnetic field reaches its maximum at the interface, see Fig. 9. Near the resonance angle, an extremely strong evanescent field at the metal/dielectric interface is generated by the surface plasmon wave. The unique characteristic of the generating evanescent field, where the field amplitude is greatest at the interface and exponentially decaying as a function of distance from the metal/dielectric interface, makes the SPR signal very sensitive to refractive-index changes in the vicinity of the metal surface. Figure 9 corresponds to the Kretschmann configuration that was illustrated in Fig. 2b.

The structure was optimized in order to obtain perfect resonance at 633 nm wavelength. The x component of the electric field is continuous; however the z component is discontinuous as expected. Due to the small dielectric constant of the analyte (ε_{a}) compared to that of the metal ($|\varepsilon_{\mathrm{m}}|$), $|E_z|$ has a strong enhancement at the metal/analyte interface. As shown in Figs. 9a and b the enhancement of the electric field is largest at the resonance compared to the cases near the resonance, where the resonance angle in this case is $\theta_{\mathrm{res}} = 54.619$ (deg). The incident magnetic field at the prism interface was set to unity, and the electric field intensities were normalized to the incident electric fields.

Since the SPR is accompanied by an enhanced evanescent field in the metal/analyte interface region, the sensor sensitivity for a perturbation in the analyte is determined by the field distribution in this region. According to Abdulhalim [34], the shift in the wavevector is proportional to the overlap integral, which in turn is proportional to the interaction volume V_{int}.

$$\delta k \approx \frac{k_i}{2}\frac{\int_{V_{\mathrm{int}}}\vec{E}_i^{*}\delta\varepsilon\vec{E}_f dr}{\int_V \vec{E}_i^{*}\varepsilon\vec{E}_i dr}, \tag{23}$$

where E_i, k_i are the electrical field and its wavevector before the variation in the analyte refractive index took place, while E_{f} is the field after the index perturbation and δk is the associated shift in the wavevector due to a change from ε to $\varepsilon + \delta\varepsilon$ in the analyte dielectric constant. Since δk expresses the change in the incidence angle or alternatively the change in the wavelength, then $(\delta k/\delta\varepsilon)$ represents the sensitivity of the sensor, which is proportional to the overlap integral in the numerator of Eq. (23) normalized to the total energy. Hence, to maximize the sensitivity one needs to maximize this integral, which can be accomplished by increasing the interaction volume, that is the evanescence depth, the SP propagation length along the surface or by increasing the field intensity in the analyte region. The last approach provides a physical interpretation to the sensitivity

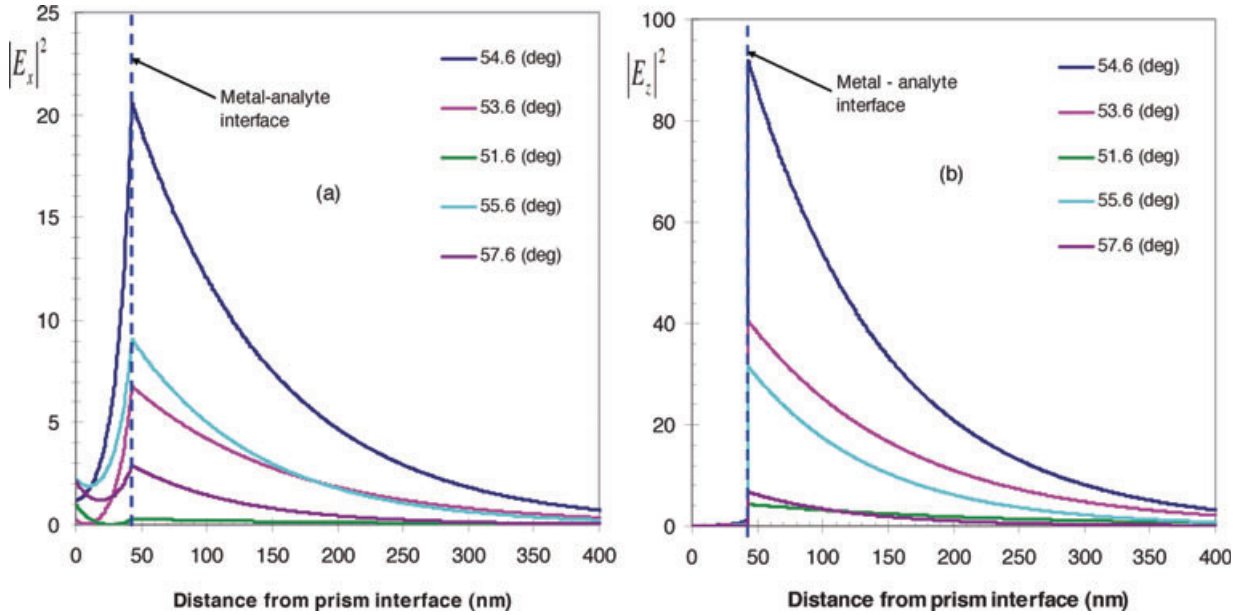

Figure 9 (online color at: www.lpr-journal.org) The electric field intensities, in the x direction (a) and in the z direction (b). The two graphs correspond to the conventional Kretschmann configuration shown in Fig. 2b with: 43 nm the silver layer thickness, 633 nm the incident wavelength, 1.33 the analyte refractive index and 1.732 the prism refractive index. The resonance angle obtained to the structure is 54.61 degrees.

enhancement that can be achieved by different techniques, as will be discussed in the following sections.

A full description of the electromagnetic field in multilayer structures within the SPR modes context was given by Davis [35] where the purpose was to obtain the eigenfunctions of the differential equation for the magnetic-field distribution and simultaneously the eigenvalues were derived from the dispersion relation. Chin and coworker [36], have presented calculations of electromagnetic field distribution using a matrix approach to extract the reflectivity of the multilayer structure. In both previous works [35,36], propagation matrices were used to calculate the two components of the forward- and backward-propagating magnetic-field amplitudes in an arbitrary layer from the boundary values of the aforementioned amplitudes. Ohta and Ishida [37] proposed a method to calculate the forward- and backward-propagating electric field without using inverse matrices; however, they described the full fields by exponential expressions, which may be problematic due to some numerical instability. Ekgasit et al. [38] and Hansen [39] used the characteristic matrix approach and the total transmission coefficients to explain their SPR spectroscopy experiments; however, they only emphasized absorbance aspects in multilayer system. A simplified three-step algorithm of field distribution calculations in a multilayer structure was presented recently by Shalabney and Abdulhalim [40] in which the authors verify the correlation between the sensitivity of an SPR sensor and the overlap integral in the analyte region. The algorithm is based on Abeles matrices using the reflection coefficient of the whole structure and propagation matrices for the layers. The modularity of the last algorithm makes it a very convenient tool for numerical implementations.

3. Sensitivity enhancement methods in extended SPR sensors

3.1. Metal-layer optimization

As was emphasized in Sect. 2, one of the widely used geometries is the Kretschmann configuration illustrated in Fig. 2a. Some of the reflectance profile parameters depend on the metal-layer features such as the minimum of the dip in the reflectivity profile $R_{\min}$, the full width at half-maximum ΔR, and the sensitivity of the sensor as was defined in Eq. (5). Furthermore, the protection layer responsible for the stability of the sensor is usually considered a very important characteristic when the sensor performance needs to be evaluated. To increase the signal-to-noise ratio (SNR), the thickness of the metal film is chosen in such a way that $R_{\min} \approx 0$. The corresponding value of the metal-layer thickness d_{m} can be estimated using numerical calculations. For silver and gold this value is on the order of 47 nm and 51 nm, respectively in the visible range (≈ 633 nm) and decreases on increasing wavelength.

Absorption in the metal layer influences significantly the width of the reflectance dip ΔR [41–43]. Since the dissipation in metals is determined mainly by the imaginary part of the refractive index n_{mi}, one may choose a metal type with low imaginary part to reduce the dissipation and consequently to obtain a narrower dip. Silver and gold are noble metals that satisfy this condition, while aluminum has a large imaginary part and exhibits wider dips compared to silver and gold. As a result, increasing the thickness of the aluminum layer causes the dip to disappear and a peak appears at the onset to the total internal reflection (TIR). Moreover, roughness of the surface causes the SP to scatter

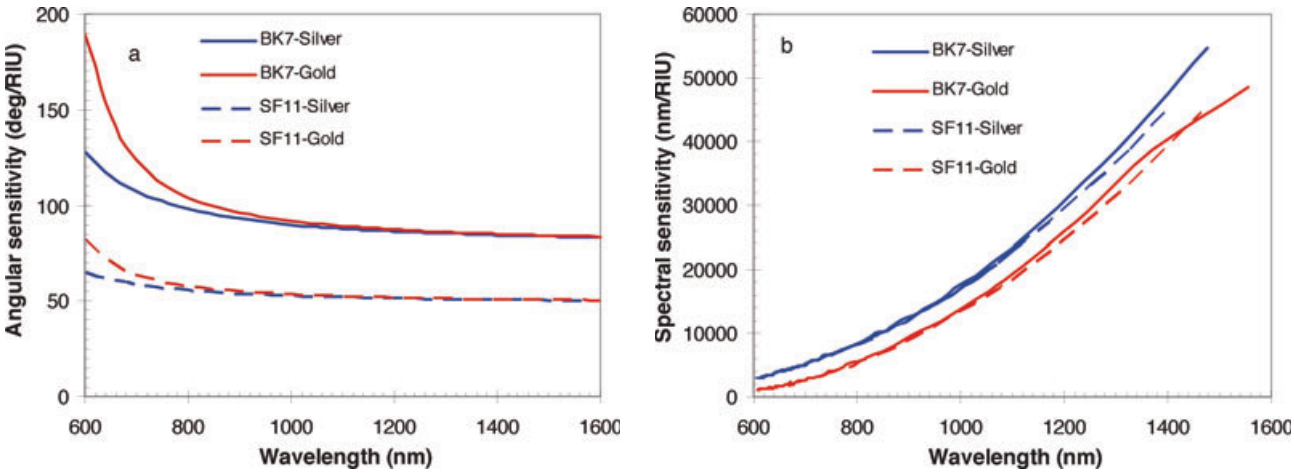

Figure 10 (online color at: www.lpr-journal.org) (a) The angular sensitivity versus wavelength for the conventional Kretschmann configuration shown in Fig. 2b. The sensitivity was calculated for both silver and gold with two types of prisms (BK7 with 1.51631 RI, and SF11 with 1.78301 RI). In each wavelength, the metal-layer thickness was optimized such that perfect resonance is obtained and the prism dispersion was neglected. (b) The spectral sensitivity for the same structure shown in Fig. 2b for both silver and gold metal layers with two types of prism (BK7 and SF11). For each wavelength, the incidence angle and the metal-layer thickness were chosen to obtain perfect resonance.

and change direction; as a result the dip becomes wider. Optimizing the metal layer to improve the sensor performances by computational means was done early on by Gent and coworkers [44]. Snopok [45] and coworkers showed that a simple procedure of low-temperature annealing (at ≈ 120 °C) can provide optimum parameters of the thin gold film as a physical transducer in an optical SPR biosensor. Recently, high-quality patterned metals were fabricated using template stripping with precisely patterned silicon substrate to obtain ultrasmooth pure metal films with grooves [46].

When considering the effect of the metal type on the sensitivity of the SPR sensors, a small confusion usually appears when distinguishing between silver- and gold-based sensors sensitivity. Early on, a comparison was reported by Homola [47] in which he determined that silver-based sensors have higher sensitivity than gold-based counterpart sensors. The last statement is not sweeping and it is valid only for spectral sensitivity, with the interpretation that silver has a higher real part of the dielectric permittivity than gold, thus its sensitivity is higher. On the other hand, if we consider the angular sensitivity of the sensor we see that the opposite is valid, that is gold-based SPR sensors have a higher angular sensitivity. This was clarified later by Homola [21], as can be seen in Fig. 10. One can use an approximate formula of the spectral sensitivity $S_\lambda \cong S_{\lambda\_\mathrm{app}} = \frac{2\varepsilon_{\mathrm{mr}}^2}{n_a^3\left|\frac{d\varepsilon_{\mathrm{mr}}}{d\lambda}\right|}$, in which the dispersion of the prism is neglected.

Using silver as the transducer layer has the advantage of high spectral sensitivity but with poor chemical resistance as it deteriorates upon contact with the atmosphere or some chemicals. As a result, gold is commonly used as the transducer metallic layer due to its stable performance and high chemical resistance.

As a compromise between high sensitivity and chemical stability, a bimetallic based SPR sensor was proposed by Yuan and coworkers [48]. The device in Fig. 11a is made of double silver-gold layers and based on the conventional Kretschmann configuration. The combination of 21 nm silver with 23 nm gold bimetallic layer promises a high chemical stability with reasonable sensitivity compared with a single gold layer.

The additional silver layer causes a narrower dip and a higher resolution. As can be seen from Fig. 11c, the full width at half-maximum (FWHM) obtained experimentally by the double-layer design is narrower (≈ 4.8 times improvement) than the single gold layer configuration. As a result, a much better resolution and higher-precision sensor can be produced by using the double-layer arrangement in comparison to the single-layer profile. The influence of using double metallic film on the sensitivity and stability of the sensor was also investigated by Lecaruyer and coworkers [49]. Since silver, and similarly gold, has poor adherence with glass; therefore chromium or titanium must be inserted to fix the silver or gold layer to the glass substrate. Because of this addition some small loss in the sensitivity appears. In the last work, the use of metamaterials was also investigated to gain improved sensitivity, which shows that these sensors still have a potential for sensitivity improvement.

3.2. Effect of prism index and dispersion

Considering the Kretschmann configuration, the resonance condition obtained by equating the SP wavevector and the emerging light wavevector is given by Eq. (3) which can explicitly be written as $k_0 n_p \sin\theta = k_0\sqrt{\frac{\varepsilon_{\mathrm{mr}} n_a^2}{\varepsilon_{\mathrm{mr}}+n_a^2}}$ where n_a and n_p are the analyte and the prism refractive indices, respectively, and $\varepsilon_{\mathrm{mr}}$ is the real part of the metal refractive index. By analyzing the last condition one can conclude that the coupling condition is fulfilled if $|\varepsilon_{\mathrm{mr}}|$ is higher than

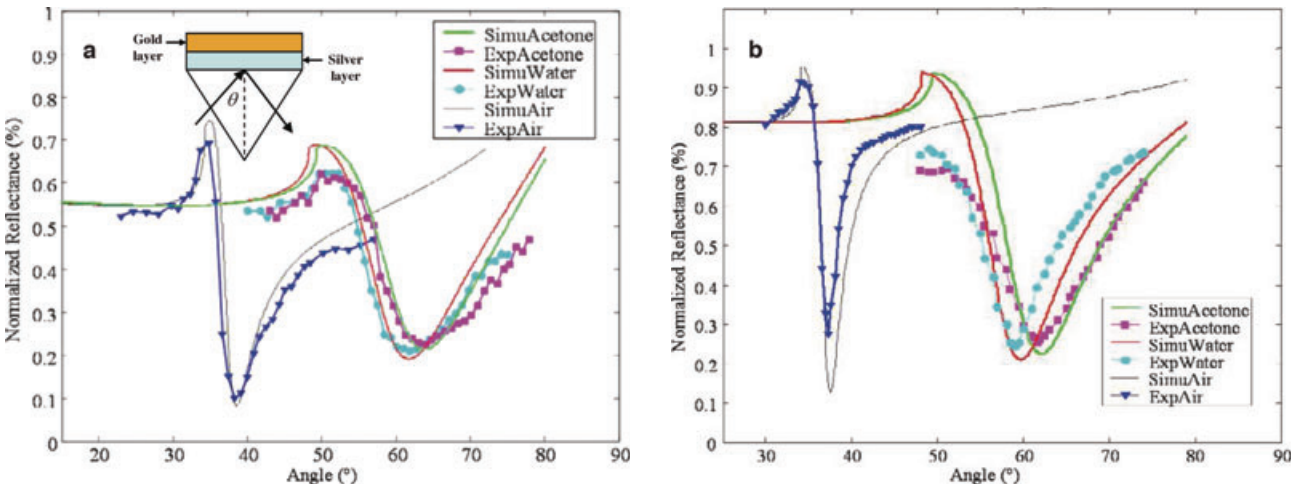

Figure 11 (online color at: www.lpr-journal.org) The inset shows the two layer metal film configuration (a) comparison of the SPR curves for the simulation and the experimental results for the single gold layer configuration with air, water and acetone analyte. SimuAir, SimuWater, and SimuAcetone refer to simulation results obtained for the air, water, and acetone, respectively. ExpAir, ExpWater, and ExpAcetone refer to the experimental results obtained for the air, water, and acetone, respectively (b) comparison of the SPR curves of the double metal layer configuration for air, water, and acetone analyte. (Reproduced from [48], X.-C. Yuan et al., Part (a) was taken from Fig. 5, and part (b) was taken from Fig. 7 of the original article).

$\left(n_a^2 \cdot n_p^2/n_p^2 - n_a^2\right)$, which corresponds to the resonance angles of incidence $\theta \leqslant 90$. When wavelength decreases, $|\varepsilon_{mr}|$ also decreases and approaches this critical value. At a certain (cutoff) wavelength, an SPW can no longer be excited. For wavelengths longer than the cutoff wavelength, the resonance wavelength increases when increasing the analyte refractive index and decreases for smaller analyte refractive index.

The expression for the sensitivity of the resonance angle to variations in the analyte refractive index is given by Eq. (6). In Fig. 10, the angular sensitivity is plotted as a function of the operation wavelength. The sensitivity exhibits high values for short wavelengths, and in this region of the spectrum the sensitivity is governed by a singularity occurring when $\left(|\varepsilon_{mr}| = \frac{n_a^2 \cdot n_p^2}{n_p^2 - n_a^2}\right)$. For long wavelengths, the sensitivity does not vary considerably with wavelength. If an angular SPR sensing device operates far from the cutoff, the sensitivity can approximately be expressed as:

$$S_\theta \equiv \frac{d\theta}{dn_a} \approx \frac{1}{\sqrt{(n_p^2 - n_a^{2)}}}. \qquad (24)$$

Therefore, the sensitivity at high wavelengths depends mainly on the refractive-index contrast between the prism and the analyte, increasing when decreasing contrast. Actually, the relationship between the sensitivity and the prism refractive index does not only exist in the region of long wavelengths, but it is also valid at smaller wavelengths (see Eq. (6)). Furthermore, this relationship is valid for spectral sensitivity as well as angular sensitivity. This correlation can be seen through the expression of spectral sensitivity and Fig. 10, in which the sensitivity for two types of prisms is shown.

Sensitivity enhancement of spectral biosensor by modifying the prism refractive index was presented in the work of Yuk et al. [50]. Sensitivity was modulated by the refractive index of the sensing prism of the spectral SPR biosensors with the same incidence angle. The sensitivity of a spectral SPR biosensor with fused silica prism (1.458 refractive index at 589 nm) was 1.6 times higher than that with a BK-7 prism (1.517 refractive index at 589 nm) at the same incidence angle 46.2°. The authors attributed the enhancement in the spectral sensitivity not to the direct influence of the prism refractive index in the expression of the spectral sensitivity as it is given in Eq. (6), but to the difference in the resonance wavelength obtained with each prism. As shown in Fig. 12c, the resonance wavelength for the BK-7 prism is smaller than that of the fused silica prism, and since the sensitivity scales monotonically with the operation wavelength the sensitivity will be much higher in the case of a prism with smaller refractive index. Physically, the authors interpreted the increase in the sensitivity to the increase in the penetration depth of the evanescent field for the prism with the smaller refractive index. Although the penetration depth scales with the operation wavelength according to Raether [4], the effect of increasing the penetration depth on sensitivity enhancement is still inadequate because in the case discussed by Yuk et al.., the thickness of the proteins layer is very thin, typically $\leqslant 10$ nm. Furthermore, increasing the wavelength is accompanied not only with a larger penetration depth, but also with depletion in the field intensity at the interface between the metal and the dielectric. For our evaluation, the essential effect of prism refractive index on spectral sensitivity should be reinvestigated and several parameters may be examined.

Sensitivity enhancement by modifying the prism refractive index under angular interrogation was also presented by Gupta and Kondoh [51]. In this paper, the role of prism

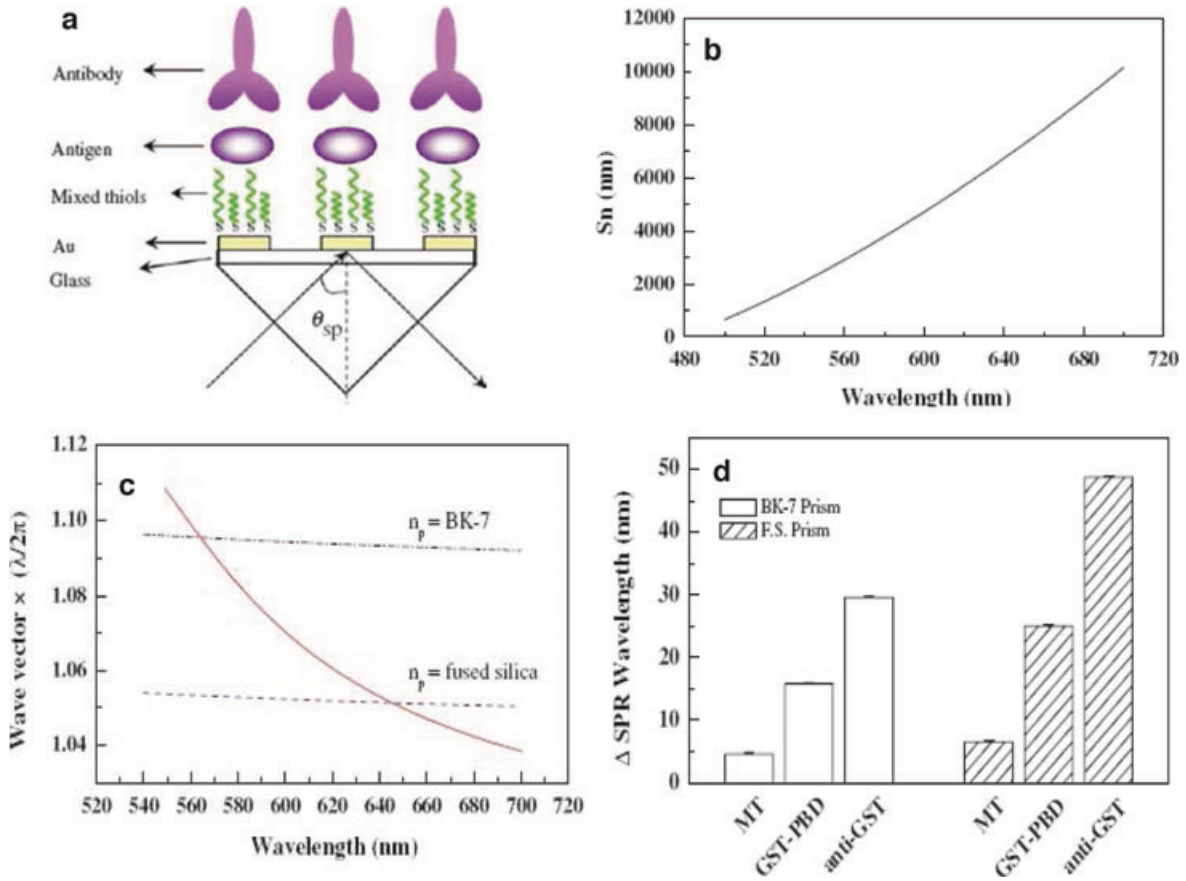

Figure 12 (online color at: www.lpr-journal.org) (a) surface structure of protein arrays for spectral SPR biosensor (b) sensitivity S_n was calculated as a function of wavelength for the refractive index of air. Gold metallic layer and BK-7 prism were considered (c) the wavevector of the surface plasmon is displayed by a solid line. The incident light wavevector parallel to the surface is displayed by a dashed-dotted line for BK-7 prism, and by a dashed line for the fused silica prism with an incidence angle of 46.2°. The resonance wavelengths were calculated at the intersection point between the solid line and the dashed-dotted line for BK-7 prism, or the dashed line for fused silica prism (d) net shifts of resonance wavelengths were calculated by subtracting the resonance wavelength of the gold surface from that of each modified surface. For comparison, the resonance wavelength shifts are given for both the spectral SPR biosensor with BK-7 prism and the counterpart sensor with fused silica prism (reproduced from [50] J. S. Yuk, et al. Part (a) was taken from Fig. 1, parts (b) and (c) were taken from Fig. 2 and part (d) was taken from Fig. 5 of the original article).

material in sensor design was described both theoretically and experimentally. The analyses were carried out for three prisms with different refractive indices and the reflection spectra were studied under the angular interrogation mode. The experimental values of angular sensitivity increase from 94.46 deg/RIU to 204.41 deg/RIU on changing the refractive index of the prism from 1.597 to 1.456 without changing the other parameters (see Figs. 13a and b).

The adverse affects of working with low refractive index prisms are relatively low dynamic range of the sensor and a large FWHM of the SPR reflection spectra, which must also be considered before selecting the prism material. The authors did not give an explicit interpretation to the enhancement in the sensitivity due to decreasing the prism refractive index. Overall, the choice of prism material proves to be a vital design parameter and is significant for tuning and optimizing the sensor performance. Recently, Shalabney and Abdulhalim [40] explained the sensitivity enhancement in terms of the enhancement in the electric field near the metal/analyte interface. We have used the same algorithm and the parameters of Figs. 13a and b to draw Figs. 13c and d for the field distribution at two different wavelengths. Figure 3c demonstrates the effect of the prism index on the sensitivity, while Fig. 13d explains the effect of the wavelength.

3.3. Addition of top nanodielectric layer

In this section we consider the addition of a thin dielectric layer with a high refractive index on top of the metal layer. We emphasize that the added layer is very thin (typically 10 nm) and with high refractive index. One should distinguish this case from the case of coupled plasmon-waveguide resonance (CPWR). CPWR biosensors incorporate a thick waveguide layer (typically 500 nm) beneath the surface of the conventional SPR biosensor [52, 53]. Unlike the conventional SPR biosensors, whose reflectivity demonstrates a

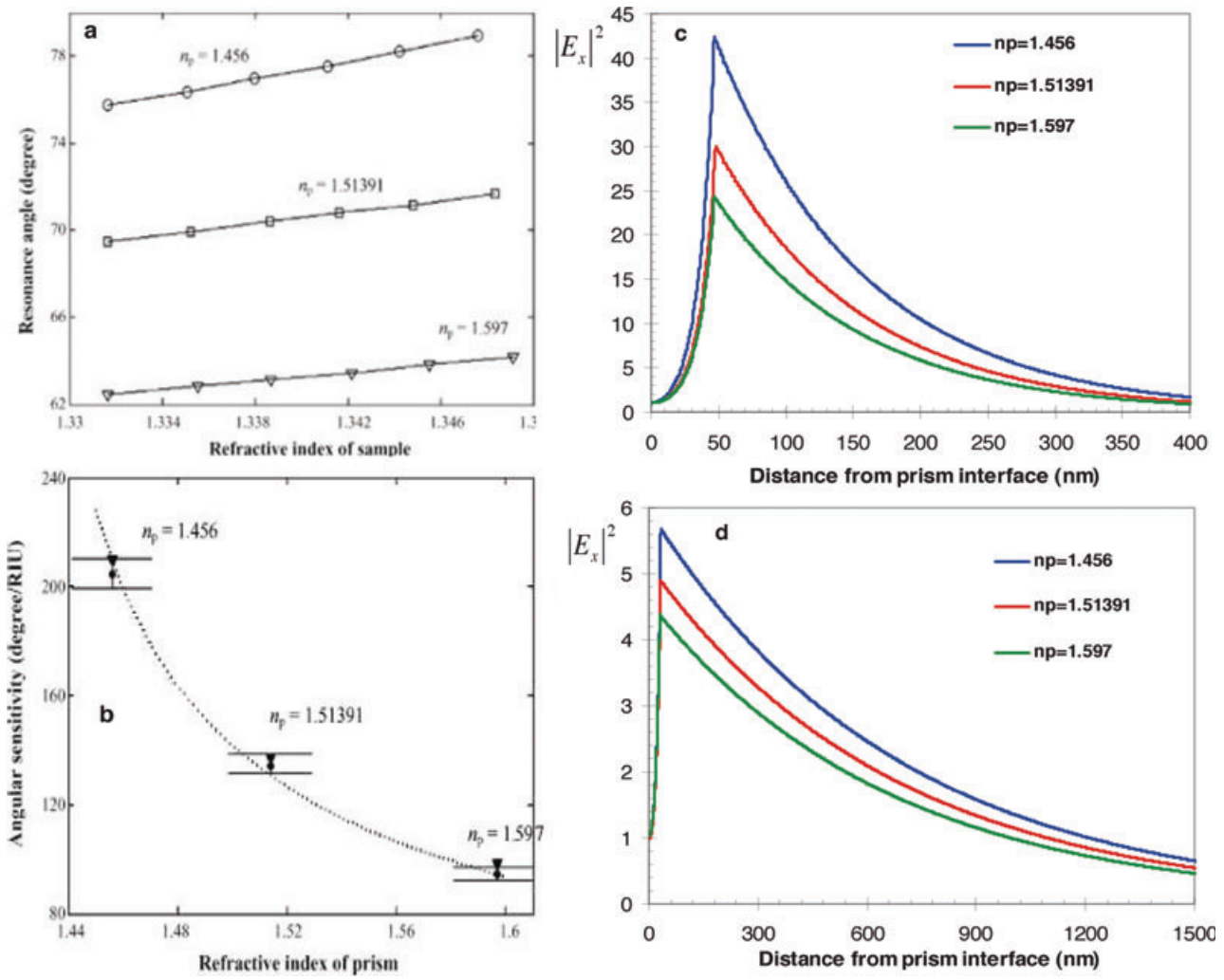

Figure 13 (online color at: www.lpr-journal.org) (a) Plot of resonance angle and ethanol solution with different concentrations and refractive indices for three different prisms (b) variation of angular sensitivity as a function of the refractive index of the prism: experimental values (filled circles), analytical values (dashed curves), and numerical values (filled triangles). The two horizontal lines correspond to the range of values obtained for fives sensor chips (Parts (a) and (b) were reproduced from Figs. 8 and 9, respectively, of [51], G. Gupta et al.). (c) and (d) show the x component of the electric field distribution for the three prism indices used in (a) and (b) for two wavelengths: 633 nm and 1550 nm respectively. In (c) and (d) the silver film thickness was varied between the different prisms to obtain the optimum SPR: (c) 47 nm, 48 nm, 47 nm, (d) 33 nm, 32 nm, 30 nm for the prism indices 1.456, 1.51391 and 1.597, respectively.

dip only in the TM mode, the interference in the waveguide layer causes a dip both in the TE and TM modes in the CPWR device [54]. Although CPWR sensors exhibit sharp dips and improve significantly the SNR of the measurement, their sensitivity is less than that of conventional SPR devices by an order of magnitude since the biosensing surface is located at a considerable distance from the SPs that exist on the interface between the metal and the waveguide layer [55, 56].

The contribution of a thin dielectric top layer to the sensitivity enhancement of SPR sensor was reported for the first time by Lahav et al. [57]. The nearly guided wave SPR (NGWSPR) sensor is similar to the conventional SPR sensor with an addition of a thin dielectric layer between the metal layer and the cover material to be sensed. The thickness is not enough to support a guided mode, see Fig. 14. The introduction of thin ZrO_2 layer on top of the silver film was done by Gent et al. [44] for the purpose of protection and they observed some enhancement of the sensitivity, although it was small because ZrO_2 has a relatively small index. In the NGWSPR the dielectric layer that was used is silicon with a thickness of about 10 nm as the refractive index of the silicon is relatively high.

Since silver has poor chemical stability, the silicon layer that was added to the sensor protects the metal layer as well as improving significantly its sensitivity. The sensitivity in the NGWSPR case was 4 times larger than the sensitivity of SPR sensor and 1.5 times larger than the sensitivity when a ZrO_2 layer is used. The origin of the enhancement mechanism is in the combination between the SPR phe-

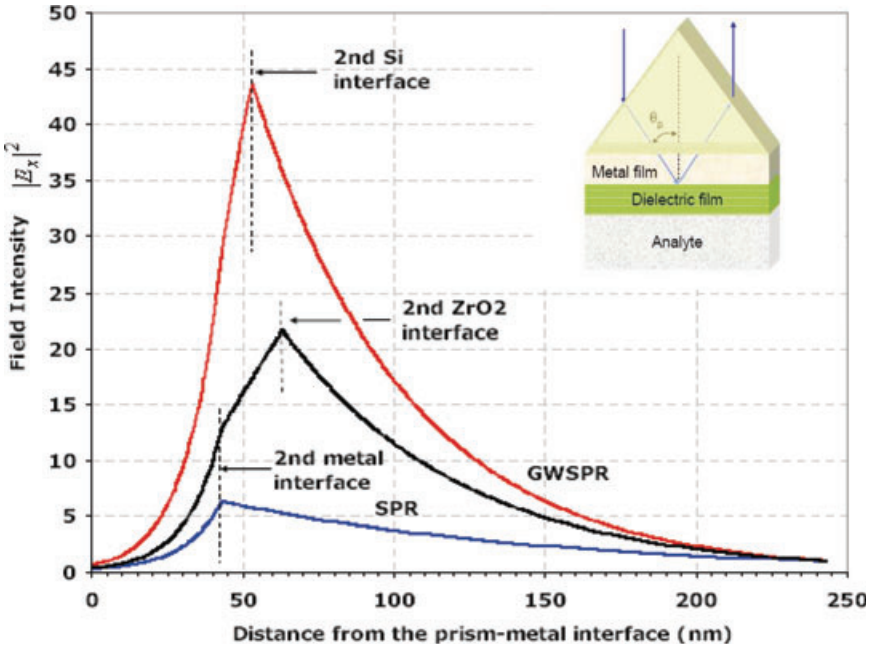

Figure 14 (online color at: www.lpr-journal.org) the inset shows schematic illustration of the NGWSPR configuration. Electric-field intensity distribution versus the distance from prism metal interface for three cases: (1) conventional SPR configuration with no top layer and 43 nm silver layer with 1.33 analyte refractive index, 20 nm thickness of ZrO_2 layer with 2.1517 refractive index on the top of 43 nm silver layer and with 1.33 analyte refractive index, 10 nm Si layer on top of 43 nm silver. For the three cases the wavelength is 633 nm, and the prism refractive index is 1.73205 (reproduced from [58], A. Lahav et al. The inset and the graph were taken from Figs. 1 and 4, respectively, from the original article).

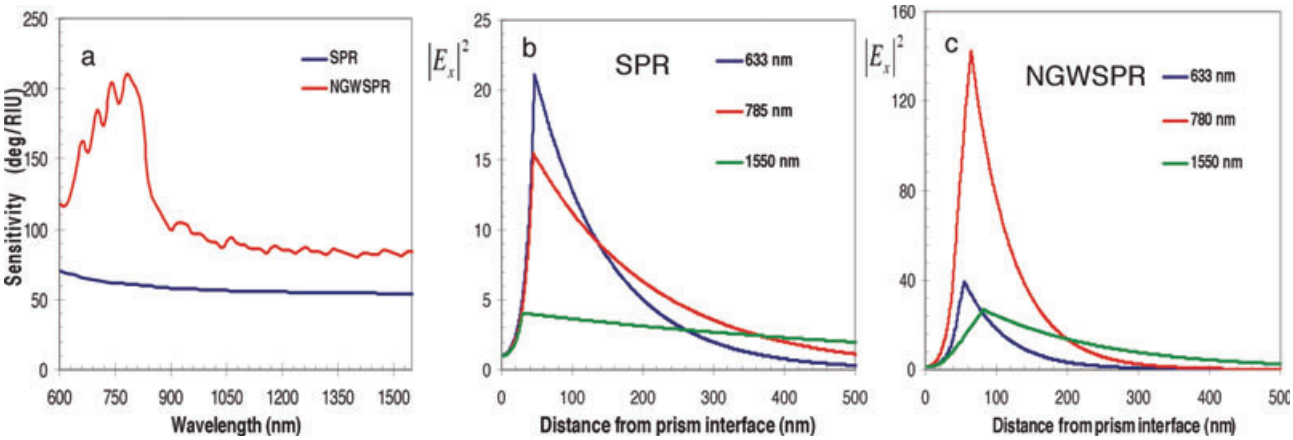

Figure 15 (online color at: www.lpr-journal.org) (a) Sensitivity as a function of wavelength for SPR versus NGWSPR. The prism refractive index is 1.732 and the analyte refractive index is 1.33. For SPR the metal layer was optimized to obtain a perfect resonance. For NGWSPR, both the metal layer and the silicon layer thicknesses were optimized to obtain a resonance with minimum reflectivity in the resonance $R_{\min} < 0.01$. In (b) and (c) the electric-field distribution is shown corresponding to the SPR and NGWSPR cases for different operation wavelengths. The silver layer thicknesses that were chosen to obtain resonance are 47 nm, 45 nm and 30 nm in (b) and 47 nm Ag/8 nm Si, 45 nm Ag/20 nm Si and 30 nm Ag/20 nm Si for the three wavelengths indicated on the figure, respectively, from the short to the long wavelength. The prism and the analyte refractive indices are 1.732 and 1.33, respectively, in both (b) and (c).

nomenon and the NGWSPR configuration, which enables the surface plasmons to spread along the dielectric layer. When the dielectric layer has a large refractive index it can support guided waves for smaller thicknesses. Being thin enough, causes a larger fraction of the evanescent field to be in the analyte region. Hence, together with the fact that the wave is partially guided (below the cutoff of the TM mode), the whole interaction volume is larger, thus increasing the sensitivity. This can be understood from the fact that the sensitivity related to the overlap integral of the electrical intensity in the analyte region, which is in turn proportional to the interaction volume [34]. From Fig. 14 one can see that silicon causes the largest enhancement for the electric field at the interface of the analyte and allow a maximum overlap integral [58]. One can see from Fig. 15a that the addition of a silicon layer with appropriate thickness can significantly improve the sensitivity of the sensor. Such an improvement is accompanied with widening of the dip and shifting the resonance angle towards 90 degrees. The explanation is again correlated nicely with the field-distribution enhancement as shown in Figs. 15b and c using the algorithm of Shalabney and Abdulhalim [40]. Near the wavelength of 780 nm the sensitivity is maximum in the NGWSPR case and the field at the silver/analyte interface is also maximum. Although at 1550 nm the penetration depth is higher, the overlap integral in Eq. (23) is determined both by the field

distribution and the penetration depth. In reference [40] the correlation between the overlap integral and the sensitivity was demonstrated quantitatively.

3.4. Addition of gratings on top of the metal layer

As mentioned in Sect. 2.1, the surface plasmon can be excited by gratings as well as by prism coupling. By adding a corrugation (gratings) to the metal, two things can be accomplished: the grating provides the required momentum matching to the incidence light and couples it to the surface plasmons; and secondly, the gratings can perturb the propagation of the surface plasmon. There are two configurations used for grating coupling: direct and indirect. In the direct configuration the light is incident directly onto the metal/dielectric interface from the dielectric side [59] (see Fig. 2b), while in the indirect configuration the light is incident through a prism [60, 61] (see Fig. 16a). The indirect configuration caught the interest of many researchers because it allows coupling of light to the surface plasmon by the TIR configuration and then perturbing it by adding the grating [62, 63]. SP waves that propagate along the grating vector will experience back reflections. If the period of the grating corresponds to the Bragg condition then a bandgap will form where no plasmons are permitted to propagate.

Mainly, the bandgap is used to control the surface plasmon propagation direction similar to the use of waveguides and photonic crystals in telecommunications. In the context of biosensing, Alleyne et al. [64] showed theoretically that the surface plasmons on the edge of the bandgap experience an increased sensitivity to bulk index changes in the dielectric above the grating. By choosing various gratings with different heights and periods, the authors maintained the bandgap to be near the excitation wavelength. By designing the operating point of the sensor to be near the bandgap, the sensitivity was improved by a factor of six compared with the sensitivity of the conventional SPR sensor with flat metallic layer (see Fig. 16).

An extinction-based transmission-type SPR sensor is also plausible and has been extensively investigated to study spectral outcoupling of surface plasmons excited in nanostructures often using a wavelength-scanning setup. One of the significant limitations of this coupling is the transmission power efficiency to associate them with other external devices.

By using the Kretschmann configuration with a dielectric grating on a silver film, an outcoupling efficiency of 50% was presented and proved experimentally by Park et al. [65], 68% was obtained by Lenaerts et al. [66], and even 72% was predicted numerically by Shen et al. [67]. Numerical investigation of the transmission-type SPR sensor with dielectric and metallic gratings was done by Byun [68] and coworkers. They showed that a metallic grating has the advantage of narrower transmission peaks and a high sensitivity compared with a dielectric grating but with lower maximum transmittance. A similar comprehensive work was done by Bin et al. [69] in which they investigated a transmission-type SPR sensor with metallic dielectric mixed gratings, compared to the conventional dielectric gratings-based structure. It is found that the transmittance efficiency and the FWHM of the transmission curve can be modulated by increasing or decreasing the metallic part. Therefore, the appropriate proportion of the metal part will induce an enhancement factor of the sensor performance (see Fig. 17). Furthermore, this structure will also bring enhancement of resonant angle shift, which can be explained by plasmonic interpretation based on a surface-limited increase of interaction area and excitation of localized surface plasmons (LSPs).

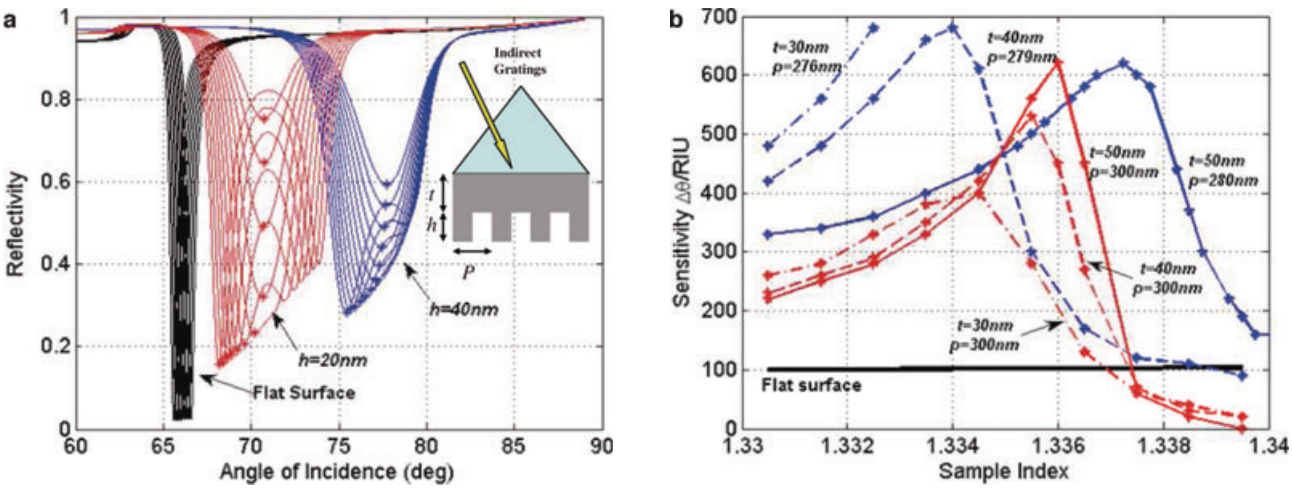

Figure 16 (online color at: www.lpr-journal.org) The inset shows combined TIR and indirect grating coupled SPR (a) reflectivity dips for a flat surface (black curves) and two gratings, the first with $h = 20$ nm (the red curves), and the second with $h = 40$ nm (the blue curves) both with $t = 50$ nm and with sample index values from 1.33 to 1.34. The asterisk shows the curve minima (b) sensitivity versus sample index for a flat surface (black solid line) and various gratings. The red curves represent grating with $h = 20$ nm and the blue curves with $h = 40$ nm. The period required to keep the band edge near $\lambda = 850$ nm is also noted (Reproduced from [64], C. J. Alleyne, et al. Parts (a) and (b) were taken from Figs. 6 and 7, respectively, from the original article.)

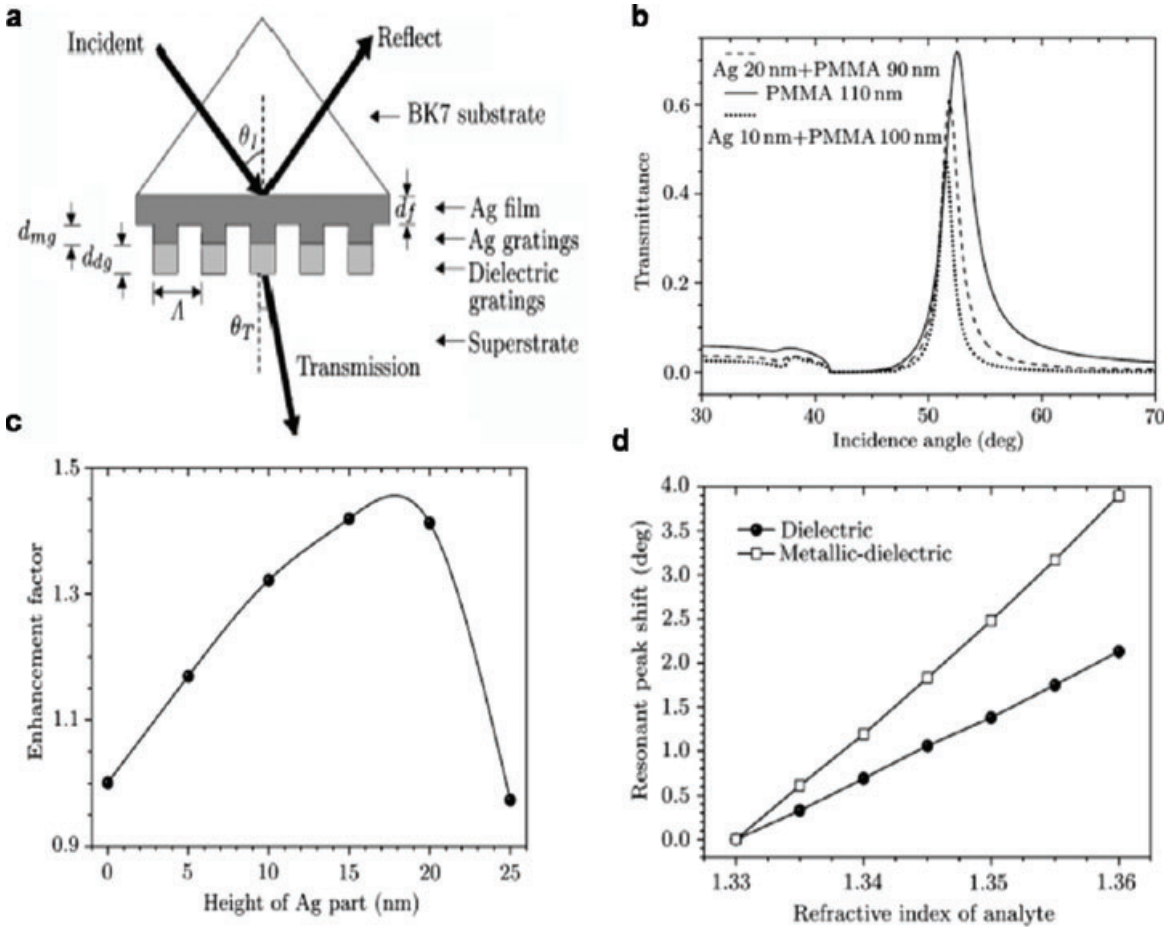

Figure 17 (a) Schematic of metallic–dielectric mixed gratings based SPR structure (b) transmittance curves (1T) for air substrate as a function of incidence angle. The grating thickness is fixed on 110 nm with three different proportions between metal and dielectric (110 nm PMMA, 10 nm metal and 100 nm PMMA, 20 nm metal and 90 nm PMMA) (c) influence of the Ag part on enhancement factor of the sensor merit in air substrate. The metal height varies from 0 to 25 nm when the total grating height is fixed at 110 nm. (d) Resonant peak shift of conventional dielectric gratings (110 nm PMMA) in comparison with a dielectric–metallic mixed one with 20 nm Ag and 20 nm PMMA. (Reproduced from [69], W. Bin et al., Parts (a), (b), (c), and (d) were taken from Figs. 1, 2, 4, and 5, respectively, of the original article).

3.5. Long-range SPR

The long-range SPR (LRSPR) biosensors based on the Kretschmann configuration comprise four basic layers, namely the prism ε_p, the dielectric buffer layer (ε_b, d_b), the metal layer (ε_m, d_m), and the analyte ε_a. In these devices, the thin metal layer is separated from the prism by an additional dielectric buffer layer [70–73] as shown in Fig. 18a. If the dielectric constant of the dielectric buffer layer is very similar to that of the intended analyte, and is lower than that of the prism, a symmetric environment is achieved on either side of the metal thin film. Ideally, the dielectric constants of the dielectric buffer layer and the analyte will be equal, i. e. $(\varepsilon_b = \varepsilon_a)$. If the thickness of the thin metal layer is such that $k_{zm} \cdot d_m \ll 1$, the resulting symmetric configuration causes the same surface plasmon wave to exist on both sides of the thin metal layer, and interaction then takes place between the two SP waves at both surfaces. Under these conditions, the surface plasmon frequency divides into $\omega_{\pm}$. The electric field of the high-frequency ω_+ mode is asymmetric to the center plane of the thin metal layer, while the electric field of the low-frequency ω_- mode is symmetric to the same plane. The short-range dispersion relationship L_+ and long-range dispersion relationship L_- for this symmetric configuration are given by Raether [4].

$$\begin{aligned} \omega_+ : L_+ &= \varepsilon_m k_{za} + \varepsilon_a k_{zm} \cdot \tanh\left(\frac{k_{zm} d_m}{2i}\right) = 0, \\ \omega_- : L_- &= \varepsilon_m k_{za} + \varepsilon_a k_{zm} \cdot \mathrm{ctgh}\left(\frac{k_{zm} d_m}{2i}\right) = 0. \end{aligned} \tag{25}$$

In the equations above, ω_+, represents the short-range surface plasmon frequency while ω_-, denotes the long-range surface plasmon frequency mode. These modes are characterized by greater and lesser loss, respectively. Compared to the conventional SPR biosensor, the propagation length of the long-range surface plasmon is increased by a factor of approximately 10 times. The incident beam energy is

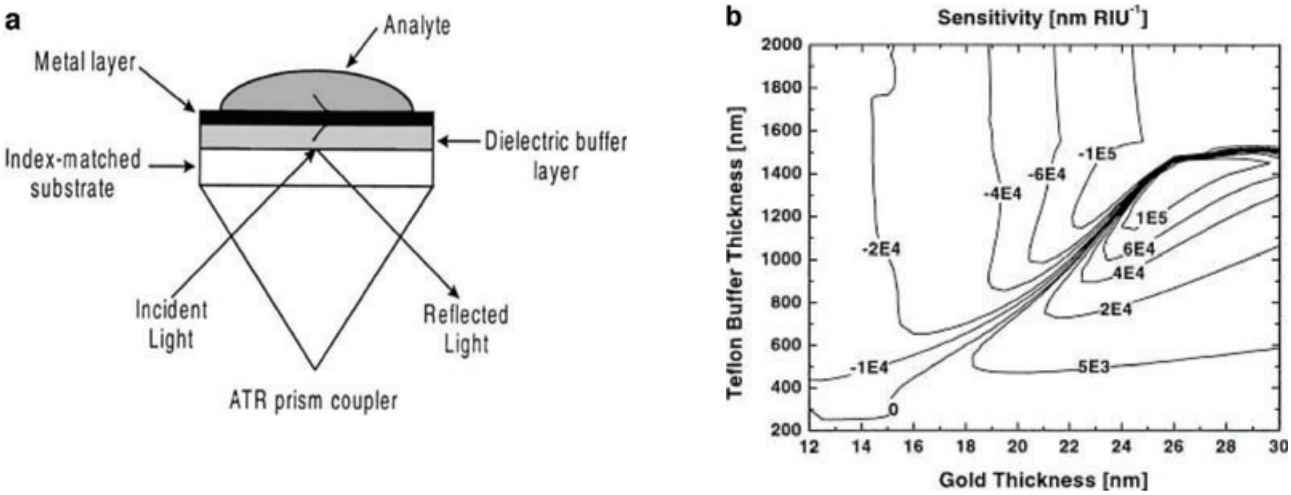

Figure 18 (a) Configuration of LRSPR sensor using a removable sensor substrate (b) Design curves as a function of metal and buffer layer thickness for an LRSPR sensor using an SF14 glass substrate and a Teflon AF-1600 buffer layer with water as the analyte. The operating angle was optimized at each point to achieve the greatest coupling into the resonance (operating wavelength 500–1000 nm). (Reproduced from [74], G. G. Nenninger, et al. Parts (a) and (b) were taken from Figs. 4 and 6, respectively, of the original article).

more concentrated, and the depth-to-width ratio of the resonance dip is increased. The reflectivity dip at a lower angle has a smaller FWHM and hence indicates the long-range surface plasmon mode, while the dip at a higher angle is indicative of the short-range surface plasmon mode. Nenninger et al. [74] showed that for specific combinations of metal thickness and buffer layer thickness, the magnitude of the sensitivity can be extremely high, on the order of 1×10^5 nm/RIU when the buffer layer made of Teflon AF-1600 compared with a sensitivity of 1.4×10^4 nm/RIU for a conventional prism-coupled wavelength-interrogation SPR sensor operating at 850 nm (see Fig. 18b).

While in the work of Nenninger a seven-fold improvement in the spectral sensitivity was reported, Chien and Chenb [75] showed that just a slight improvement is achieved in the LRSPR device compared to the conventional SPR configuration with spectral interrogation, and a lower sensitivity when the angular interrogation is considered. The difference between the last two studies is attributed to the fact that in Chien and Chenb's study the authors focused upon the variation in refractive index and thickness of the biomolecular layer, whereas in Nenninger's work the researchers considered variations in the refractive index of the analyte layer solution. This difference in the format of the sensitivity definition leads to the difference in the reported values of sensitivity. The wavelength interrogation induces variations in the dielectric constants of the sensor layers (metal layer, buffer layer, analyte) which have a significant effect on the symmetric environment of the LRSPR biosensor. Even though the LRSPR sensor has a slightly higher sensitivity and a much narrower dip than the conventional SPR sensors, its requirement of a symmetric configuration is a significant drawback in environmental detection of various biomolecules, and hence tends to restrict its use in practical biosensing applications. By exploiting the very narrow dip in the LRSPR configuration and advanced photonic components Slavik and Homola [76] reported an SPR sensor with very low detection limit (2.5×10^{-8} RIU). Within another experimental study, Vala and coworkers [77] reported an SPR sensor based on spectroscopy of LSPR for the detection of large analyte such as latex beads and bacteria. In the LSPR sensor a spectral sensitivity of 59 000 nm/RIU was measured, which is about 8-fold higher than the sensitivity of a conventional SPR sensor when the resonance was obtained close to 850 nm.

3.6. Sensitivity in the infrared versus the visible range

Under our previous definition of the angular sensitivity, which was given in Eq. (5), the sensitivity decreases when increasing the operation wavelength, as can be seen from Fig. 10. In general, the performance of any SPR sensor is determined in terms of two aspects. First, the shift in resonance angle $(\delta\theta_R)$ for a given change (δn_a) in the sensing layer refractive index should be as large as possible. Secondly, the FWHM corresponding to the SPR curves $(\delta\theta_{HM})$ should be as small as possible so that the error in determining the resonance angle is minimal.

Taking both these aspects into account, Jah and Sharma [78] defined a performance parameter called intrinsic sensitivity S_i, which is equivalent to the figure of merit (FOM) as it is commonly defined [68,130,132]. The parameter S_i is directly proportional to the shift in resonance angle $\delta\theta_R$ and is inversely proportional to the average FWHM $\delta\theta_{HM}$ of two SPR curves (see Fig. 19). Mathematically, the intrinsic sensitivity or alternatively the FOM of the sensor is defined by:

$$S_i = \frac{\delta\theta_R}{\delta\theta_{HM}}. \tag{26}$$

When adopting the last definition of the sensitivity, the behavior of the sensitivity versus wavelength will take a different form. If we do not neglect the imaginary parts of

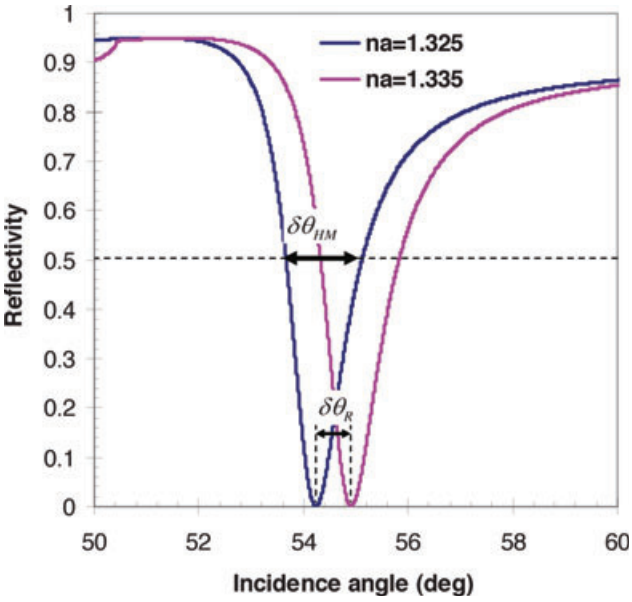

Figure 19 (online color at: www.lpr-journal.org) Illustration of the FWHM ($\delta\theta_{HM}$) and shifting ($\delta\theta_R$) of two SPR curves corresponding to slightly different analyte refractive index (δn_a). The prism refractive index is 1.732, wavelength 633 nm, the metal layer is silver with 47 nm thickness and the sensing layer is water with 1.33 RI.

the dielectric constants of both the metal and the analyte, the plasmon wavevector will include an imaginary part that affects mainly the width of the dip, while the real part determines the position and the shift in the resonant angle. Increasing the wavelength reduces the angular shift as well as the dip width. Since the influence of increasing the wavelength on the curve width is larger than its influence on the resonance shift, the intrinsic sensitivity was found to be larger in the IR region [78].

Golosovsky et al. [79] defined the sensitivity as the change in the reflectivity per change in the analyte refractive index: $(\partial R/\partial n_a)$. Considering the intensity mode, maximum sensitivity is achieved at some angle that corresponds to the steepest slope of the SPR curve, where the reflectivity sharply drops from unity to almost zero (see Fig. 20). However, angular sensitivity evidently decreases in the mid-IR and IR regions relative to the visible range. The advantages of operating at larger wavelengths according to Golosovsky [79] and Lirtsman et al. [80] are: (1) *penetration depth*, of the surface plasmon in the visible range is very short. This is beneficial for studying very thin layers, but detrimental for studying cells and cell cultures. The surface plasmon in the IR penetrates much deeper in the analyte and is more appropriate for studying cells, see Eq. (8). (2) *Spectroscopy*, since many biomolecules have specific absorption bands in the IR range, performing multiwavelength SPR measurements allows these biomolecules to be identified selectively. (3) *Long-range propagation*, as can be seen in Eq. (9), the propagation distance of the SP waves is determined by the ratio $\mathrm{lrp} = \left(\lambda \cdot \varepsilon_{mr}^2/\varepsilon_{mi}\right)$. The propagation length extremely increases in the IR range due to the large contrast between the square (ε_{mr}^2) and the imaginary

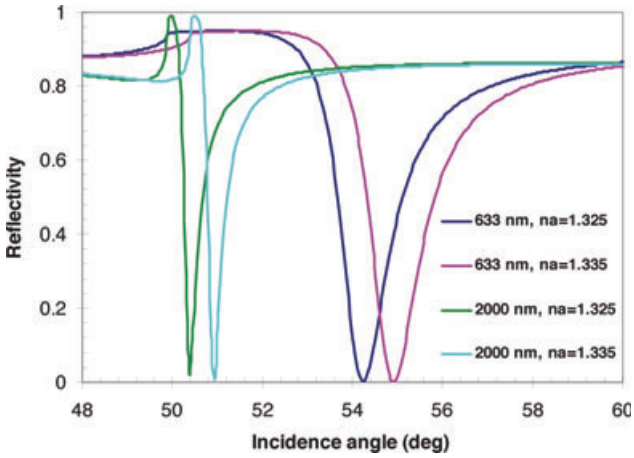

Figure 20 (online color at: www.lpr-journal.org) Reflectivity of SPR sensor in the visible versus the IR range. The reflectivity was calculated at 633 nm and 2000 nm wavelength for two values of the analyte refractive index (1.325, 1.335). The silver layer thickness was optimized to obtain perfect resonance (47 nm at 633 nm wavelength and 25 nm at 2000 nm wavelength), the prism refractive index is 1.732.

part of the metal dielectric constant (ε_{mi}), e. g. the ratio lrp equals 0.154 mm at 633 nm wavelength, and 2.88 mm at 2 μm wavelength. Although SPR sensors in the IR region have the advantages mentioned above, their angular sensitivity is still smaller than their counterpart in the visible range (if the analyte is not dispersive), hence choosing the information parameter is a critical key when evaluating the sensitivity of the system. However, if the dispersion of the analyte was taken into account, one can exploit the absorption of the sensed media at long wavelengths to enhance sensitivity. Herminjard and coworkers [81] in an experimental study reported on significant enhancement in the SPR sensor sensitivity in the mid-IR region (about five times greater than in the visible) when they detected CO_2. They attributed this enhancement to the absorption of CO_2 at 4.4 μm, which was the operation wavelength in their experiments. While the whole previous discussion in this section was on angular sensitivity, one can see in Fig. 10b that the spectral sensitivity has an opposite behavior from the angular sensitivity. Because the spectral sensitivity mainly determined by the real part of the metal dielectric constant and the metal dispersion, it increases when increasing wavelength, see Eq. (6). Moreover, using a prism with strong normal dispersion $(\frac{dn_p}{d\lambda} < 0)$ may cause an additional contribution to the sensitivity enhancement in the IR range. Patskovsky et al. [82, 83] used silicon as a prism to modify the dispersion relation of the incident light from the ambient in order to improve the sensor performance and miniaturize the structure dimensions.

3.7. Phase-sensitive SPR sensors

Recalling the phase sensitivity as was defined in Sect. 2.1; it follows from Fresnel formulas that reflection of light from a metal surface is accompanied by a change $\Delta\varphi$ in the phase

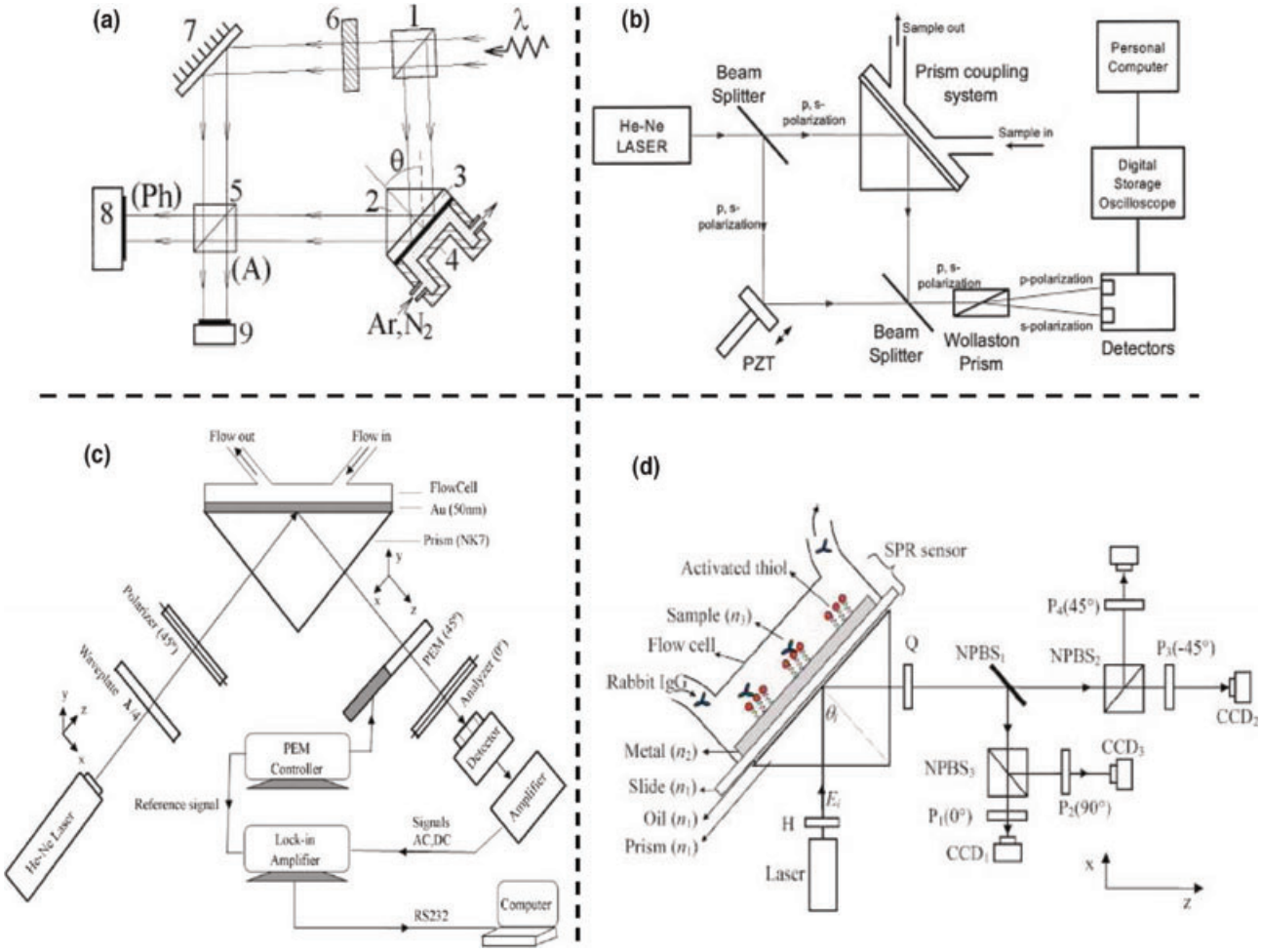

Figure 21 (online color at: www.lpr-journal.org) (a) Scheme of SPR interferometer. (1), (5) beam splitters; (2) prism; (3) slide with Au film; (4) gas cell; (6) absorbing filter; (7) mirror; (8) CCD-matrix; (9) wide-aperture photodiode, reproduced from [85] A. V. Kabashin 1998 (b) Experimental setup for measurement of differential SPR phase shift indicating s and p polarizations on the figure, reproduced from [86] S. Y. Wu (c) Schematic of surface plasmon enhanced ellipsometry (SPEE) biosensor scheme, the incidence angle of the sensing beam is 72.3 degrees to achieve maximum SPR coupling efficiency. The Quarterwave-plate and the polarizer in the input are to obtain 45 linearly polarized beam, photoelastic modulator PEM oriented at 45 degrees from the x-axis modulates the polarization state, analyzer with its orientation at 0 degrees from the x-axis, silicon detector, Reproduced from [93] W. Yuana (d) (Color online) Kretschmann's configuration for the SPR and polarization interferometer (PI) optical setup. The $+z$-axis is chosen to be along the direction of light propagation. The PI consists of a quarter-wave-plate Q, three nonpolarizing beam splitters $NPBS_{1-3}$, four polarizers P_{1-4}, (their transmittance axes are at 0, 90, -45, and 45 degrees with respect to the x-axis, respectively), and four charge-coupled devices CCD_{1-4}. The light is divided into four optical paths in the PI. Reproduced from [97] Ju-Yi Lee.

of the light beam. In the case of interaction of an elliptically polarized beam with SPR sensor in the Kretschmann configuration, the p-polarized component experiences significant modification in its intensity and phase, while the s-polarized component remains almost without a change (see Fig. 4). Since the shift in the p-polarized phase due to SPR is extremely sensitive to the analyte RI, one can measure this phase shift to detect biomolecular binding events at the metal/analyte interface. Kabashin and coworkers [84, 85], in two successive studies presented a classic interferometric method for the detection of the phase shift of reflected light under SPR conditions due to refractive-index change. By measuring the phase difference between the signal that passed through SPR conditions and the reference, the authors reported that a detection limit on the order of 4×10^{-8} RIU can be achieved. In the latter method, the signal and the reference passed noncommon paths, a fact that affects the detection limit (see Fig. 21a). Since SPR affects only the p polarization, the signal due to the s polarization can be used as the reference. Consequently, the differential phase between the two polarizations allows eliminating all noncommon-path phase noise sources, while keeping the phase change caused by the SPR effect. Wu et al. [86] used the Mach–Zehnder interferometer with a Wollaston prism to interrogate simultaneously the p and s polarizations in which a detection limit of 5.5×10^{-8} RIU was obtained (see Fig. 21b). Several attempts based on the common-path approach were made, such as quadrature interferometry [87]

and the use of multipass interferometry in the Michelson and Fabry–Perot configurations which gave the possibility of enhancing the phase shift and reducing the detection limit by a factor of two [88]. One can see that the field of phase-sensitive SPR sensors was extensively investigated in the last decade due to the fact that phase interrogation yields smaller LOD as compared to other interrogations. The origin of the last insight is the steep and abrupt change caused to the phase under SPR effect while the intensity dependence is much more moderate. In addition, in some of the techniques where the phase difference between the s and p polarized waves is measured, the noise level can be made very small such as when ellipsometry is used because it is a self-referenced technique. Ran and Lipson [89] did not agree with the superiority of the phase mode and claimed that both intensity mode and phase mode have a comparable detection limit. The authors claimed that there is no way to measure phase shift unless by interferometry means that are by the end intensity measurements. Although it is true that standard interferometry might not reveal better LOD, depending on how noisy the system is, we think that common-path interferometry as well as ellipsometry and polarimetry are superior in phase-difference measurements. For example it is well known from polarimetry and ellipsometry that it is possible to measure phase retardation $\Delta = \varphi_{TM} - \varphi_{TE}$ with a precision better than 0.001°. Hence, using SPR retardation sensitivity of 10^5 deg/RIU (see Table 1) one can arrive to a LOD of 10^{-8} RIU.

Following these considerations, and to refute the claims in [89] the noise sources in SPR sensors were analyzed by Kabashin et al. [90] who showed experimentally that using polarimetric measurement with photoeleastic modulator (PEM), an LOD of 4×10^{-8} RIU can be obtained. They used a gold substrate purchased from Biacore that when used with a Biacore commercial system gives two orders of magnitude higher LOD. This indicates the superiority of the phase mode when measured using modulated polarimetry. As mentioned before, the LOD that is determined by the sensitivity and the SNR of the system depends on many elements of the system itself as well as on the concept upon which the measurement is based. Using polarimetry, ellipsometry or common-path interferometry the LOD can be lowered because high SNR is achievable. Table 1 summarizes the sensitivities in phase-sensitive SPR versus other techniques of SPR sensing. Calibrating the incidence angle to the appropriate resonance angle is a very important

Table 1 Typical sensitivities and LOD for different methods and sensitivity definitions.

Information parameter		Enhancement mechanism	Sensitivity	Typical system noise	λ nm	System type	LOD (RIU)	Ref.
Measured magnitude	Sensitivity definition							
Resonance angle	$\frac{d\theta_{RES}}{dn_a}$ °/RIU	Gold on SF11	66	10^{-4}	670	K. C.	1.5×10^{-6}	21
		Synthesized quartz prism 1.456	204	10^{-4}	670	K. C.	5×10^{-7}	51
		Adding top dielectric layer	160	10^{-4}	670	K. C.	6×10^{-7}	40
		Periodic metallic structure	650	10^{-4}	850	K. C.	1.5×10^{-7}	64
Resonance wavelength	$\frac{d\lambda_{RES}}{dn_a}$ nm/RIU	Gold on SF11	2750	0.02	700	K. C.	7×10^{-6}	21
		Long-range SPR	30 000	0.0074	700	K. C.	2.5×10^{-6}	74
		Long-range SPR optimized	570 000	0.0014	830	K. C.	2.5×10^{-8}	76
Reflected intensity	$\frac{dR}{dn_a}$ %/RIU	Gold on BK7	3900	0.2%	630	K. C.	5×10^{-5}	9
		Gold on BK7	15 000	0.2%	850	K. C.	1×10^{-5}	9
		Grating-based SPR	4400	0.2%	850	Grating	5×10^{-5}	
TM-Phase change	$\frac{d\varphi_{TM}}{dn_a}$ rad/RIU	SPR interferometer	1.5×10^5	$2\pi 10^{-3}$	633	SPR interferometer with K. C.	4×10^{-8}	84
TM-TE Retardation	$\frac{d\varphi_{TM-TE}}{dn_a}$ °/RIU	Mach–Zehnder interferometer	1.8×10^5	0.01	633	Mach–Zehnder interferometer	5.5×10^{-8}	86
		Polarimetry	1.2×10^5	0.005	633	PEM- based polarimeter	4×10^{-8}	90
		Ellipsometry	666	4×10^{-4}	633	PEM-based ellipsometer	6×10^{-7}	93

K. C. – Kretschmann configuration

condition to obtain an enhanced detection limit in phase-sensitive SPR sensors [91, 92]. So far, all the methods that were presented are based on an interferometric approach to detect phase shift. Other methods based on modulated ellipsometry scheme using PEM [93] (see Fig. 21c), polarimetry-based methodologies [94], and other applicative sensing systems [95] were investigated and applied. Furthermore, the phase mode was used in two-dimensional biosensor arrays based on SPR imaging [96, 97] and other advanced techniques such as fiber-based SPR sensors [98] which were examined theoretically for nanohole-array-based SPR sensors [99]. Profiting from a much superior LOD, some promising designs of phase-sensitive SPR polarimetry are now successfully commercialized [100].

It is clear that most of the techniques of phase-sensitive SPR constitute a successive effort to improve the LOD of SPR sensors. The fact that LOD represents the absolute ability of the sensor in detecting tiny concentrations of biomolecules makes it a universal characteristic in evaluating SPR sensors performances. In the work of Piliarik and Homola [101], there was a decisive attempt to determine an ultimate resolution of an SPR sensor. Although the attempt of the authors was to perform an intensive analysis of the noise sources in SPR sensors, there were some assumptions in their discussion that may break this ultimate resolution value such as: ignoring the high resolution of phase-sensitive SPR sensors, the Lorentzian approximation of the reflectivity profile, and the use of gold as the preferred transducer layer. However, the expression that was derived in [101] might help improve the LOD available by improving the metal layer features, the coupling strength between the SP and the incident light, and reducing the detector noise.

3.8. SPR imaging techniques for sensing

SPR Imaging (SPRI) enables spatially resolved, surface-sensitive, label-free, real-time analysis of surface–biomolecule interactions and is compatible with a microarray format. Typically, the collimated reflected light beam from an SPR experiment is detected by a camera, detector array or viewed through a microscope, enabling spatial measurements of changes in the thickness or refractive index at a particular surface. If an SPR image is grabbed at a fixed incident angle (collimated beam), the reflectance of any region within the sensor area is a function of the refractive index of the sample immediately next to the sensor surface. While if the beam is diverging or converging, any index variations on the surface will result in different resonance locations (see Fig. 22). This feature of SPRI permits the label-free, rapid, and parallel analysis of the adsorption of a particular biomolecule to an array of sample spots under identical environmental conditions. SPRI can also reveal an improvement in the LOD since the image contains a large number of data points. Assuming a uniform analyte for example, with the noncollimated-beam approach, the SPR will result in a dark straight line in a bright background. Each pixel in this line defines one measurement point of the SPR location. Hence, with SPRI one gets an improved precision, which in turn improves the LOD as it was recently pointed out by Karabchevsky et al. [102].

SPRI could be performed using the whole variety of SPR detection methods and approaches that were mentioned before. By SPR intensity imaging technique, one measures the reflectivity changes caused by the refractive-index variations on the surface. On the other hand, in SPR phase imaging, the phase shift is measured as a function of the analyte refractive-index change.

SPR imaging techniques have been used to study the sequence-specific adsorption of response regulator proteins to DNA [103, 104], bioaffinity interactions in peptide arrays [105], proteins [106], and carbohydrate–protein interactions [107]. A very important feature in SPR imaging is the spatial resolution of the image that is determined by the propagation length of the SP at the interface between the metal and the analyte, which is dependent on the dielectric constant of the metal film, the refractive index of the analyte, and the frequency of the incident light (see Eq. (9)). Under optimized conditions, a resolution of less than 2 μm can be achieved [108]. Novel approaches towards the development of high-resolution microarrays are critical for high-throughput screening. Jung et al. [109] demonstrated a simple method to fabricate SPR imaging microarrays using

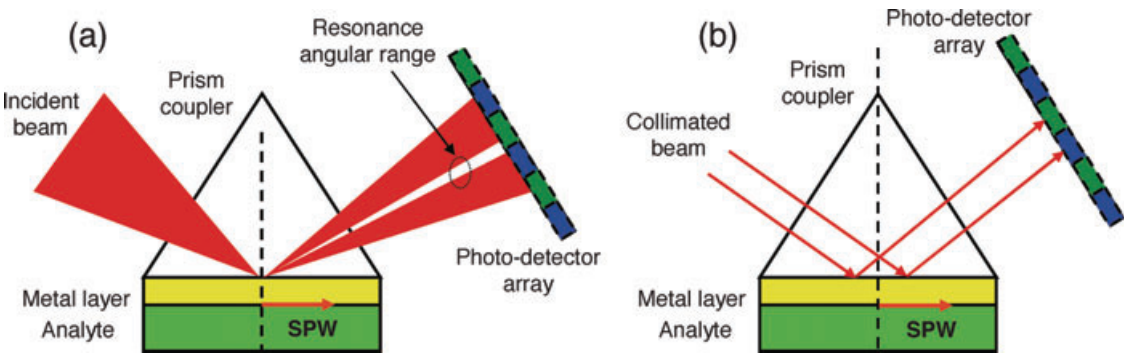

Figure 22 (online color at: www.lpr-journal.org) an illustration for two different SPR imaging schemes (a) when illuminating with a converging beam, the intensity per pixel is also angle dependent (b) fixed incident beam configuration (collimated beam), the intensity at each pixel of the output image depends on the reflectance, which in turn determined by the refractive index of the analyte.

polymer micropatterns. The use of a micrometer-scale polymeric optical screen (microPOS) passivates the region deposited with polymer by removing SPR signals completely or by saturating the SPR signal far beyond the detection range in SPR imaging [109]. Recently, the SPR reflectance imaging technique was proposed as a label-free visualization tool to characterize near-field fluidic transport properties [110]. The key idea is that the SPR reflectance intensity varies with the near-field refractive index of the test fluid, which in turn depends on the micro/nanofluidic scalar properties, such as concentrations, temperatures, and phases. A combined electrochemical and SPR measurements can be performed on a multielectrode sample such that a large number of electrochemical potentials and associated surface phenomena can be interrogated in a single experiment [111]. Although most of these research works are based on the SPR intensity imaging technique, phase-sensitive SPR imaging was also presented in the works of Wong et al. [96] and Lee et al. [97]. Exploiting the improved LOD that characterizes the phase-sensitive SPR method and the advancement in fabricating multielement arrays make this system promising for biosensing. Experiments are now on-going to populate the high-density microarrays with a variety of protein species for label-free diagnostic applications.

3.9. Recent developments

Due to the intensive advances in extraordinary optical materials, many researchers show interest in the excitation of surface plasmons from engineered nanomaterials, and consequently investigating the effect of such materials on the sensitivity of biosensors that are based on these structures. Ishimaru et al. [112] presented the use of metamaterials for plasmon resonance sensors at microwave frequencies. The work deals with a surface plasmon sensor making use of an isotropic and homogeneous metamaterials. However, there are some practical issues, including the questions of how to construct such metamaterials, and what are the effects of anisotropic characteristics. Since most metamaterials are known to be highly dispersive and lossy, the sensitivities need to be carefully studied. It is also important to investigate how to construct practical broadband, low-loss metamaterials. The use of porous materials in SPR biosensors has also been under the investigation by several groups. Columnar thin films (CTFs), which can be considered as porous materials were investigated first by Yang et al. [113]. They used a prism coupling of SPPs in the Otto geometry at 3.391 μm to determine the surface optical anisotropy of several obliquely deposited nickel films. Yang et al.. measured SPR response from these CTFs of nickel and estimated by the Bruggeman effective-medium theory the optical properties and the geometrical factors of the metallic films. Nanoporous gold films in the context of SPR were also investigated by Maaroof et al. [114]. In the pioneering study of Shalabney et al. [115], the authors demonstrated that thin films of porous metals can be used as biosensors. They showed that using metallic CTFs facilitates the development of sensors with high sensitivity. For Ag and Au CTFs, the SPR dip sensitivity increases by about a factor of 2 with 30% porosity as compared to nonporous films. As shown in Fig. 23, the metallic CTF was divided into two porous layers with different thicknesses and the porosity was varied to obtain optimal fit with the experiments results. The authors demonstrated theoretically that the sensitivity of a CTF-based SPR sensor is higher than the conventional SPR sensor, and furthermore the sensitivity can be tuned by varying the porosity of the CTF. As the porosity increases, the SPR dip widens and becomes asymmetric because of increasing scattering losses in the CTF that are due to the nonhomogeneous distribution of matter therein. As the porosity increases beyond 0.75, the SPR dip almost disappears, with a vestigial peak near the onset to the TIR regime, which can be also used as a *peak sensor*.

The appearance of a peak at the onset of the TIR regime when the SPR broadens can also be seen when the broadening is due to absorption loss rather than scattering loss inside a thin metal film. Al and Cr, for example, have bulk refractive indexes with high imaginary parts at wavelengths in the visible region; therefore, absorption loss is strong in these metals and the peak can be seen even with dense films. The appearance of the peak in conventional SPR sensor with closed metallic film indicates that a peak sensor can be produced also due to absorption losses (see Fig. 24).

4. Sensitivity enhancement methods in localized SPR sensors

The most common method for LSPR sensing is the wavelength-shift measurement, in which the change in the maximum (or minimum) of the LSPR extinction curve is monitored as a function of changes in the local dielectric environment caused by analyte adsorption. This relationship is described in Eq. (22), and has been demonstrated for a number of systems in which either the bulk-solvent refractive index or the length of a molecular adsorbate (i. e. a linear alkane chain) is changed. Coupling two plasmonic nanoparticles also leads to a shift in λ_{res}. In this equation, the sensitivity to the bulk refractive index S_λ plays an important role in determining the total response of the LSPR. This sensitivity depends on various factors such as size and shape of the nanoparticles; in the following section we discuss the effect of the particles shape and its design on the sensing process.

4.1. Metallic nanostructures design and evanescent-field enhancement methods

Apparently, the resonance position is not dependent on the particle size, as can be seen from Eqs. (17) and (19) for a sphere and only variations in the intensity of the SPR absorption with particle size are observed. However, experimentally the SPR bandwidth as well as band position is observed to depend on the nanoparticle size. In the modification to the Mie theory, Drude and Sommerfeld considered

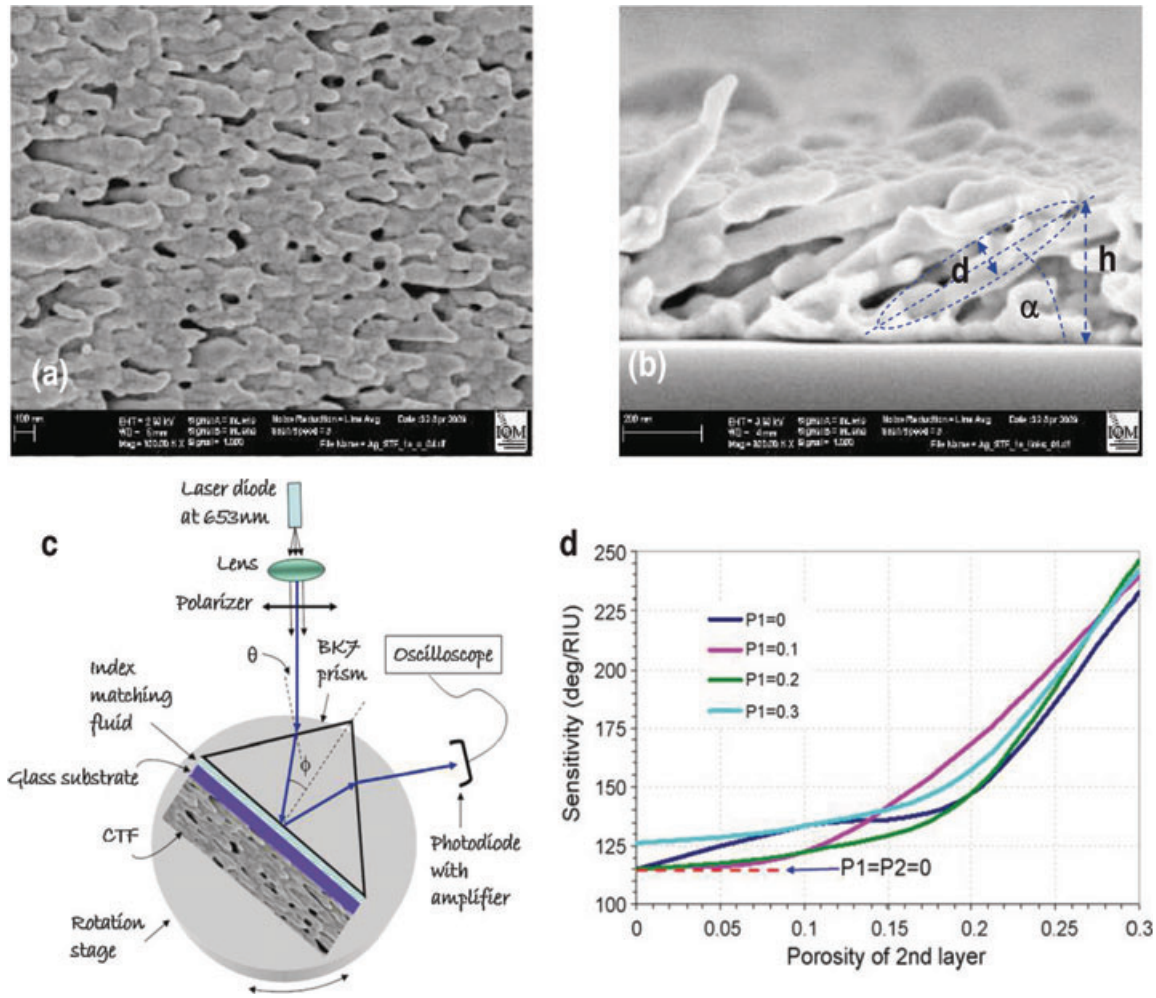

Figure 23 (online color at: www.lpr-journal.org) (a) silver columnar thin films (top view) (b) silver columnar thin film (cross section) (c) schematic of the Kretschmann configuration using CTF as the metal film (d) simulation results to demonstrate the sensitivity enhancement as the porosity deceases. Calculated sensitivity when the porosity of the first layer (thinner layer) is kept fixed as indicated in the legend while the porosity of the thicker layer is varied from 0 to 0.3. (Reproduced from [115], A. Shalabney et al. Parts (c) and (d) were taken from Figs. 2 and 10, respectively, in the original article).

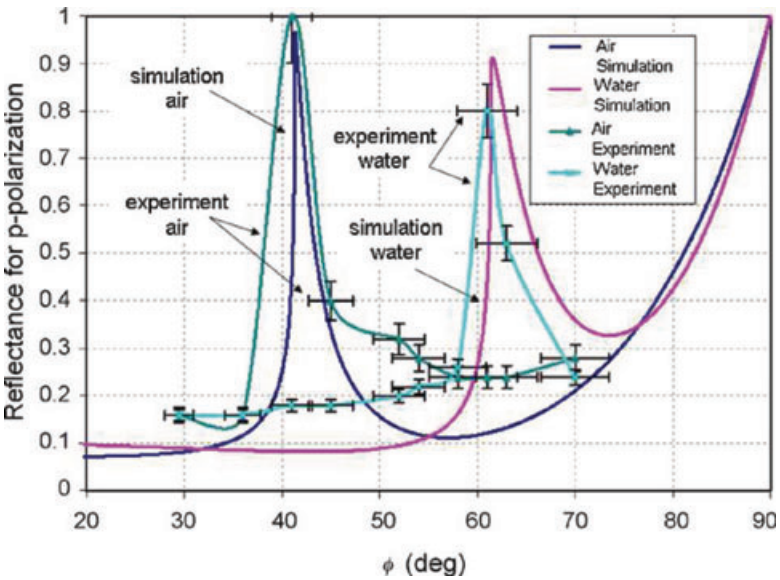

Figure 24 (online color at: www.lpr-journal.org) Measured/simulated data for p-polarization reflectance R versus the angle φ when the dense/nonporous ($p = 0$) metal film is 8 nm thick and made of Cr. The curves exhibit a broad dip and a sharp and symmetric peak due to the absorption in bulk Cr. The analyte sensed is either air or water (refractive index = 1.33). The graph was reproduced from Fig. 4 of reference [115] by A. Shalabney et al.

that the relative permittivity of the nanoparticle depends on the size $\varepsilon(\omega, R)$ in lieu of $\varepsilon(\omega)$. The real and the imaginary parts of the modified relative permittivity are given by [116, 117]:

$$\varepsilon'(\omega) = \varepsilon_{\mathrm{ib}} - \frac{\omega_{\mathrm{p}}^2}{\omega^2 + \omega_{\mathrm{d}}^2} \tag{27}$$

and

$$\varepsilon''(\omega) = \frac{\omega_{\mathrm{p}}^2 \cdot \omega_{\mathrm{d}}}{\omega\left(\omega^2 + \omega_{\mathrm{d}}^2\right)}, \tag{28}$$

where $\varepsilon_{\mathrm{ib}}$ is the high-frequency limit of $\varepsilon(\omega)$, arising from response of the core electrons (electrons in completely filled bands); ω_{d} is the relaxation or damping frequency that represents collisions of electrons with the lattice (phonons) and defects; and ω_{p} is the bulk plasmon frequency given by:

$$\omega_{\mathrm{p}}^2 = \frac{4\pi n e^2}{m}, \tag{29}$$

where n is the electron concentration in metal, e is the electronic charge and m is the effective mass of the electron. The dependence of the relative permittivity on the particle radius R was introduced by assuming that the particle size is smaller than the mean free path of conduction electrons. The damping frequency ω_{d} is related to the mean free path of the conduction electrons in bulk metal R_{bulk} and Fermi velocity of electrons v_{f} by:

$$\omega_{\mathrm{d}} = \frac{v_{\mathrm{f}}}{R_{\mathrm{bulk}}}, \tag{30}$$

when R becomes smaller than the mean free path, surface scattering is dominant. This surface scattering results in the peak broadening and induces a $1/R$ dependence of the SPR bandwidth. In this case, the effective mean free path R_{eff} becomes size dependent according to:

$$\frac{1}{R_{\mathrm{eff}}} = \frac{1}{R} + \frac{1}{R_{\mathrm{bulk}}}. \tag{31}$$

In Sect. 2.2 we referred to a correction function that usually added to the permittivity of the metal and above we demonstrated in detail how the LSPR resonance could be dependent on the particles size due to this correction. One can see from Eqs. (18)–(22) that the metal particle shape dictates the spectral signature of its plasmon resonance. The ability to change this parameter and study the effect on LSPR response is a very important experimental challenge. The development of increasingly sophisticated lithographic and chemical methods now allows the routine production of a wide variety of complex NPs and their assemblies [118]. For example, the spectrum of silver nanoparticles can be tuned from 380 nm to at least 6 µm by varying their size and shape, with increasing aspect ratio and sizes producing nanoparticles with redshifted LSPR spectra [119]. Recently, an ideal class of colloidal Ag nanoparticles with highly uniform morphologies and narrow size distributions were synthesized [120]. For particle diameters in the range $d \approx 2 - 20$ nm, an exceptional behavior was observed: as the size decreases below $d \approx 20\,nm$ it blue shifts but then turns over near $d \approx 12$ nm and strongly redshifts. In contrast to the size of the nanoparticle, a change in the shape produces larger shifts and modification in the LSPR band. In a theoretical study of the LSPR bulk sensitivity behavior that was presented by Miller and Lazarides [121], the authors used the discrete dipole approximation (DDA) to calculate the electrodynamics' response of an arbitrary nanoparticle to a plane-wave excitation. By investigating the correlation between the extinction spectra of the particle and the aspect ratio, material properties, resonance wavelength; interesting results were obtained. The resonance wavelength increases with an increasing the aspect ratio [122, 123], and the sensitivity had a positive correlation with the resonance wavelength. The calculations were fitted with analytical approximations that demonstrated that bulk sensitivity basically depended on the resonance wavelength, particle material dispersion, and the medium refractive index. Fig. 25 demonstrates the correlation between resonance wavelengths for cylinders, discs, and hallow nanoshells made from gold with various aspect ratios. Fig. 25d shows the linear dependence of the bulk sensitivity on the resonance wavelength.

Haes and coworkers [124] reported on the use of Ag nanotriangles synthesized using nanosphere lithography (NSL) as an LSPR biosensor that monitors the interaction between a biotinylated surface and free streptavidin or anti-biotin in solution. While Fu et al. [125] reported on an LSPR sensor for detection of salmonella bacteria and found that due to the small contact area between the nanoparticle and the bacteria and the short-range interaction of the local electric field, the plasmon peak shift induced by such a system is about 2–4 nm, regardless of the concentration of the bacteria. A multireflection-based device was used by Hamamoto et al. [126] to study the LSPR response of gold nanoparticles on glass substrate to changes in sucrose concentration as an analyte. The authors found that multireflections of the incident beam at the glass/nanoparticles interface improve the sensitivity of the detection process.

An alternative sensing modality that use gold nanohole arrays and composite crystalline–metal nanostructures has been shown to exhibit even greater sensitivity in response to refractive-index changes. Hicks and coworkers [127] developed a plasmonic structure termed "film over nanowell" that exhibited plasmon peaks with a FWHM as narrow as 35 nm, and improved refractive index sensitivity $S_\lambda = 538$ nm/RIU (see Eq. (22)) with an overall figure of merit (FOM), S_λ/FWHM of about 14.5, surpassing the typical FOM for nanoprisms arrays of about 3. The use of metallic nanohole arrays as biosensors will be extensively discussed in Sect. 4.3 within the framework of extraordinary optical transmission (EOT) sensors. Other novel nanostructures were widely investigated and presented in the last few years as a high-sensitivity LSPR devices such as Au nanoparticles and multiwalled carbon nanotubes with sensitivity of about 5.6 times greater than Au NPs on a glass chip [128], aligned gold nanotube arrays [129], Au nanorods protected with mPEG-SH molecules as LSPR-based sensors of molecular biothiols [130]. Metamaterials-based sensors composed

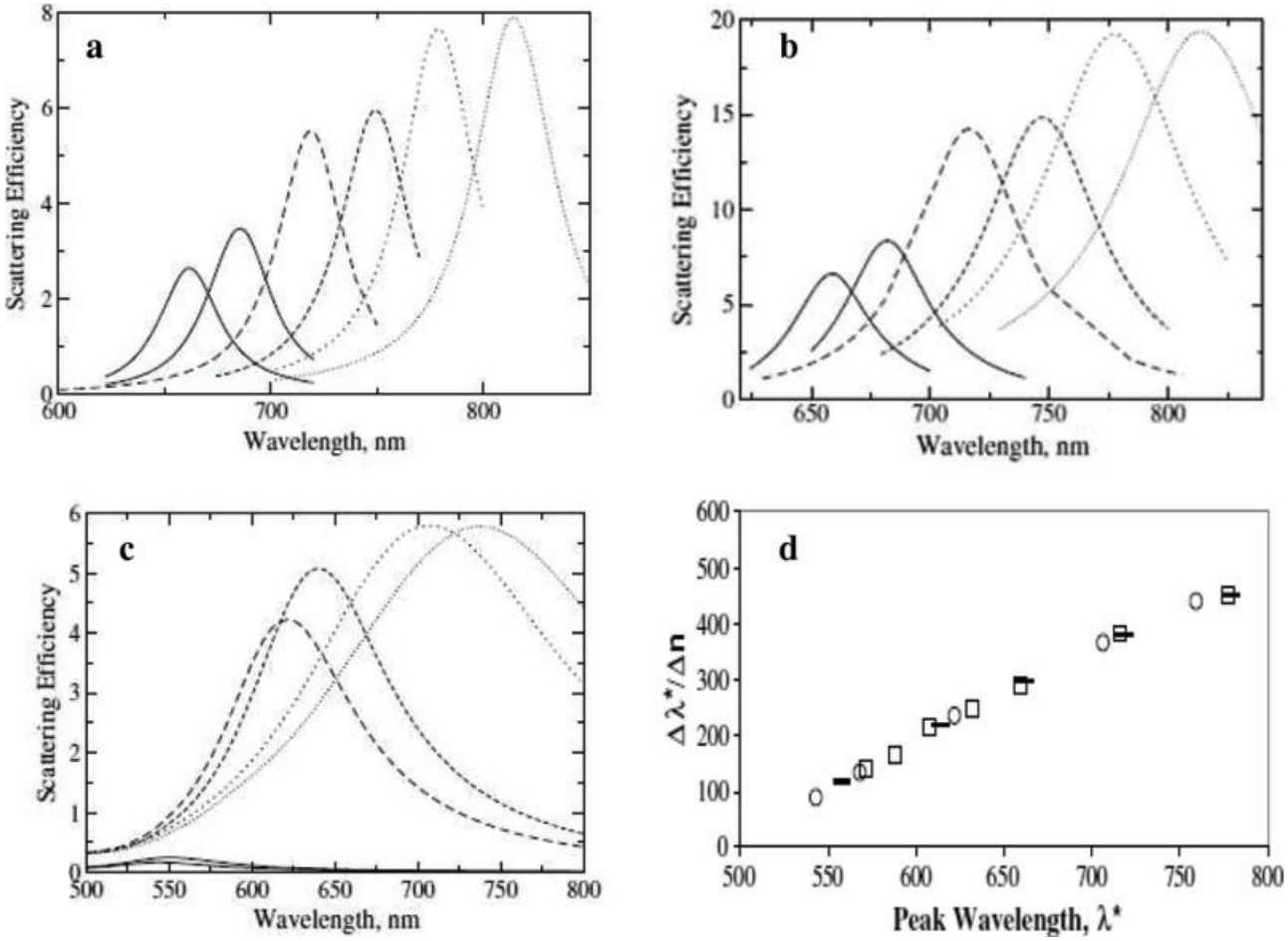

Figure 25 (a) Scattering spectra of gold nanocylinders in media of refractive index 1.33 (thick lines) and 1.41 (thin lines). Cylinders are 20 nm in diameter and 40 (solid lines), 50 (dashed lines) or 60 (dotted lines) nm in length (b) Scattering spectra of gold nanodiscs in media of refractive index 1.33 (thick lines) and 1.41 (thin lines). Discs are 12 nm in height and 60 (solid lines), 80 (dashed lines) or 100 (dotted lines) nm in diameter (c) Scattering plasmon bands of three hollow gold nanoshells in media of refractive index 1.33 (thick lines) and $n = 1.41$ (thin lines). The particles have core radii of 5 (solid lines), 30 (dashed lines) and 50 nm (dotted lines) and 15-nm thick gold shells. Note that sensitivities are calculated under the assumption that the refractive index of the interior, n_{core}, varies identically with that of the external medium (d) Sensitivity of scattering LSP peak wavelength to bulk refractive index as a function of peak wavelength. Sensitivities of gold nanodiscs (open squares), nanocylinders (dashes) and hollow nanoshells (open circles) of size parameters less than 0.77 are shown. (Reproduced from [121], Molly M. Miller et al. Parts (a), (b), (c), and (d) were taken from Figs. 1, 3, 5, and 7, respectively, in the original article).

of nanorods with spectral sensitivity of 30 000 nm/RIU and a large probe depth up to 500 nm [131], phase-sensitive SPR biosensors with the use of gold nanorods as powerful amplification labels [132]. The high sensitivity in using metamaterials-based nanorods [131] basically originates from two reasons, first the overlap between the localized electric field guided inside the rod slab, and secondly because the modification of the metamaterials dielectric constant when changing the analyte RI that makes the dispersion relation steeper. Table 2 summarizes some of the available nanostructures and their sensitivities. In addition to describing methods to improve the sensitivity of nanoparticles, Anker et al. [133] surveyed, in their review article, several important techniques to enhance LSPR shift. Advances in LSPR instrumentation and analysis have allowed the detection of LSPR spectral shifts with a noise level of less than 5×10^{-4} nm and less than 5×10^{-6} extinction units [134]. Most LSPR spectroscopy has been performed with large ensembles of nanoparticles. However, each nanoparticle in the ensemble could potentially serve as an independent sensor. Single-nanoparticle sensors offer improved absolute detection limits and also enable higher spatial resolution in multiplexed assays together with better SNR resolution, providing them with promising applications for measurements in solutions, or inside cells and tissues where fixed arrays are unable to penetrate [135]. Furthermore Anker et al. [133] explored the interaction between the molecular resonance of a chromophore and the plasmon resonance of a nanoparticle. When chromophores adsorb onto silver nanoparticles, the resulting LSPR shift depends strongly on the spectral overlap between the molecular absorbance and the LSPR. A drastic change in the LSPR shift was observed

Table 2 Sensitivity of nanostructures with different geometries and shapes.

Geometry	Resonance wavelength (nm)	Width (nm)	Height (nm)	Metal type	Sensitivity (nm/RIU)	Ref.
Hollow Nanoshells	500–760	Thick 15 nm	Radii 5–60	Au	80–420	121
Nanorice	1200–1700	13 nm thick	340 nm and 54 nm radii	Au/Hematite	800	149
Nanorods	1280	50	700	Au	32000	131
Discs	550–850	20–120	12	Au	100–500	121
Cylinders	662–778	40–20	20–60	Au	100–420	121
Triangular	561	100	51	Ag	NA	147
Nanowell	750	590	50	Ag	538	127
Nanotubes	650	44	120	Au	225	129
Nanorods	750	15	60	Au	252	130
Prisms	561	100	50	Ag	191	136

NA – data not available (the sensitivity was measured in wavelength shift with the analyte concentration, and not with the change in the analyte refractive index).

when the LSPR of silver nanoparticles was tuned through the molecular resonance of MgPz at 598 nm [136, 137].

The dependence of the nanoparticle surface plasmon resonance on the interaction between proximal nanoparticles has also been studied in detail [138, 139]. When noble metal nanoparticles come in close proximity, the plasmon resonance oscillations on the individual nanoparticles are coupled. For light polarized parallel to the interparticle axis, this coupling causes a redshift in the plasmon resonance, which increases with decreasing interparticle separation [140]. Jain and El-Sayed [141] used a pair of gold nanospheres as a model for a coupled-particle system for investigating the effect of the separation distance between the particles on the LSPR response.

Similar to isolated nanoparticles, Fig. 26 shows that for a coupled nanoparticles pairs there is a redshift in the plasmon resonance of the two-particle system as the medium refractive index is increased. The rate at which the plasmon resonance redshifts in response to a given refractive-index change increases rapidly as the interparticle separation in the nanosphere pair is decreased. The sensitivity was found to be very strongly dependent on the separation between the coupled particles, as can be seen from Fig. 27 where D is the particle diameter, and d is the interparticle surface-to-surface separation [142].

A wide variety of nanoparticle shapes were proposed as LSPR sensors such as, rings [143], dots [144], stars [145], nanobottles [146], nanoprisms [147], nanocubes [148], nanorice [149] and many other shapes. A very important aspect in shape modification is the field enhancement caused by structure design. Similar to SPR (Sect. 2.3), the field enhancement in the vicinity of the nanoparticles plays a very

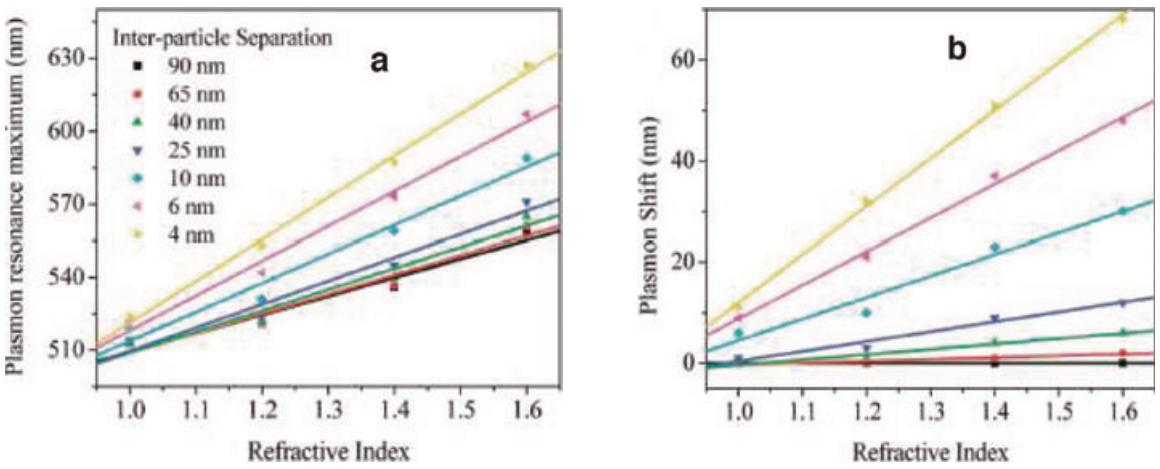

Figure 26 (online color at: www.lpr-journal.org) (a) Plasmon resonance wavelength maximum and (b) coupling-induced resonance wavelength redshift for a pair of 40 nm gold nanospheres as a function of the medium refractive index for different interparticle separations. The plasmon resonances were simulated for light polarized along the interparticle axis. The solid lines are straight-line fits (Reproduced from [142] by Prashant K. Jain et al. Both parts (a) and (b) were taken from Fig. 1 in the original article).

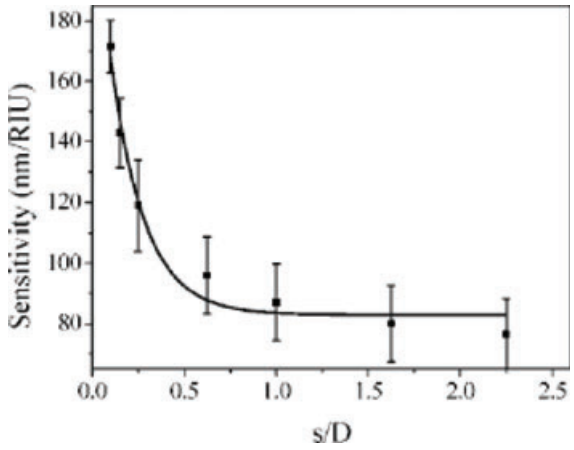

Figure 27 Plasmon resonance sensitivity $(\Delta\lambda_{SP}/\Delta n_m)$ in the gold nanosphere pair plotted as a function of the interparticle separation in units of the particle diameter (s/D). The sensitivity increases nearly exponentially with decreasing (s/D) as seen from the fit (solid line) to the single-exponential decay $(y = y_0 + a \cdot \exp(-x/\tau)$ where $\tau = 0.18 \pm 0.04$. The error bars represent the error in the straight line fits in Fig. 24a. (Reproduced from Fig. 2 of reference [142] by Prashant K. Jain et al.)

significant role in improving sensitivity when this structure is used as a biosensor. This phenomenon has a key application in surface-enhanced spectroscopy, such as surface-enhanced Raman scattering (SERS) and surface-enhanced fluorescence (SEF). When the nanostructure has more corners, more resonance wavelengths can be excited and more hot spots can be obtained at these resonance wavelengths. In U-shaped structures that were presented by Zhang and Zhao [150] more resonance wavelengths in the visible range were excited as compared to parallel nanorods. The electrons in the parallel nanorods structure can oscillate within the individual nanorods, while in the U-shaped structure the bottom rod builds a path to connect the two vertical nanorods, and further plasmons can be excited. As one can see from Fig. 28, for a parallel nanorod structure just two resonance wavelengths can be excited (at 0.359 μm and 0.341 μm), while in the U-shaped structure an additional three wavelengths appear (at 0.820 μm, 0.579 μm, and 0.485 μm).

When illuminating the U-shaped nanostructure with these wavelengths, a larger enhancement to the local field and more hot spots are obtained. The local field enhancement is expressed by $\gamma \equiv |E|^2 / |E_0|^2$, where E is the local electric field and E_0 is the incident field. The resonances

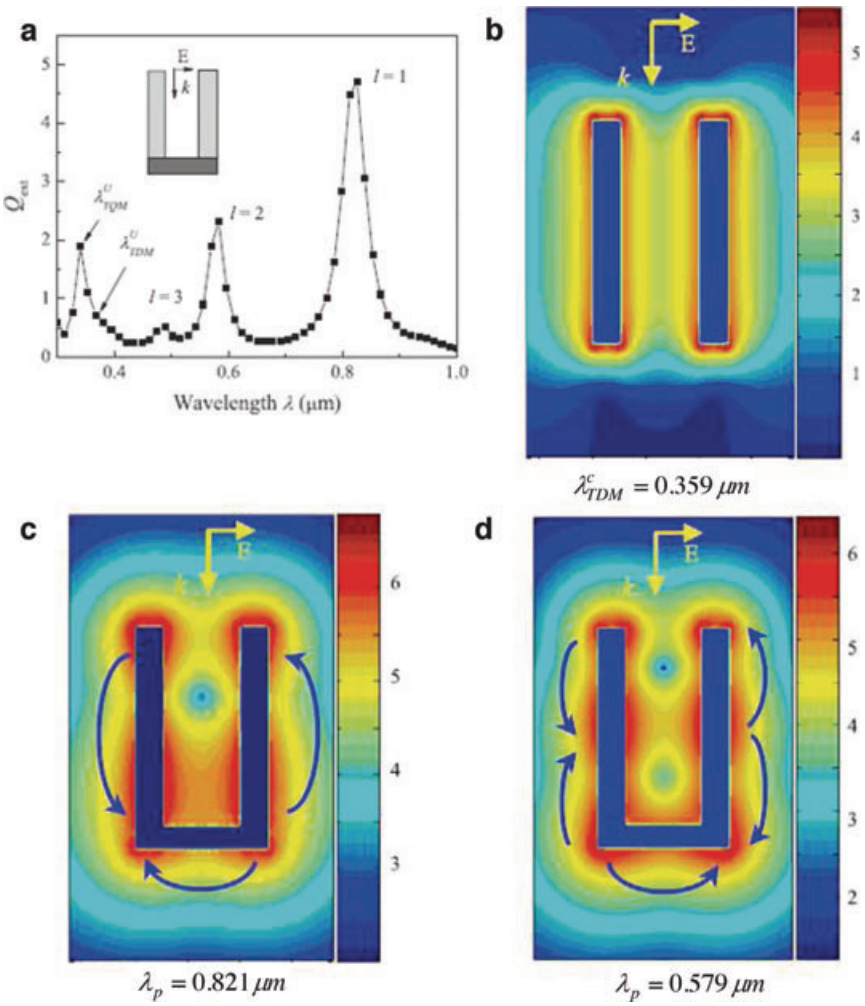

Figure 28 (online color at: www.lpr-journal.org) (a) Calculated extinction spectra of the U-shaped nanostructure (b) E-field enhancement contours $(\log_{10}\gamma)$ of the parallel-nanorod structure at wavelength $\lambda = 0.359\,\mu m$, a characteristic resonance wavelength to parallel nanorods (c) E field enhancement contours $(\log_{10}\gamma)$ of the U-shaped structure at wavelength $\lambda = 0.820\,\mu m$, a resonance wavelength that is excited in the U-shaped structure (d) E field enhancement contours $(\log_{10}\gamma)$ of the U-shaped structure at wavelength $\lambda = 0.579\,\mu m$, a resonance wavelength that is excited in the U-shaped structure. (Reproduced from [150] by Zhongyue Zhang et al. Parts (a) and (b) were taken from Figs. 4 and 3, respectively, and parts (c) and (d) were taken from Fig. 5 in the original article).

can be tuned by controlling the dimensions of the nanostructures, which makes it a very useful tool in biosensing and enhanced spectroscopy.

4.2. Surface-enhanced spectroscopies

The interaction between light and nanoparticles causes further optical signals to arise and be enhanced such as surface-enhanced raman scattering (SERS) and surface-enhanced fluorescence (SEF). SERS is a very sensitive spectroscopy that allows the detection of organic molecules adsorbed on noble-metal substrates (silver, gold, copper) at submicromolar concentration. Xu coworkers [151] and have obtained vibrational Raman Spectra from single hemoglobin molecules attached to 100-nm-sized immobilized Ag particles. Since SERS depends on the local field to the fourth power ($|E|^4$) in the vicinity of an adsorbate molecule [152, 153], one can significantly enhance the SERS intensity by enhancing the field near the scattering molecules. In the previous section we reviewed field-enhancing methods by using different shapes of nanostructures characterized by a large field enhancement factors due to excitation with the resonance wavelengths corresponding to the specific structures. Félidj et al. [154] found that by engineering the nanoparticle structure size and shape to yield resonance wavelength that is suitably located between the exciting laser and the Raman frequency, one can obtain large enhancement factors of Raman scattering signals. The effects of the nanostructures features (substrate material, nanoparticles material, nanoparticles size, nanoparticles shape, etc.) on the SERS enhancement were intensively investigated during the last few years [155–157]. In the work of Kumar and coworkers [158] it was shown that a SP, propagating along a metal surface, embedded with regularly arranged nanoparticles, undergoes surface-enhanced Raman scattering from molecules adsorbed over the particles. A significant scattered wave is detected if a relative relationship between, the particles arrangement period, Raman frequency and the surface plasmon wave is satisfied. In Fig. 29, the effects of the temperature and the substrate rotation during the deposition on SERS spectra are demonstrated. SERS has been shown recently [46] to give significant and reproducible signal using ultrasmooth metal surfaces on variety of Si based nanostructures.

The potential of SEF was rediscovered during the past decade due to the emerging developments in the optics of metallic nanostructures [159]. SEF is a very useful phe-

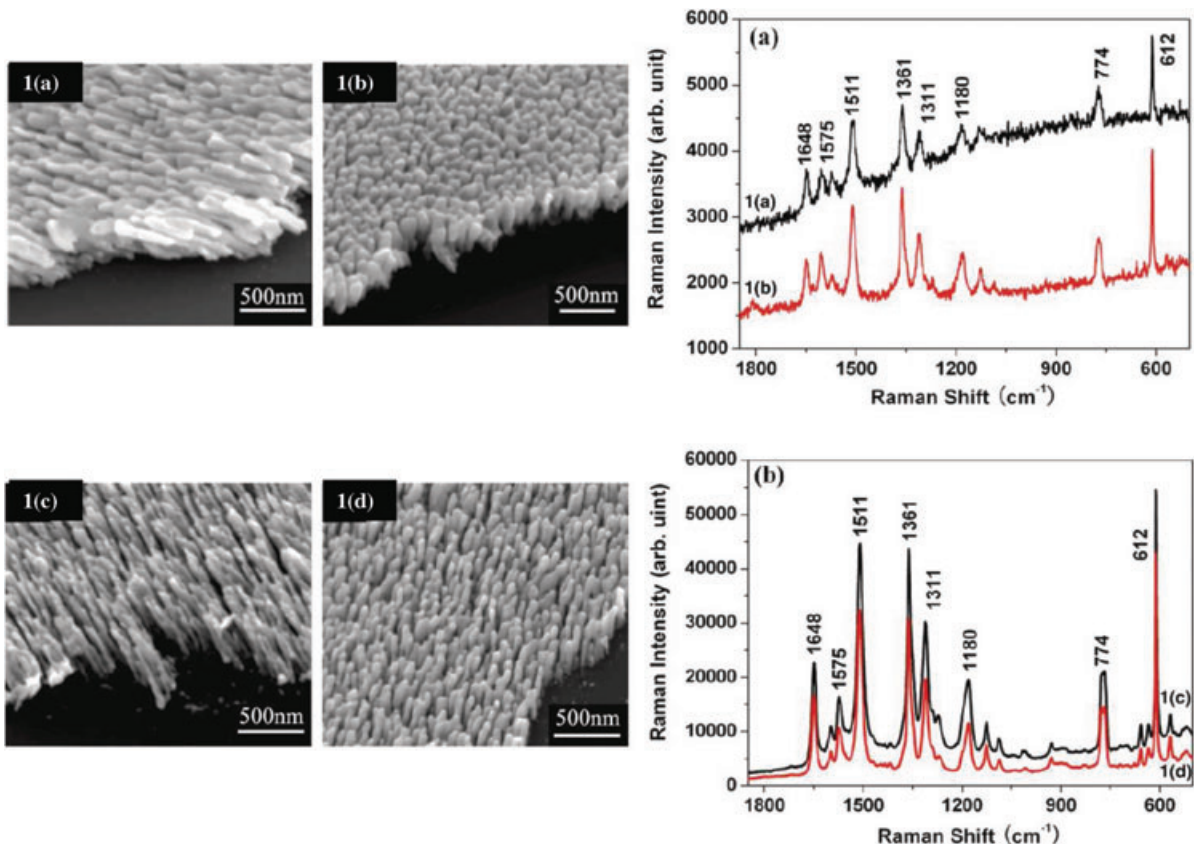

Figure 29 (online color at: www.lpr-journal.org) Growth morphology of Ag thin films by GLAD at various conditions (1a) at 120 ℃ without substrate rotation (1b) at 120 ℃ and substrate rotation at 0.2 rpm (1c) at −40 ℃ without substrate rotation (1d) at −40 ℃ and substrate rotation at 0.2 rpm (a) Raman spectra of R6G on Ag thin films consisting of (a) joined nanorods shown by Figs. 1a and b, and (b) separated Ag nanorods shown by Figs. 1c and d, respectively, at a concentration of 1×10^{-6} mol × L^{-1}. (Reproduced from [155], Qin Zhou et al. The parts (1a–d) were taken from Fig. 1, while parts (a) and (b) were taken from Fig. 3 in the original article).

nomenon with significant applications in biotechnology and life sciences [160]. Localization of the electromagnetic field near nanotips, corners, holes, needles, etc. has been shown to produce large SEF by factors of up to a few hundreds in what is known as the lightning nanoantenna effect [161]. A recent review article [162] summarized the fluorophore molecule interactions with the metal surface under SP waves excitation.

Surface-enhanced fluorescence from porous, metallic sculptured thin films (STFs) was demonstrated for sensing of bacteria in water by Abdulhalim et al. [163] Enhancement factors larger than 15 were observed using STFs made of silver, aluminum, gold, and copper with respect to their dense-film counterparts. The STFs used are assemblies of tilted, shaped, parallel nanowires prepared with several variants of the oblique-angle-deposition technique (OAD). Abdulhalim et al. [163] examined the effect of the substrate material, constituent rods material, porosity, and the rods tilt angle on the enhancement factor of SEF. Enhancement of SEF from porous, metallic STFs was applied to biosensing in water. The main SEF mechanisms, according to the authors, are believed to be the lightning nanoantenna effect and the dipole–dipole interaction. This observation makes STFs potential candidates as SEF nanobeds for biosensing and bioimaging. In Fig. 30, one can see the advantage of such sculptured films on their counterpart closed and flat films.

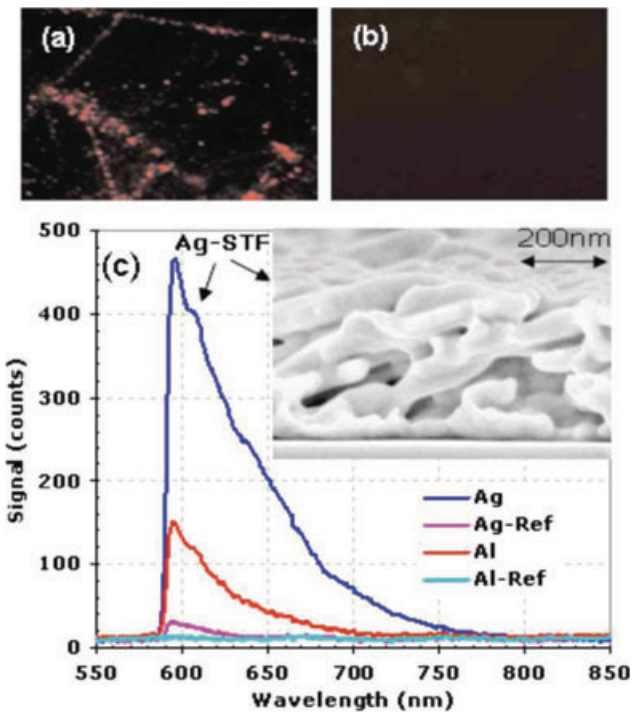

Figure 30 (online color at: www.lpr-journal.org) Fluorescence images from (a) Ag nanorod STF and (b) a dense Ag film immersed in an aqueous solution of luminescent *E. coli*. (c) Typical SEF spectra from an Ag nanorod STF and an Al-nanorod STF and from the corresponding reference films. Inset: SEM micrograph of an Ag nanorod STF showing the highest enhancement factor (Reproduced from Fig. 2 of [163], by I. Abdulhalim et al.)

4.3. Extraordinary optical transmission – EOT

In 1998 Ebbesen et al. [164] presented experimental results showing that periodic arrays of subwavelength holes in a metal film can exhibit structured light transmission spectra with peak maxima corresponding to a surprising amount of transmission in comparison with expectations based on Bethe theory [165]. Bethe theory is an analytical treatment of light transmission by a hole in a perfect metal that cannot support SP excitations. Recently, it was shown by Gordon [166] that in a periodic array of nanoapertures in a metal film, Bethe theory predicts almost 100% transmission at certain wavelengths. Hence, SP excitation of SPs is not necessarily required for the existence of EOT. This extraordinary optical transmission (EOT) phenomenon is also very sensitive to the nature of any substrate placed over the holes and so many researchers have explored the possibility of developing chemical and biological sensors based on such systems. Kang et al. [167] presented a simple theoretical model to study the effect of a substrate on the resonance of an aperture in a thin metal film. The transmitted energy through an aperture is shown to be governed by the coupling of an aperture waveguide mode to the incoming and the outgoing electromagnetic waves into the substrate region. Transmission of polarized light through subwavelength slit apertures was studied by Pang et al. [168] in the visible and near-infrared range wavelengths. The authors examined the roles played by the slit apertures, such as length, depth, period and number of slits. Birefringence aspects from plasmonic nanoslit arrays were presented by Hsu [169] and coworkers. The EOT through an array of nanoholes in a metal film was extensively studied and a few reviews were published [170,177]. Recently, the additional effects from variations in real metal properties at different wavelengths, film thicknesses, hole shape and lattice configuration were presented in a good review by Gordon and coworkers [170].

In the field of biosensing, Lee et al. [171] used the transmission spectra from 1D Au nanoslit arrays to detect changes in the refractive index of NaCl solutions. The adsorption of a self-assembled monolayer of molecules on a metal surface commonly causes a redshift in its surface plasmon resonance. Jung and coworkers [172] reported that the anomalous dispersion of surface plasmons in an Au nanoslit array structure can cause a blueshift of optical transmission upon adsorption of a nonabsorbing self-assembled monolayer of molecules. Brolo et al. [173] reported on 400 nm/RIU spectral sensitivities obtained from nanoholes in a gold film that was used to monitor the binding of organic and biological molecules to the metallic surface. In contrast to the commercial SPR sensors, the phase-matching condition for exciting SPs in zero-order transmission is given by the periodicity of the holes (Eq. (32)), and the prism coupling is not required. This simplified optical setup is more suitable for miniaturization. The combination of highly localized sensing area and simple setup, render these types of substrates ideal for the development of integrated biosensors in laboratory-on-chip devices [174, 175]. The device proposed by De Leebeeck et al. [174] demonstrated a spectral

Table 3 Sensitivity of nanoholes arrays with different geometries.

Geometry	Periodicity (nm)	λ (nm)	Width/diameter (nm)	Depth (nm)	Metal	Sensitivity (nm/RIU)	Ref.
Slits	1600	790	300	150	Au	563	171
Circles	510	645	200	100	Au	400	173
Circles	450	606	150	100	Au	333	174
Disordered holes	–	–	60, 110	20, 55	Au	80, 50	163
Square arrays	400, 450	–	100, 150	50, 100	Au	200, 333	179
Square array	600		90, 250	110	Au	420, 561	179
Square array of double holes	600	–	200	100	Au	600	182
Square array	1530	–	300	150, 200	Au	1570, 1110	179
Hexagonal array	450	–	250, 320	13, 48	Au	487, 226	179
Holes	450	554	120	50	Ag	400	179
Holes	450	882	310	50	Au	170	179
Holes	450	551–572	254	Ag 50–5 Au 0–45	Ag/Au bimetallic	242–253	179
Holes	600	835	150	110	Au	560	181
Holes on Kretschmann configuration	1500	600	900	50	Au	4244	180
Nanoslits	600	835	70	110	Au	650	181–184
Nanoslits	1000–17 000	1500–25 000	50	24	Ag	400–18 000	185
Concentric circles	600	870	70	110	Au	623	181

sensitivity of 333 nm/RIU that agrees well with the values predicted for gratings-based SPR devices and similar to the sensitivities obtained from sensing schemes based on metallic nanoparticles. The sensor output sensitivity obtained is an order of magnitude smaller than the values obtained from commercial angle-resolved SPR systems. This is not a fundamental limitation to the application of arrays of nanoholes for sensing. It is important to point out that the sensing area of the arrays of nanoholes is much smaller than that typical of SPR arrangement; hence, the magnitude of the wavelength shift originates from a smaller number of molecules. These considerations have been taken into account by Stark et al. [176]. Since the SP fields are tightly confined to the interface, another powerful approach for chemical sensing is to take advantage of this localization to produce enhanced molecular spectroscopy. Nanoholes in noble metals are a promising platform for enhanced spectroscopy because they not only confine the EM field but also restrict the analyte to very small volumes. Moreover, in contrast to colloidal particles dispersed on glass, the hot spots responsible for the field enhancement are specifically organized by the nanofabrication of the device. Table 3 demonstrated some of the nanoapertures and their spectral sensitivities. Gordon et al. [177] surveyed the application of nanoholes-based devices as substrates to surface-enhanced spectroscopy. They explored the dependence of EOT on the hole shape and its effect on sensing and enhanced spectroscopy. In this context, the authors presented a double-hole structure instead of the single hole. When the two holes overlap, two sharp apexes are created and act as an optical antenna that focuses the electromagnetic field to very small region at the sharp apexes [178]. Murray-Méthot and coworkers [179] recently investigated the optical properties and analytical response such as sensitivity, transmission intensity, and FWHM of various arrays. Ag and Au arrays with different periodicities, diameters and bimetallic nanoholes were examined. Sensitivity of 400 nm/RIU was observed for Ag nanohole arrays with the smallest hole diameter of 120 nm. Furthermore, bimetallic nanohole arrays composed of a Ag underlayer covered with Au exhibited an improved sensitivity, stability, and FWHM compared with nanohole arrays of pure metal. This field considerably accelerated in the last years, and the sensitivities of various shapes were examined [180]. Lee et al. [181] found that the sensitivities of nanohole arrays, concentric circles, and nanoslits are 560 nm/RIU, 623 nm/RIU, and 650 nm/RIU, respectively. The effect of a thin top atomic layer on the device performances was also recently investigated [182].

The resonance wavelength is found from the k-vector matching condition of SPR existence, $k_x = k_{SP}$, which for the case of 1d array of nanoslits at normal incidence (see Fig. 31a) and first-order diffracted wave gives:

$$\lambda_{SP} \approx \mathrm{Re}\left\{\Lambda\sqrt{\frac{\varepsilon_m\varepsilon_a}{\varepsilon_m+\varepsilon_a}}\right\} \tag{32}$$

where Λ is the period of the grating. Equation (32) is valid for the 1st resonance peak and for thick metal film; however, it is used as well for estimating the SPR location for thin metal films as the thickness of the metal film has negligi-

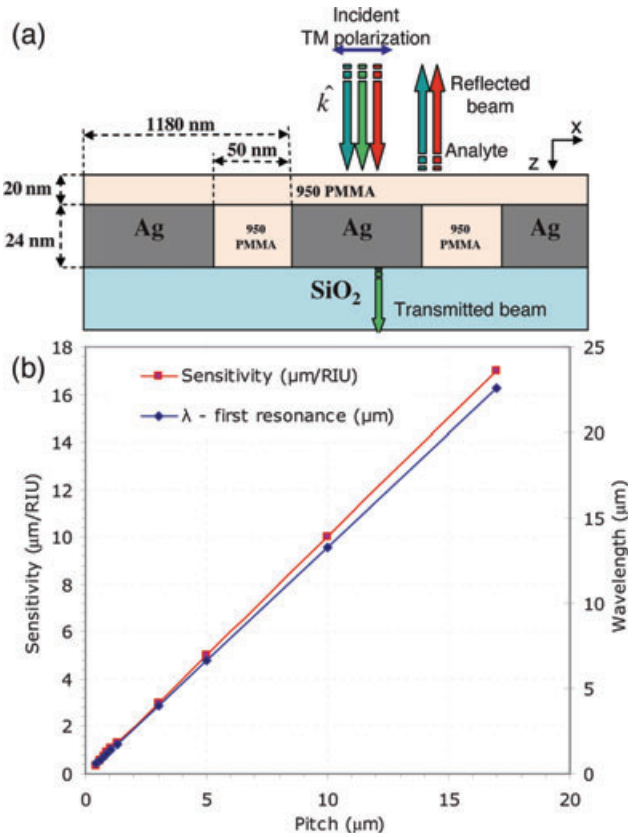

Figure 31 (online color at: www.lpr-journal.org) (a) Cross section of typical EOT based sensor using 1D array of nanoslits. (b) Spectral sensitivity and resonance wavelength versus the pitch of the structure parameters as indicated in (a). The simulations are based on the rigorous coupled wave analysis.

ble effect on the k-vector of the plasmon. The fact that the wavevector-matching condition is satisfied indicates that a propagating surface plasmon is excited and not a localized one even though the apertures have nonscale size. The sensitivity of the sensor is measured in nm per refractive index units (nm/RIU) defined as the slope of the variation λ_{SP} with the analyte index $n_a = \sqrt{\varepsilon_a}$ and can be derived from Eq. (32) in a similar manner to the grating coupled PSPR case:

$$S_\lambda = \frac{\lambda_{SP}}{\sqrt{\varepsilon_a}} \times \mathrm{Re}\left\{ \frac{\varepsilon_m}{(\varepsilon_m + \varepsilon_a) - 0.5\lambda_{SP}\frac{\varepsilon_a}{\varepsilon_m}\frac{\partial \varepsilon_m}{\partial \lambda} - 0.5\lambda_{SP}\frac{\varepsilon_m}{\varepsilon_a}\frac{\partial \varepsilon_a}{\partial \lambda}} \right\}. \quad (33)$$

Hence, only when the metal and the analyte dispersions are ignored does the sensitivity scale linearly with the structure period Λ and the wavelength. Since usually in the IR region $|\varepsilon_{mr}| \gg \varepsilon_a$, Eq. (33) leads to $S_\lambda \approx \lambda_{SP}/n_a$. Hence, larger sensitivities can be obtained by designing EOT sensors with resonances in the infrared range. Experimental demonstration for water pollution sensing was presented by Karabchevsky et al. [183, 184] in the visible range of the spectrum and in the near-infrared by Krasnykov et al. [185] (see Fig. 31b).

One can see from Table 3 that the spectral sensitivity of nanohole-based arrays scales with the periodicity of the device. This fact is observable in square arrays for example, increasing the period of the structure yields an increase in the sensitivity. Since the resonance wavelength redshifts when the period is larger, the sensitivity is expected to be larger when considering the same metal. Furthermore, producing an array of double holes causes an enhancement in the sensitivity relative to the single-hole structure counterpart array. The latter fact apparently originates from the EM field enhancement in the vicinity of the apexes created due to the double-hole structure.

5. Summary and future directions

During the last 20 years the surface plasmon resonance sensing technique was developed into a very useful technology with numerous applications. Surface plasmons, which are collective oscillations of electrons in small particles or on metal/dielectric interfaces induced by an incident electromagnetic field, have been a topic of tremendous interest and the whole new field of "plasmonics" is dealing with this phenomenon [186]. In recent years, the potential of plasmonics has been realized in making highly sensitive and very small photonic devices. Among the main characteristics of plasmonic sensors are their high sensitivity, possibility for biochip buildup and the ability to specify the material being sensed. A wide range of applications arising from controlling the light at the nanoscale such as high-resolution optical imaging below the diffraction limit, enhanced optical transmission through subwavelength apertures [187], biodetection at the femtomole level, nanoscale waveguiding, and surface-enhanced Raman scattering have been established. Many futuristic applications are also inspiring research in this field. Improving the sensitivity of plasmonic devices that are designated to biosensing is highly important beside many other characteristics that should be improved. This paper has reviewed briefly the basics of surface plasmon generation and detection, particularly in the context of sensing. Sensitivity enhancement was shown to originate from the enhancement of the overlap integral that is basically determined by the interaction volume and the field strength. Enhancing the local field or the penetration depth are the most common ways of enhancing the interaction integral in evanescent field sensing. The recent advances in enhancing sensitivity methods have also been reviewed. LSPR, enhanced surface spectroscopy, EOT as well as propagating SPR structures were considered. Although this field experienced a tremendous progress in the last few decades, many aspects of fabrication and stabilization, miniaturizing, integration with electronic devices, flexibility and controlling performances are also needed. Biochip buildup from planar structures is becoming feasible, particularly with arrays of nanoholes or nanoslits in metals as they can be produced in large area on glass substrates. Nanoparticles of different shapes are being explored almost weekly for the purpose of tuning the resonance wavelength and enhancing the sensitivity [188–191]. Nanosculptured

metallic thin films is another area of practical interest as they can be produced with oblique-angle deposition techniques in large areas and they can be patterned and the nanofeatures can be controlled in size and shape. Their porosity and anisotropic nature reveal additional interesting features to the SPR response that might be used for sensitivity improvement. PSPR on the surface of anisotropic films has recently caught the attention of several researchers exhibiting several novel phenomena. Excitation of TE and TM SP waves at the interface between thin anisotropic film and metal was shown [192] to be possible in the Otto configuration with the anisotropic layer being thicker than the evanescent region. Total absorption occurs at specific wavelengths or incidence angles both for TE and TM waves. Polarization conversion at the resonance was also shown to occur when both modes are excited in the anisotropic layer. Tuning the orientation of the dielectric tensor ellipsoid or its principal values was shown to allow tuning of the resonance location. It was shown recently [193, 194] that it is possible to excite SP waves directly on the interface of a uniaxial medium and metal. Both TE and TM SP waves were shown to be possible with large sensitivity to the orientation of the optic axis. Morphological effects for the excitation of SPP waves at the interface with structurally chiral films were recently reported [195, 196] and multiple SPR excitations were observed numerically [197, 198]. Another interesting topic is the coupling between plasmons and excitons when a top nanolayer of semiconductor quantum dots is deposited on the metal layer, as was demonstrated recently [199] and might reveal new type of devices with enhanced sensitivity different from the other enhancement mechanisms. Deep metallic gratings and metallic gratings combined with guided-wave resonances are another interesting structure that can enhance the sensitivity and improve the reliability [200, 201].

After two decades of extensive research work on optical sensing using metallic nanostructures, the time is approaching for true products to emerge. Sensors based on the PSPR in Kretchmann configuration have been available commercially for more than two decades now and the time has come to start commercializing sensors based on LSPR. The manufacturability of nanostructures is becoming mature in different ways such as chemical means, nanolithography, direct writing and deposition of thin films. All this combined with the explosion of information technology, computing power, miniature detection devices such as spectrometers, cameras and lenses is expected to bring a true revolution in biosensing. For example, miniature Raman and fluorescence spectrometers are available today at reasonable price that when combined with nanostructures to obtain high SERS and SEF signals can provide a powerful tool for monitoring and sensing.

Acknowledgements. The authors would like to thank the following colleagues for their collaboration during the last few years on several topics related to the subject of this article: Mrs. Alina Karabchevsky, Ms. Olga Krasnykov, Mr. Amit Lahav, Prof. Mark Auslender, Prof. Robert Marks, Prof. Akhlesh Lakhtakia, Prof. Bernd Rauschenbach, Dr. Christian Patzig, Mr. Chinmay Khare, and Dr. M. Zourob.

Received: 18 April 2010, **Revised:** 3 January 2011, **Accepted:** 21 January 2011

Published online: 29 March 2011

Key words: SPR sensors, plasmonics, biosensors, optical sensors.

Atef Shalabney received his bachelor of sciences in electrical engineering from the Technion, Institute of Technology, Hafia, Israel in 1997, and a masters degree in electro-optics engineering from the Ben Gurion University, Beer Shiva, Israel in 2009. Currently, he is a Ph. D. student in electro-optics engineering at Ben Gurion University. His research interests are plasmonic structures and optical biosensing devices.

Ibrahim Abdulhalim studied physics at the Technion, Haifa, where he received his B. Sc., M. Sc. and D. Sc. in 1982, 1985 and 1988, respectively. He spent several years working in applied optics and devices in academia and industry such as in the OCS in the University of Colorado at Boulder, in the ORC at Southampton University, in the University of Western Scotland, in KLA-Tencor Corporation, in Nova Measuring Instruments and in GWS-Photonics. In October 2005 Prof. Abdulhalim joined the Ben Gurion University, department of electro-optic engineering. His current research activities involve nanophotonic structures for biosensing, improved biomedical optical imaging techniques such as spectropolarimetric imaging and full-field optical coherence tomography.

References

[1] A. V. Zayats, I. I. Smolyaninov, and A. A. Maradudin, Phys. Rep. **408**, 131–314 (2005).
[2] J. M. Pitarke, V. M. Silkin, E. V. Chulkov, and P. M. Echenique, Rep. Prog. Phys. **70**, 1–87 (2007).
[3] I. Abdulhalim, M. Zourob, and A. Lakhtakia, Electromagnetics (UK) **28**, 214–242 (2008).
[4] H. Raether, Surface Plasmons on Smooth and Rough Surfaces and on Gratings, Springer Tracts in Modern Physics, Vol. 111 (Springer, Berlin Heidelberg New York, 1988).
[5] B. Liedberg, C. Nylander, and I. Lunström, Sens. Actuators **4**, 299–304 (1983).
[6] C. E. H. Berger, T. A. M. Beumer, R. P. H. Kooyman, and J. Greve, Anal. Chem. **70**, 703–706 (1998).
[7] K. A. Peterlinz, and R. M. Georgiadis, T. M. Herne, and M. J. Tarlov, J. Am. Chem. Soc. **119**, 3401–3402 (1997).
[8] V. Owen, Biosens. Bioelectron. (UK) **12**(1), i–ii (1997).
[9] J. Homola, S. S. Yee, and G. Gauglitz, Sens. Actuators B **54**, 3–15 (1999).
[10] J. Homola, Anal Bioanal. Chem. **377**, 528–539 (2003).

[11] E. M. Yeatman, Biosens. Bioelectron. (UK) **11**, 635–649, (1996).
[12] A. A. Kolomenskii, P. D. Gershon, and H. A. Schuessler, Appl. Opt. **36**, 6539–6547 (1997).
[13] J. M. McDonnell, Curr. Opin. Chem. Biol. **5**, 572–577 (2001).
[14] A. N. Naimushin, S. D. Soelberg, D. K. Nguyen, L. Dunlap, D. Bartholomew, J. Elkind, J. Melendez, and C. E. Furlong, Biosens. Bioelectron. (UK) **17**, 573–584 (2002).
[15] Y. Sun, and Y. Xia, Anal. Chem. **74**, 5297–5305 (2002).
[16] A. P. F. Turner, Science **290**, 1315 – 1317 (2000).
[17] A. J. Haes, and R. P. Van Duyne, Mat. Res. Soc. Symp. Proc. **723**, O3.1.1–6 (2002).
[18] T. R. Jensen, R. P. Van Duyne, S. A. Johnson, and V. A. Maroni, Appl. Spectrosc. **54**(7), 88A–113A, 331–459, 371–377 (2000).
[19] W. P. Hu, S. -J. Chen, K. -T. Huang, J. H. Hsu, W. Y. Chen, G. L. Chang, and K. -A. Lai, Biosens. Bioelectron. (UK) **19**, 1465–1471 (2004).
[20] R. B. M. Schasfoort, and A. J. Tudos, Handbook of Surface Plasmon Resonance (The Royal Society of Chemistry, Cambridge, 2008).
[21] J. Homola, I. Koudela, and S. S. Yee, Sens. Actuators B **54**, 16–24 (1999).
[22] K. A. Willets, and R. P. Van Duyne, Annu. Rev. Phys. Chem. **58**, 267–97 (2007).
[23] N. G. Khlebtsov, Quantum Electron. **38**, 504–529 (2008).
[24] H. C. Van de Hulst, Light Scattering by Small Particles (Dover, New York, (1981).
[25] W. T. Doyle, Phys. Rev. **111**, 1067–1072 (1958).
[26] R. H. Doremus, J. Chem. Phys. **40**, 2389 (1964).
[27] U. Kreibig, and M. Vollmer, Optical Properties of Metal Clusters (Springer-Verlag, Berlin, 1995).
[28] J. D. Eversole, and H. P. Broida, Phys. Rev. B **15**, 1644–1655 (1977).
[29] W. T. Doyle, Phys. Rev. B , **39**, 9852–9858 (1989).
[30] J. M. Montgomery, T.-W. Lee, and S. K. Gray, J. Phys., Condens. Matter **20**, 323201 (2008).
[31] E. Fort, and S. Gresillon, J. Phys. D, Appl. Phys. **41**, 13001 (2008).
[32] E. C. Stoner, Philos. Mag. **36**(63), 803 (1945).
[33] L. S. Jung, C. T. Campbell, T. M. Chinowsky, M. N. Mar, and S. S. Yee, Langmuir **14**, 5636–5648 (1998).
[34] I. Abdulhalim, Optical waveguide sensing and imaging, NATO Science for Peace and Security Series B, Physics and Biophysics, edited by W. J. Bock, I. Gannot, and S. Tanev (Springer-Verlag, Netherlands, 2007), pp. 211–228.
[35] T. J. Davis, Opt. Commun. **282**, 135–140 (2009).
[36] C. B. Su, and J. Kameoka, Meas. Sci. Technol. **19**, 015204 (2008).
[37] K. Ohta, and H. Ishida, Appl. Opt. **29**, 1952–1959 (1990).
[38] S. Ekgasit, C. Thammacharoen, and W. Knoll, Anal. Chim. **76**, 561–568 (2004).
[39] W. Hansen, J. Opt. Soc. Am. **58**, 380–390 (1968).
[40] A. Shalabney, and I. Abdulhalim, Sens. Actuators A, **159**, 24–32 (2010).
[41] N. J. Harrick, Internal Reflection Spectroscopy (Harrick Scientific Corp, New York, 1987)
[42] J. D. E. McIntyre, in: Optical Properties of Solids – New Developments, edited by B. O. Seraphin (North-Holland Publishing Co., Amsterdam, 1967), pp. 555–630.
[43] S. Ekgasit, S. Appl. Spectrosc. **52**, 773–776 (1998).
[44] J. V. Gent, P. Lambeck, H. Kreuwel, G. Gerritsma, E. Sudholter, D. Reinhoudt, and T. Popma, Appl. Opt. **29**, 2843-2849 (1990).
[45] B. A. Snopok, Semicond. Phys. Quantum Electron. Optoelectron. **4**, 56–69 (2001).
[46] P. Nagpal, N. C. Lindquist, S.-H. Oh, and D. J. Norris, Science **325**, 594–597 (2009).
[47] J. Homola, Sens. Actuators B **41**, 207–211 (1997).
[48] X. -C. Yuan, B. H. Ong, Y. G. Tan, D. W. Zhang, R. Irawan, and S. C. Tjin, J. Opt. A, Pure Appl. Opt. **8**, 959–963 (2006).
[49] P. Lecaruyer, M. Canva, and J. Rolland, Appl. Opt. **46**, 2361–2369 (2007).
[50] J. S. Yuk, D. G. Hong, J. W. Jung, S. H. Jung, H. S. Kim, J. A. Han, Y. M. Kim, and K. S. Ha, Eur. Biophys. J **35**, 469–476 (2006).
[51] G. Gupta, and J. Kondoh, Sens. Actuators B, **122**, 381–388 (2007).
[52] Z. Salamon, H. A. Macleod, and G. Tollin, Biochim. Biophys. Acta **1331**, 117–129 (1997).
[53] Z. Salamon, H. A. Macleod, and G. Tollin, Biochim. Biophys. Acta **1331**, 131–152 (1997).
[54] S. Toyama, N. Doumae, A. Shoji, and Y. Ikariyama, Sens. Actuators B **65**, 32–34 (2000).
[55] Z. Salamon, and G. Tollin, Biophys. J. **80**, 1557–1567 (2001).
[56] J. M. McDonnell, Curr. Opin. Chem. Biol. **5**, 572–577 (2001).
[57] A. Lahav, M. Auslender, and I. Abdulhalim, Opt. Lett. **33**, 2539–2541 (2008).
[58] A. Lahav, A. Shalabaney, and I. Abdulhalim, J. Nanophotonics, **3**, 031501 (2009).
[59] M. J. Jory, P. S. Vukusic, and J. R. Sambles, Sens. Actuators B **17**, 203–209 (1994).
[60] U. Schroter, and D. Heitmann, Phys. Rev. B **60**, 4992–4999 (1999).
[61] M. Masale, Physica B **325**, 385–393 (2003).
[62] Z. Zhaoming, and T. G. Brown, J. Opt. Soc. Am. A **17**, 1798–1806 (2000).
[63] W. L. Barnes, T. W. Preist, S. C. Kitson, and J. R. Sambles, Phys. Rev. B **54**, 6227–6244 (1996).
[64] C. J. Alleyne, A. G. Kirk, R. C. McPhedran, N.-A. P. Nicorovici, and D. Maystre, Opt. Express **15**, 8163–8169 (2007).
[65] S. Park, G. Lee, S. H. Song, C. H. Oh, and P. S. Kim, Opt. Lett. **28**, 1870–1872 (2003).
[66] C. Lenaerts, F. Michel, B. Tilkens, Y. Lion, and Y. Renotte, Appl. Opt. **44**, 6017–6022 (2005).
[67] S. Shen, E. Forsberg, Z. Han, and S. He, J. Opt. Soc. Am. A **24**, 225–230 (2007).
[68] K. M. Byun, S. J. Kim, and D. Kim, Appl. Opt. **46**, 5703–5708 (2007).
[69] W. Bin, and W. Q. Kang, Chin. Phys. Lett. **25**, 1668–1671 (2008).
[70] D. Sarid, Phys. Rev. Lett. **47**, 1927–1930 (1981).
[71] D. Sarid, R. T. Deck, A. E. Craig, R. K. Hickernell, R. S. Jameson, and J. J. Fasano, Appl. Opt. **21**, 3933–3995 (1982).
[72] R. T. Deck, D. Sarid, G. A. Olson, and J. M. Elson, Appl. Opt. **22**, 3397–3405 (1983).
[73] J. C. Quail, J. G. Rako, and H. J. Simon, Opt. Lett. **8**, 377–379 (1983)
[74] G. G. Nenninger, P. Tobiška, J. Homola, and S. S. Yee, Sens. Actuators B **74**, 145–151 (2001).

[75] F. C. Chien, and S. J. Chenb, Biosens. Bioelectron. (UK) **20**, 633–642 (2004).
[76] R. Slavik, and J. Homola, Sens. Actuators B **123**, 10–12 (2007).
[77] M. Vala, S. Etheridge, J. A. Roach, and J. Homola, Sens. Actuators B **139**, 59–63 (2009).
[78] R. Jha, and A. K. Sharma, J. Opt. A, Pure Appl. Opt. **11**, 045502 (2009).
[79] M. Golosovsky, V. Lirtsman, V. Yashunsky, D. Davidov, and B. Aroeti, J. Appl. Phys. **105**, 102036 (2009).
[80] V. Lirtsman, R. Ziblat, M. Golosovsky, and D. Davidov, J. Appl. Phys. **98**, 093506 (2005).
[81] S. Herminjard, L. Sirigu, H. Peter Herzig, E. Studemann, A. Crottini, J.-P. Pellaux, T. Gresch, M. Fischer, and J. Faist, Opt. Express, **17**, 293–303 (2009).
[82] S. Patskovsky, A. V. Kabashin, and M. Meunier, J. Opt. Soc. Am. A **20**, 1644–1650 (2003).
[83] S. Patskovsky, A. V. Kabashin, M. Meunier, and J. H. T. Luongb, Sens. Actuators B **97**, 409–414 (2004).
[84] A. V. Kabashin, and P. I. Nikitin, Quantum Electron. **27**(7), 653–654 (1997).
[85] A. V. Kabashin, and P. I. Nikitin, Opt. Commun. **150**, 5–8 (1998).
[86] S. Y. Wu, H. P. Ho, W. C. Law, C. Lin, and S. K. Kong, Opt. Lett. **29**, 2378–2380 (2004).
[87] J.-Y. Lee, H.-C. Shih, C.-T. Hong, and T. Ko Chou, Opt. Commun. **276**, 283–287 (2007).
[88] H. P. Ho, W. Yuan, C. L. Wong, S. Y. Wu, Y. K. Suen, S. K. Kong, and C. Lin, Opt. Commun. **275**, 491–496 (2007).
[89] B. Ran, and S. G. Lipson, Opt. Express **14**, 5641–5650 (2006).
[90] A. V. Kabashin, S. Patskovsky, and A. N. Grigorenko, Opt. Express **17**, 21191–21204 (2009).
[91] S. Patskovsky, M. Vallieres, M. Maisonneuve, I.-H. Song, M. Meunier, and A. V. Kabashin, Opt. Express **17**, 2255–2263 (2009).
[92] S.-F. Wang, M.-H. Chiu, C.-W. Lai, and R.-S. Chang, Appl. Opt. **45**, 6702–6707 (2006).
[93] W. Yuan, H. P. Hoa, S. Y. Wua, Y. K. Suen, and S. K. Kong, Sens. Actuators A **151**, 23–28 (2009).
[94] M. Meunier, P. N. Prasad, A. V. Kabashin, and S. Patskovsky, Opt. Express **18**, 14353–14358 (2010).
[95] L. Liu, Z. Hu, S. Ma, Y. Zhang, Y. He, and J. Guo, Opt. Lasers Eng., in press (2010).
[96] C. L. Wong, H. P. Ho, T. T. Yu, Y. K. Suen, W. W. Y. Chow, S. Y. Wu, W. C. Law, W. Yuan, W. J. Li, S. K. Kong, and C. Lin, Appl. Opt. **46**, 2325–2332 (2007).
[97] J.-Y. Lee, T.-K. Chou, and H.-C. Shih, Opt. Lett. **33**, 434–436 (2008).
[98] M.-H. Chiu, Opt. Lett. **30**, 233–235 (2005).
[99] T. Yang, and H. P. Ho, Opt. Express, **17**, 11205–11216 (2009).
[100] www.bioptix.com, www.cambridgeconsultants.com/news_pr76.html.
[101] M. Piliarik, and J. Homola, Opt. Express **17**, 16505–16517 (2009).
[102] A. Karabchevsky, S. Karabchevsky, and I. Abdulhalim, Sens. Actuators B, Chem., in press (2011), doi:10.1016/j.snb.2010.12.012.
[103] E. A. Smith, M. G. Erickson, A. T. Ulijasz, B. Weisblum, and R. M. Corn, Langmuir **19**, 1486–1492 (2003).
[104] Y. Chen, A. Nguyen, L. Niu, and R. M. Corn, Langmuir **25**, 5054–5060 (2009).
[105] G. J. Wegner, H. Jin Lee, and R. M. Corn, Analytical Chemistry **74**, 5161–5168 (2002).
[106] G. J. Wegner, H. Jin Lee, G. Marriott, and R. M. Corn, Anal. Chem. **75**, 4740–4746 (2003).
[107] E. A. Smith, W. D. Thomas, L. L. Kiessling, and R. M. Corn, J. Am. Chem. Soc. **125**, 6140–6148 (2003).
[108] A. L. Hook, H. Thissen, and N. H. Voelcker, Langmuir **25**, 9173–9181 (2009).
[109] J. Jung, J. Seol Yuk, K. Na, O. Kim, J. Lee, K. Yun, K.-S. Ha, and J. Hyun, Langmuir **23**, 10403–10406 (2007).
[110] K. D. Kihm, Exp. Fluids **48**, 547–564 (2010).
[111] C. Hoon Choi, and A. C. Hillier, Anal. Chem. **82**, 6293–6298 (2010).
[112] A. Ishimaru, S. Jaruwatanadilok, and Y. Kuga, Prog. Electromagn. Res. **51**, 139–152 (2005).
[113] F. Yang, G. W. Bradberry, and J. R. Sambles, Thin Solid Films **196**, 35–46, (1991).
[114] A. I. Maaroof, A. Gentle, G. B. Smith, and M. B. Cortie, J. Phys. D, Appl. Phys. **40**, 5675–5682 (2007).
[115] A. Shalabney, A. Lakhtakia, I. Abdulhalim, A. Lahav, C. Patzig, I. Hazek, A. Karabchevsky, B. Rauschenbach, F. Zhang, and J. Xu, Photonics Nanostructures Fundam. Appl. **7**, 176–185 (2009).
[116] S. A. Kalele, N. R. Tiwari, S. W. Gosavi, and S. K. Kulkarni, J. Nanophotonics, **1**, 012501 (2007).
[117] S. Link, and M. A. El-Sayed, J. Phys. Chem. B **103**, 4212–4217 (1999).
[118] M. Pelton, J. Aizpurua, and G. Bryant, Laser Photon. Rev. **2**, 136–159 (2008).
[119] T. R. Jensen, M. Duval Malinsky, C. L. Haynes, and R. P. Van Duyne, J. Phys. Chem. B **104**, 10549–10556 (2000).
[120] S. Peng, J. M. McMahon, G. C. Schatz, S. K. Gray, and Y. Sun, PNAS **107**, 14530–14534 (2010).
[121] M. M. Miller, and A. A. Lazarides, J. Opt. A, Pure Appl. Opt. **8**, S239–S249 (2006).
[122] K.-S. Lee, and M. A. El-Sayed, J. Phys. Chem. B **110**, 19220–19225 (2006).
[123] J. Pérez-Juste, I. Pastoriza-Santos, L. M. Liz-Marzán, and P. Mulvaney, Coord. Chem. Rev. **249**, 1870–1901 (2005).
[124] A. J. Haes, and R. P. Van Duyne, SPIE **5221**, 47–58 (2003).
[125] J. Fu, B. Park, and Y. Zhao, Sens. Actuators B, Chem. **141**, 276–283 (2009).
[126] K. Hamamoto, R. Micheletto, M. Oyama, A. Ali Umar, S. Kawai, and Y. Kawakami, J. Opt. A, Pure Appl. Opt. **8**, 268–271 (2006).
[127] E. M. Hicks, X. Zhang, S. Zou, O. Lyandres, K. G. Spears, G. C. Schatz, and R. P. Van Duyne, J. Phys. Chem. B **109**, 22351–22358 (2005).
[128] L. Guo, G. Chen, and D.-H. Kim, Anal. Chem. **82**, 5147–5153 (2010).
[129] J. McPhillips, A. Murphy, M. P. Jonsson, W. R. Hendren, R. Atkinson, F. Hook, A. V. Zayats, and R. J. Pollard, ACS Nano **4**, 2210–2216 (2010).
[130] C. Li, C. Wu, J. Zheng, J. Lai, C. Zhang, and Y. Zhao, Langmuir **26**, 9130–9135 (2010).
[131] A. V. Kabashin, P. Evans, S. Pastkovsky, W. Hendren, G. A. Wurtz, R. Atkinson, R. Pollard, V. A. Podolskiy, and A. V. Zayats, Nature Mater. **8**, 867–871 (2009).
[132] W.-C. Law, K.-T. Yong, A. Baev, R. Hu, and P. N. Prasad, Optic Express **17**, 19041–19046 (2009).

[133] J. N. Anker, W. Paige Hall, O. Lyandres, N. C. Shah, J. Zhao, and R. P. Van Duyne, Nature Mater. **7**, 442–453 (2008).
[134] A. B. Dahlin, J. O. Tegenfeldt, and F. Höök, Anal. Chem. **78**, 4416–4423 (2006).
[135] K. J. Lee, P. D. Nallathamby, L. M. Browning, C. J. Osgood, and X.-H. Nancy Xu, ACS Nano **1**, 133–143 (2007).
[136] A. J. Haes, S. Zou, J. Zhao, G. C. Schatz, and R. P. Van Duyne, J. Am. Chem. Soc. **128**, 10905–10914 (2006).
[137] J. Zhao, L. Jensen, J. Sung, S. Zou, G. C. Schatz, and R. P. Van Duyne, J. Am. Chem. Soc. **129**, 7647–7656 (2007).
[138] K.-H. Su, Q.-H. Wei, and X. Zhang, J. J. Mock, D. R. Smith, and S. Schultz, Nano Lett. **3**, 1087–1090 (2003).
[139] P. K. Jain, W. Huang, and M. A. El-Sayed, Nano Lett. **7**, 2080–2088 (2007).
[140] W. Rechberger, A. Hohenau, A. Leitner, J. R. Krenn, B. Lamprecht, and F. R. Aussenegg, Opt. Commun. **220**, 137–141 (2003).
[141] P. K. Jain, and M. A. El-Sayed, Nano Lett. **8**, 4347–4352 (2008).
[142] P. K. Jain, W. Huang, and M. A. El-Sayed, Nano Lett. **7**, 2080–2088 (2007).
[143] S. Zou, Opt. Lett. **33**, 2113–2115 (2008).
[144] S. Kim, J.-M. Jung, D.-G. Choi, H.-T. Jung, and S.-M. Yang, Langmuir **22**, 7109–7112 (2006).
[145] F. Hao, C. L. Nehl, J. H. Hafner, and P. Nordlander, Nano Lett. **7**, 729–732 (2007).
[146] H. Iu, J. Li, H. C. Ong, and J. T. K. Wan, Opt. Express **16**, 10294–10302 (2008).
[147] A. J. Haes, and R. P. Van Duyne, J. Am. Chem. Soc. **124**, 10596–10604 (2002).
[148] E. Ringe, J. M. McMahon, K. Sohn, C. Cobley, Y. Xia, J. Huang, G. C. Schatz, L. D. Marks, and R. P. Van Duyne, J. Phys. Chem. C **114**, 12511–12516 (2010).
[149] H. Wang, D. W. Brandl, F. Le, P. Nordlander, and N. J. Halas, Nano Lett. **6**, 827–832 (2006).
[150] Z. Zhang, and Y. Zhao, J. Phys., Condens. Matter, **20**, 345223 (2008).
[151] H. Xu, E. J. Bjerneld, M. Käll, and L. Börjesson, Phys. Rev. Lett. **83**, 4357–4360 (1999).
[152] M. Kerker, D.-S. Wang, and H. Chew, Appl. Opt. **19**, 3373–3388 (1980).
[153] G. C. Schatz, and R. P. Van Duyne, Reproduced from: Handbook of Vibrational Spectroscopy, edited by J. M. Chalmers and P. R. Griffiths (John Wiley & Sons Ltd, Chichester, 2002).
[154] N. Felidj, J. Aubard, G. Levi, J. R. Krenn, A. Hohenau, G. Schider, A. Leitner, and F. R. Aussenegg, Appl. Phys. Lett. **82**, 3095–3097 (2003).
[155] Q. Zhou, Z. Li, Y. Yang, and Z. Zhang, J. Phys. D, Appl. Phys. **41**, 152007 (2008).
[156] J. B. Jackson, S. L. Westcott, L. R. Hirsch, J. L. West, and N. J. Halas, Appl. Phys. Lett. **82**, 257–259 (2003).
[157] Y. Wang, X. Zou, W. Ren, W. Wang, and E. Wang, J. Phys., Chem. C **111**, 3259–3265 (2007).
[158] G. Kumar, D. B. Singh, and V. K. Tripathi, J. Phys., Appl. Phys. D **39**, 4436–4439 (2006).
[159] K. Aslan, I. Gryczynski, J. Malicka, E. Matveeva, J. R. Lakowicz, and C. D. Geddes, Curr. Opin. Biotechnol. **16**, 55–62 (2005).
[160] E. Fort, and S. Grésillon, J. Phys. D, Appl. Phys. **41**, 013001 (2008).
[161] M. Moskovits, Rev. Mod. Phys. **57**, 783–826 (1985).
[162] Y. Fu, and J. R. Lakowicz, Laser Photon. Rev. **3**, 221–232 (2009).
[163] I. Abdulhalim, A. Karabchevsky, C. Patzig, B. Rauschenbach, B. Fuhrmann, E. Eltzov, R. Marks, J. Xu, F. Zhang, and A. Lakhtakia, Appl. Phys. Lett. **94**, 063106–200 (2009).
[164] T. W. Ebbesen, H. J. Lezec, H. F. Ghaemi, T. Thio, and P. A. Wolff, Nature **391**, 667–669 (1998).
[165] H. A. Bethe, Phys. Rev., **66**, 163 (1944).
[166] R. Gordon, Phys. Rev. A **76**, 053806 (2007).
[167] J. H. Kang, J.-H. Choe, D. S. Kim, and Q.-H. Park, Opt. Express **17**, 15652–15658 (2009).
[168] Y. Pang, C. Genet, and T. W. Ebbesen, Opt. Commun. **280**, 10–15 (2007).
[169] S.-Y. Hsu, K.-L. Lee, E.-H. Lin, M.-C. Lee, and P.-K. Wei, Appl. Phys. Lett. **95**, 0131051–3 (2009).
[170] R. Gordon, A. G. Brolo, and D. Sinton, Laser Photon. Rev. **4**, 311–335 (2010).
[171] M. Hyung Lee, H. Gao, and T. W. Odom, Nano Lett. **9**, 2584–2588 (2009).
[172] Y. S. Jung, J. Wuenschell, H. K. Kim, P. Kaur, and D. H. Waldeck, Opt. Express **17**, 16081–16091 (2009).
[173] A. G. Brolo, R. Gordon, B. Leathem, and K. L. Kavanagh, Langmuir **20**, 4813–4815 (2004).
[174] A. De Leebeeck, L. K. Swaroop Kumar, V. de Lange, D. Sinton, R. Gordon, and A. G. Brolo, Anal. Chem. **79**, 4094–4100 (2007).
[175] K. A. Tetz, L. Pang, and Y. Fainman, Opt. Lett. **31**, 1528–1530 (2006).
[176] P. R. H. Stark, A. E. Halleck, and D. N. Larson, Nature Methods **37**, 37–47 (2005).
[177] R. Gordon, D. Sinton, K. L. Kavanagh, and A. G. Brolo, Acc. Chem. Res. **41**, 1049–1057 (2008).
[178] A. Lesuffleur, H. Im, N. C. Lindquist, and S. H. Oh, Appl. Phys. Lett. **90**, 243110 (2007).
[179] M.-P. Murray-Méthot, M. Ratel, and J.-F. Masson, J. Phys. Chem. C **114**, 8268–8275 (2010).
[180] L. S. Live, O. R. Bolduc, and J.-F. Masson, Anal. Chem. **82**, 3780–3787 (2010).
[181] K.-L. Lee, W.-S. Wang, and P.-K. Wei, Plasmonics **3**, 119–125 (2008).
[182] H. Im, N. C. Lindquist, A. Lesuffleur, and S.-H. Oh, ACS Nano **4**, 947–954 (2010).
[183] A. Karabchevsky, O. Krasnykov, M. Auslender, B. Hadad, A. Goldner, and I. Abdulhalim, J. Plasmonics **4**, 281–292 (2009).
[184] A. Karabchevsky, O. Krasnykov, I. Abdulhalim, B. Hadad, A. Goldner, M. Auslender, and S. Hava, Photon Nanostruct: Fundam Appl **7**, 170–175 (2009).
[185] O. Krasnykov, A. Karabchevsky, A. Shalabney, M. Auslender, and I. Abdulhalim, Opt. Commun. **284**, 1435–1438 (2011).
[186] S. A. Maier, Plasmonics: Fundamentals and Applications (Springer, New York, 2007).
[187] P. B. Catrysse, and S. Fan, J. Nanophotonics, **2**, 021790 (2008).
[188] H. Gai, J. Wang, and Q. Tian, J. Nanophotonics, **1**, 013555 (2007).
[189] N. A. Hatab, C.-H. Hsueh, A. L. Gaddis, S. T. Retterer, J.-H. Li, G. Eres, Z. Zhang, and G. Baohua, Nano. Lett. **10**, 4952–55 (2010).

[190] P.-Y. Chung, T.-H. Lin, G. Schultz, C. Batich, and P. Jiang, Appl. Phys. Lett. **96**, 261108 (2010).
[191] W. Kubo, and S. Fujikawa, Nano Lett. **11**, 8–15 (2011).
[192] I. Abdulhalim, J. Opt. A, Pure Appl. Opt. **11**, 015002 (2009).
[193] R. A. Depine, and M. L. Gigli, Opt. Lett. **20**, 2243–45 (1995).
[194] R. A. Depine, and M. L. Gigli, J. Opt. Soc. Am. A **14**, 510–519 (1997).
[195] J. A. Polo Jr., A. Lakhtakia, Opt. Commun. **281**, 5453–5457 (2008).
[196] J. A. Polo Jr., and A. Lakhtakia, J. Opt. Soc. Am. A **26**, 1696–1703 (2009).
[197] M. A. Motyka, and A. Lakhtakia, J. Nanophotonics **2**, 021910 (2008).
[198] M. A. Motyka, and A. Lakhtakia, J. Nanophotonics **3**, 033502 (2009).
[199] D. E. Gomez, K. C. Vernon, P. Mulvaney, and T. J. Davis, Nano Lett. **10**, 274–278 (2010).
[200] I. Abdulhalim, M. Auslender, and S. Hava, J. Nanophotonics **1**, 011680 (2007).
[201] I. Abdulhalim, Chin. Opt. Lett. **7**, 667–670 (2009).